Geodynamic models of plume-ridge interaction: Case studies of the Réunion, Iceland and Kerguelen mantle plumes

Kumulative Dissertation
zur Erlangung des akademischen Grades
"doctor rerum naturalium"
(Dr. rer. nat.)
in der Wissenschaftsdisziplin Geophysik

eingereicht an der
Mathematisch-Naturwissenschaftlichen Fakultät
der Universität Potsdam

von
Eva Bredow

Potsdam, den 22. November 2017

Erstbetreuer:	Prof. Dr. Michael Weber
Zweitbetreuer:	Dr. Bernhard Steinberger
Mentor:	Prof. Dr. Karin Sigloch
Gutachter:	Prof. Dr. Clinton Conrad Prof. Dr. Claire Currie

Published online at the
Institutional Repository of the University of Potsdam:
URN urn:nbn:de:kobv:517-opus4-411732
http://nbn-resolving.de/urn:nbn:de:kobv:517-opus4-411732

Abstract

According to the classical plume hypothesis, mantle plumes are localized upwellings of hot, buoyant material in the Earth's mantle. They have a typical mushroom shape, consisting of a large plume head, which is associated with the formation of voluminous flood basalts (a Large Igneous Province) and a narrow plume tail, which generates a linear, age-progressive chain of volcanic edifices (a hotspot track) as the tectonic plate migrates over the relatively stationary plume. Both plume heads and tails reshape large areas of the Earth's surface over many tens of millions of years.

However, not every plume has left an exemplary record that supports the classical hypothesis. The main objective of this thesis is therefore to study how specific hotspots have created the crustal thickness pattern attributed to their volcanic activities. Using regional geodynamic models, the main chapters of this thesis address the challenge of deciphering the three individual (and increasingly complex) Réunion, Iceland, and Kerguelen hotspot histories, especially focussing on the interactions between the respective plume and nearby spreading ridges.

For this purpose, the mantle convection code ASPECT is used to set up three-dimensional numerical models, which consider the specific local surroundings of each plume by prescribing time-dependent boundary conditions for temperature and mantle flow. Combining reconstructed plate boundaries and plate motions, large-scale global flow velocities and an inhomogeneous lithosphere thickness distribution together with a dehydration rheology represents a novel setup for regional convection models.

The model results show the crustal thickness pattern produced by the plume, which is compared to present-day topographic structures, crustal thickness estimates and age determinations of volcanic provinces associated with hotspot activity. Altogether, the model results agree well with surface observations. Moreover, the dynamic development of the plumes in the models provide explanations for the generation of smaller, yet characteristic volcanic features that were previously unexplained. Considering the present-day state of a model as a prediction for the current temperature distribution in the mantle, it cannot only be compared to observations on the surface, but also to structures in the Earth's interior as imaged by seismic tomography.

More precisely, in the case of the Réunion hotspot, the model demonstrates how the distinctive gap between the Maldives and Chagos is generated due to the combination of the ridge geometry and plume-ridge interaction. Further, the Rodrigues Ridge is formed as the surface expression of a long-distance sublithospheric flow channel between the upwelling plume and the closest ridge segment, confirming the long-standing hypothesis of Morgan (1978) for the first time in a dynamic context. The Réunion plume has been studied in connection with the seismological RHUM-RUM project, which has recently provided new seismic tomography images that yield an excellent match with the geodynamic model.

Regarding the Iceland plume, the numerical model shows how plume material may have accumulated in an east-west trending corridor of thin lithosphere across Greenland and resulted in simultaneous melt generation west and east of Greenland. This provides an explanation for the

extremely widespread volcanic material attributed to magma production of the Iceland hotspot and demonstrates that the model setup is also able to explain more complicated hotspot histories. The Iceland model results also agree well with newly derived seismic tomographic images.

The Kerguelen hotspot has an extremely complex history and previous studies concluded that the plume might be dismembered or influenced by solitary waves in its conduit to produce the reconstructed variable melt production rate. The geodynamic model, however, shows that a constant plume influx can result in a variable magma production rate if the plume interacts with nearby mid-ocean ridges. Moreover, the Ninetyeast Ridge in the model is created by on-ridge activities, while the Kerguelen plume was located beneath the Australian plate. This is also a contrast to earlier studies, which described the Ninetyeast Ridge as the result of the Indian plate passing over the plume. Furthermore, the Amsterdam-Saint Paul Plateau in the model is the result of plume material flowing from the upwelling toward the Southeast Indian Ridge, whereas previous geochemical studies attributed that volcanic province to a separate deep plume.

In summary, the three case studies presented in this thesis consistently highlight the importance of plume-ridge interaction in order to reconstruct the overall volcanic hotspot record as well as specific smaller features attributed to a certain hotspot. They also demonstrate that it is not necessary to attribute highly complicated properties to a specific plume in order to account for complex observations. Thus, this thesis contributes to the general understanding of plume dynamics and extends the very specific knowledge about the Réunion, Iceland, and Kerguelen mantle plumes.

Zusammenfassung

Nach der klassischen Plume-Hypothese sind Mantelplumes lokalisierte Aufströme aus heißem, aufsteigenden Material im Erdmantel und haben eine typische pilzförmige Struktur. Sie bestehen aus einem großen Plume-Kopf, der mit der Bildung von voluminösen Flutbasalten (einer Magmatischen Großprovinz) assoziiert wird und einem engen Plume-Schlauch, der eine lineare Kette von Vulkanen mit aufsteigendem Alter (einen Hotspot-Track) erzeugt, indem die tektonische Platte über den relativ stationären Plume wandert. Sowohl Plume-Köpfe als auch Plume-Schläuche formen große Gebiete der Erdoberfläche über viele zehn Millionen Jahre um.

Allerdings hat nicht jeder Plume mustergültige Spuren hinterlassen, die die klassische Hypothese unterstützen. Das Hauptziel dieser Arbeit ist daher zu untersuchen, wie ein spezifischer Hotspot den ihm zugeordneten Hotspot-Track erzeugt hat. Mit Hilfe regionaler geodynamischer Modelle stellen sich die Hauptkapitel dieser Arbeit der Herausforderung, die drei individuellen (und zunehmend komplexen) Geschichten des Réunion-, Island- und Kerguelen-Hotspots zu entschlüsseln, wobei insbesondere die Wechselwirkungen zwischen dem jeweiligen Plume und nahegelegenen Mittelozeanischen Rücken im Mittelpunkt stehen.

Zu diesem Zweck wird der Mantelkonvektions-Code ASPECT verwendet, um dreidimensionale numerische Modelle zu erstellen, die die spezielle lokale Umgebung jedes Plumes berücksichtigen, indem zeitabhängige Randbedingungen für Temperatur und Mantelströmung vorgeschrieben werden. Die Kombination von rekonstruierten Plattengrenzen und Plattenbewegungen, großräumigen globalen Strömungsgeschwindigkeiten und einer inhomogenen Lithosphärendickenverteilung zusammen mit einer Dehydrierungs-Rheologie stellt eine neue Konfiguration für regionale Konvektionsmodelle dar.

Die Modellergebnisse zeigen die vom Plume produzierte Verteilung von vulkanischem Material, die mit heutigen topographischen Strukturen, Schätzungen der Krustendicke und Altersbestimmungen vulkanischer Provinzen verglichen wird. Insgesamt stimmen die Modellergebnisse gut mit den Oberflächenbeobachtungen überein. Darüber hinaus liefert die dynamische Entwicklung der Plumes in den Modellen Erklärungen für die Erzeugung kleinerer, aber charakteristischer vulkanischer Strukturen, deren Herkunft bisher unerklärt war. Betrachtet man den heutigen Zustand eines Modells als Vorhersage für die aktuelle Temperaturverteilung im Mantel, kann man ihn nicht nur mit Beobachtungen an der Oberfläche vergleichen, sondern auch mit Strukturen im Erdinneren, wie sie durch seismische Tomographie abgebildet werden.

Genauer gesagt zeigt das Modell im Falle des Réunion-Hotspots, wie die charakteristische Lücke zwischen den Malediven und Chagos aufgrund der Kombination der Geometrie des Mittelozeanischen Rückens und der Interaktion zwischen Plume und Rücken erzeugt wird. Des Weiteren wird der Rodrigues-Rücken als Oberflächenerscheinung eines sublithosphärischen Strömungskanals zwischen dem aufsteigenden Plume und dem nächstgelegenen Segment des Mittelozeanischen Rückens gebildet, was die langjährige Hypothese von Morgan (1978) zum ersten Mal in einem dynamischen Kontext bestätigt. Der Réunion-Plume wurde im Rahmen des seismologischen RHUM-RUM-Projektes untersucht, das kürzlich neue seismische Tomographiebilder

ergeben hat, die eine exzellente Übereinstimmung mit dem geodynamischen Modell aufweisen.

Was den Island-Plume betrifft, so zeigt das numerische Modell, wie sich Plume-Material in einem von Ost nach West verlaufenden Korridor dünner Lithosphäre in Grönland angesammelt haben könnte und zu einer gleichzeitigen Schmelzerzeugung westlich und östlich von Grönland geführt hat. Dies erklärt das extrem weit verbreitete vulkanische Material, das der Magmaproduktion des Island-Hotspots zugeschrieben wird, und demonstriert, dass der Modell-Aufbau auch kompliziertere Hotspot-Geschichten erklären kann. Die Ergebnisse des Island-Modells stimmen ebenfalls gut mit neu erzeugten seismischen Tomographiebildern überein.

Der Kerguelen-Hotspot hat eine äußerst komplexe Geschichte und frühere Studien kamen zu dem Schluss, dass der Plume eine zerrissene Struktur oder durch einzelne Wellen im Schlauch beeinflusst sein könnte, um die rekonstruierte variable Schmelzproduktionsrate zu erzeugen. Das geodynamische Modell zeigt jedoch, dass ein konstanter Plume-Einstrom zu einer variablen Magmaproduktionsrate führen kann, wenn der Plume mit nahegelegenen mittelozeanischen Rücken interagiert. Darüber hinaus wird der Neunzig-Grad-Ost-Rücken im Modell am Mittelozeanischen Rücken erschaffen, während der Kerguelen-Plume unter der australischen Platte lag. Dies steht auch im Gegensatz zu früheren Studien, die den Neunzig-Grad-Ost-Rücken als Ergebnis der über den Plume wandernden indischen Platte beschrieben haben. Darüber hinaus ist das Amsterdam-Saint Paul-Plateau im Modell das Ergebnis von Plume-Material, das von der Aufstiegsregion in Richtung des Südostindischen Rückens fließt, wohingegen frühere geochemische Studien diese vulkanische Provinz einem separaten tiefen Plume zugeschrieben haben.

Zusammenfassend verdeutlichen die drei in dieser Arbeit präsentierten Fallstudien die Bedeutung der Interaktion zwischen Plume und Mittelozeanischen Rücken für die Rekonstruktion der Verteilung des gesamten vom Hotspot erzeugten vulkanischen Materials sowie von spezifischen kleineren Strukturen, die einem bestimmten Hotspot zugeordnet sind. Es wird auch gezeigt, dass es nicht notwendig ist, einem bestimmten Plume hochkomplizierte Eigenschaften zuzuschreiben, um komplexe Beobachtungen zu erklären. Somit trägt diese Arbeit zum allgemeinen Verständnis der Dynamik von Plumes bei und erweitert das sehr spezifische Wissen über die Réunion-, Island-, und Kerguelen-Mantelplumes.

Contents

1 Introduction

1.1 Hotspots and Mantle Plumes

Hotspots are localized surface regions where long-term volcanic activities take place without the involvement of any plate tectonic processes (e.g. Schubert et al., 2001). Thus being independent of the location, they occur in the interior of tectonic plates as well as at plate boundaries, where they are recognizable by intense volcanism and unusually thick crust. Hawaii, located in the interior of the Pacific plate, is the prototype example of an intraplate hotspot, whereas Iceland is well-known for being situated directly on a mid-ocean ridge. Due to the rather vague definition, the number of hotspots varies in different studies, but is mostly estimated between 40 and 50 (Sleep, 1990; Courtillot et al., 2003; King and Adam, 2014). The hotspot catalogue of Steinberger (2000), for example, is derived from global mantle flow models and lists 44 hotspots possibly fed by mantle plumes. Figure 1.1 shows their global distribution and points out the three hotspots of major interest for this thesis: Réunion on the African plate, Iceland on the Mid-Atlantic Ridge between the North American and Eurasian plates and Kerguelen on the Antarctic plate.

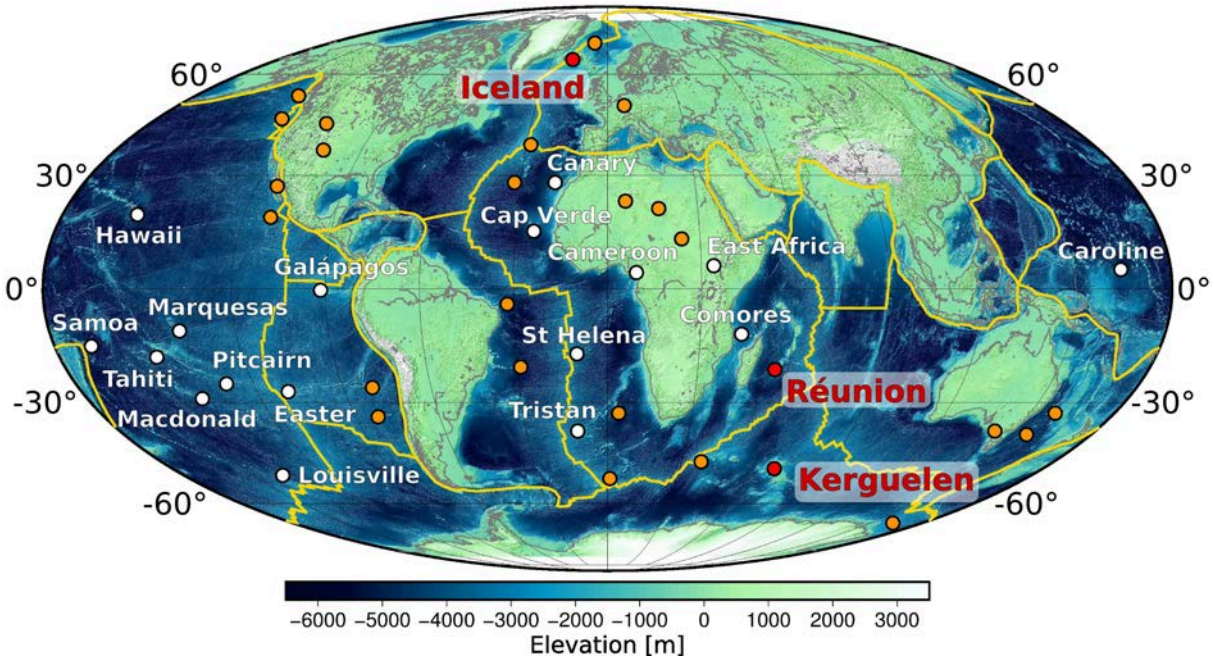

Figure 1.1: Global distribution of the 44 hotspots from Steinberger (2000) (orange, white and red circles), the 20 hotspots under which the whole-mantle seismic imaging study of French and Romanowicz (2015) detected primary and clearly resolved plumes (white and red circles) and the 3 hotspots of main importance for this thesis (red circles) shown on a topographic map (Smith and Sandwell, 1997); yellow lines indicate plate boundaries.

Historically, it was the Hawaii hotspot that inspired Wilson (1963) to suggest that heat sources in the mantle might remain stationary underneath the moving lithospheric plates. This concept elegantly explained the origin of the distinctly age-progressive and linear Hawaiian island chain

and initiated the development of the classical plume hypothesis. Later, Morgan (1971, 1972) refined this hypothesis by proposing that convection plumes originate from the lowermost mantle and ascend buoyantly to the base of the lithosphere, where they spread radially from the plume centre. Subsequently, pressure-release melting triggers magmatic activity at the surface and creates a hotspot.

To date, these central elements of Morgan's hypothesis are widely accepted and more recent definitions still specify mantle plumes as localized upwellings of hot, buoyant material in the Earth's mantle that most likely originate from the core-mantle boundary (CMB) at approximately 2900 km depth (e.g. Schubert et al., 2001).

Thermal plumes (as well as subduction zones) are basic features in a convecting system and they originate naturally from instabilities at hot thermal boundary layers such as the CMB. Historically, the physics of thermal convection and plume initiation in particular has been investigated in laboratory experiments (Whitehead and Luther, 1975; Griffiths and Campbell, 1990) as well as in numerical models (Farnetani and Richards, 1995; van Keken, 1997).

Regarding the geometry of thermal plumes, all studies concluded that starting plumes consist of a large diapir, or plume head, followed by a thin conduit, or plume tail, that maintains the connection with the source region and continues to transport material upward. The plume structure is therefore often described as a mushroom shape (Kellogg and King, 1997), as shown in Figure 1.2. Both plume heads and tails cause large-scale effects on the Earth's surface, but in different, characteristic ways.

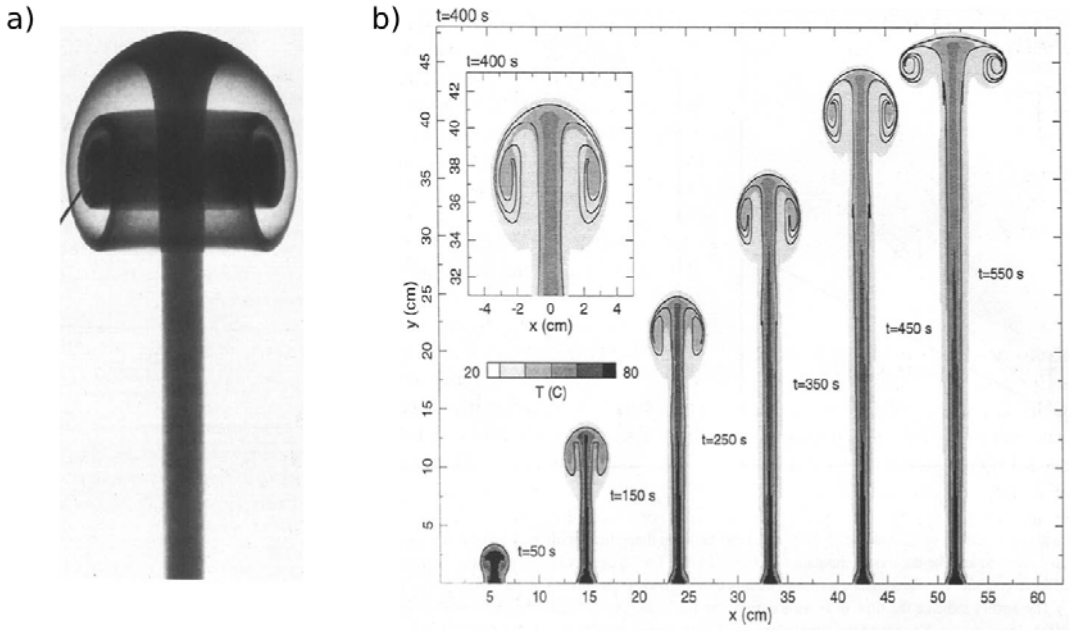

Figure 1.2: Mushroom shaped geometry of starting thermal plumes from (a) laboratory experiments of Griffiths and Campbell (1990) and (b) numerical models with laboratory scaling of van Keken (1997).

The arrival of a plume head at the base of the lithosphere is associated with the onset of massive flood basalt eruptions (Richards et al., 1989). During the relatively short time of a

few million years, gigantic volumes of basaltic material are produced and create a Large Igneous Province (LIP), which can occur either as a continental flood basalt province such as the Deccan Traps in India, or as an oceanic plateau, such as the Kerguelen Plateau in the southern Indian Ocean. More specifically, Bryan and Ernst (2008) defined LIPs as "magmatic provinces with areal extents $> 0.1 \times 10^6\,\mathrm{km}^2$, igneous volumes $> 0.1 \times 10^6\,\mathrm{km}^3$ and maximum lifespans of $\sim$50 Myr that have intraplate tectonic settings or geochemical affinities, and are characterised by igneous pulse(s) of short duration ($\sim$1 – 5 Myr), during which a large proportion ($> 75\%$) of the total igneous volume has been emplaced."

The generation of many LIPs coincided in time with major mass extinction events, for example the largest continental LIP, the Siberian Traps, was generated at the time of the largest known mass extinction event at the Permo/Triassic boundary (Sobolev et al., 2011), whereas the creation of the Deccan Traps in India is associated with the mass extinction at the Cretacious/Tertiary boundary, with an extinction rate of almost 40% and well-known for the extinction of the dinosaurs (Courtillot and Renne, 2003).

Figure 1.3 visualizes the dimensions and the number of the areas that have been affected by plume head related volcanism in the past 500 million years.

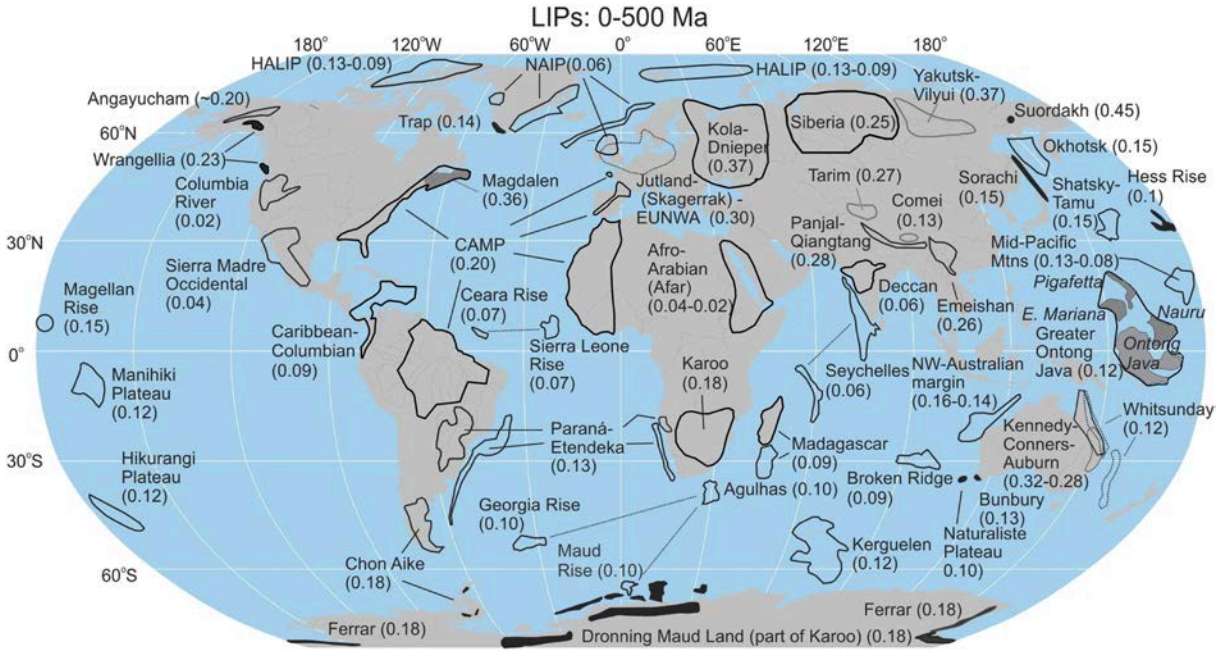

Figure 1.3: Global distribution of LIPs and associated magmatic fragments (including selected silicic LIPs) created during the last 500 Ma, with ages given in Ga. From Ernst and Youbi (2017).

Many LIPs mark the temporal and spatial onset of hotspot tracks – age-progressive chains of volcanic islands and seamounts, oriented parallel to the motions of the tectonic plates, and regarded as the surface expression of plume tails (Richards et al., 1989). Hotspot tracks are created over much longer periods of time than LIPs, suggesting that the plume tail remains constantly active over many tens of million years, but the magma production rate is much lower than during the flood basalt generation. The most prominent example of a hotspot track is the

Hawaiian-Emperor seamount chain. The younger end of the hotspot track marks the current hotspot position, often the location of an active volcano, such as Hawaii Island.

Figure 1.4 shows the dimensions of all the volcanic provinces that Coffin et al. (2006) have associated with hotspot volcanism: flood basalts are marked in red and their corresponding hotspot tracks are marked in blue. It should however be noted that different studies disagree about which magmatic provinces, in particular the smaller fragments, are considered to be part of a LIP or hotspot track, such that comparable figures (as the extents of the LIPs in Figure 1.3) may look different.

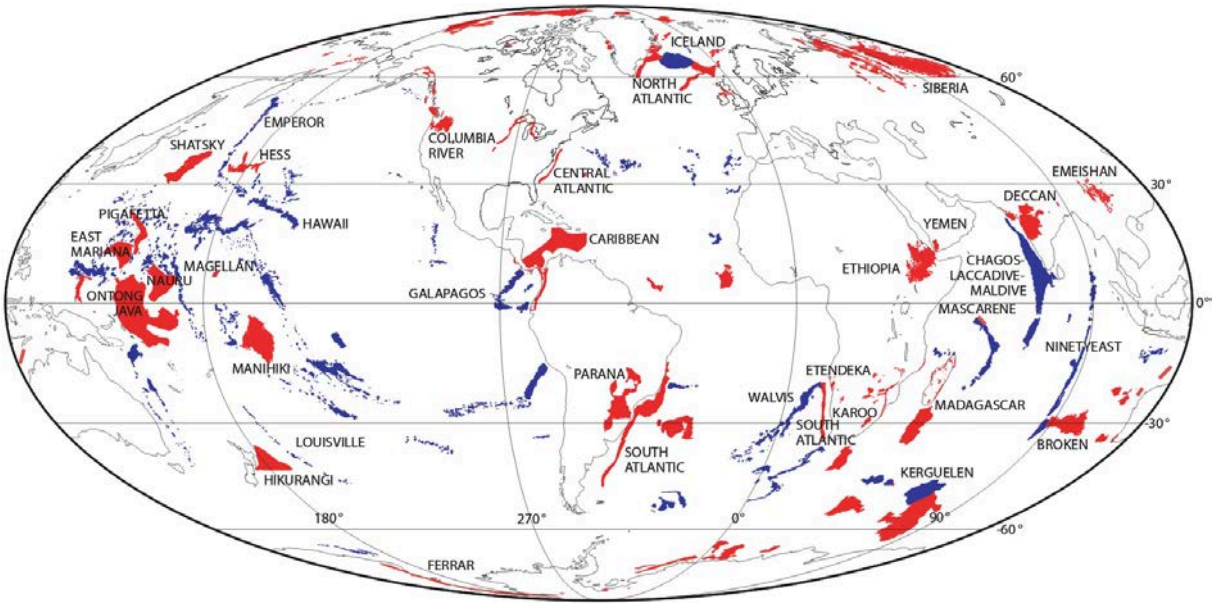

Figure 1.4: Global distribution and areal extents of the LIPs (red areas) and their corresponding hotspot tracks (blue areas), showing that plume heads and tails have created numerous, large-scale and very complex patterns of volcanic material on the Earth's surface. From Coffin et al. (2006).

Figure 1.4 illustrates that some hotspots have experienced an exemplary history, supporting the classical plume hypothesis. The Réunion hotspot, for example, is associated with the Deccan Traps in India, a large-scale continental LIP and the hotspot track can be followed almost linearly (except for the split of the track due to seafloor-spreading; see section 1.2) toward Réunion Island and its active volcano, the Piton de la Fournaise.

Other hotspots, however, have produced more complicated structures. For example, there is no LIP corresponding to the Hawaii hotspot – it has potentially been subducted; the Canary Islands have been volcanically active for approximately 65 Ma – but no apparent hotspot track or LIP; and the North Atlantic Igneous Province, associated with the Iceland hotspot, is widely (and not at all linearly) distributed between West Greenland, the North Atlantic, and even as far as Scotland and Ireland (for an overview of hotspots and their present or absent characteristics indicating a deep origin, see Courtillot et al., 2003).

In order to decipher these complex histories of individual hotspots and their impacts on the Earth's surface – as done in this thesis – the regional context of each plume has to be considered.

1.2 Plume-Ridge Interaction

Given the longevity and relatively fixed positions of plume tails and hotspots, many of them are eventually approached and even overridden by mid-ocean ridges. The fact that the hotspot activity remains intact and the hotspot track production continues on the opposite side of the ridge indicates a deep origin of the plume source underneath (Schubert et al., 2001).

Seafloor-spreading along the ridge after it has migrated over the plume results in a discontinuous hotspot track. For example, seafloor-spreading at the Central Indian Ridge after its passage over the Réunion hotspot has led to a disconnected hotspot track in the Indian Ocean (McKenzie and Sclater, 1971).

Both hotspots and mid-ocean ridges are major sites of mantle upwelling, partial melting, magma production and finally crust generation, and thus shape large areas of the Earth's surface. If they are located close enough, plumes and ridges dynamically interact with each other on large scales, such that plume-induced chemical anomalies (the geochemical signature of ocean island basalts (OIBs) distinctly differs from that of mid-ocean ridge basalts (MORBs)) and physical anomalies (regional topographic highs and unusually thick crust) can currently be observed along 15 – 20 % of the entire global mid-ocean ridge system (Ito et al., 2003).

Over the past 30 years, numerous studies have used (combinations of) geochemical observations, geophysical methods, geodynamic laboratory experiments and numerical models to extend the understanding of plume-ridge interaction (e.g. Schilling et al., 1985; Schilling, 1991; Ribe and Christensen, 1994; Ito and Lin, 1995; Ribe et al., 1995; Ito et al., 1996; Ribe, 1996; Ito et al., 1997; Albers and Christensen, 2001; Georgen et al., 2001; Mittelstaedt and Ito, 2005; Georgen, 2011; Mittelstaedt et al., 2011; Howell et al., 2014; Dordevic and Georgen, 2016; Mittal and Richards, 2017). They all followed the basic hypothesis that plumes arriving at the base of the lithosphere spread compositionally distinct material toward and along mid-ocean ridges in their vicinity (see Figure 1.5). For an extensive review of previous results, see Ito et al. (2003).

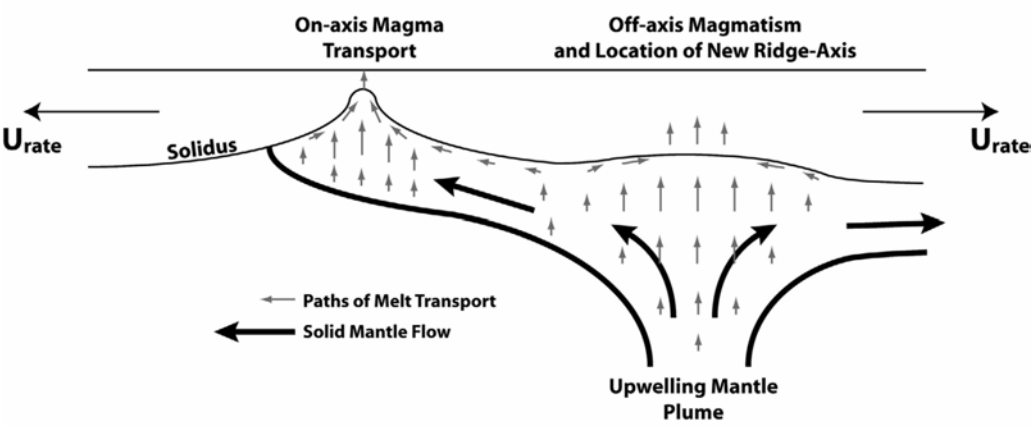

Figure 1.5: Conceptual model of a near-ridge mantle plume where melt flows along the base of the lithosphere toward the ridge axis, where it causes on-ridge volcanism. Magma passing through fractures in the lithosphere above the upwelling plume thins and weakens the plate and leads to off-ridge volcanism, which can even result in a ridge jump. From Mittelstaedt et al. (2011).

Important factors controlling this interaction are the excess temperature, buoyancy flux and viscosity of the plume, the spreading rate of the plates at the ridge axis, lithospheric thickness variations, the shear force of the plates and the relative motion between the ridge and the plume (Ito et al., 2003; Ribe et al., 2007). Furthermore, an approaching ridge needs to be relatively close to the plume before an interaction takes place, whereas a ridge retreating from a plume is fed by plume material over greater distances – the ridge seems to "capture" the plume.

Concerning the amount of generated melt, Ito et al. (1999) described that the extraction of water at the onset of partial melting, i.e. dehydration of the mantle, causes an abrupt increase in viscosity and thus reduces the melt production significantly. Crustal thickness estimates considering this effect yield values comparable to those observed at mid-ocean ridges – which implies that considering a dehydration rheology most likely improves models of plume-ridge interaction, for which melting plays an important role.

Regarding the flow of plume material toward a ridge, Sleep (1997) reported that the relief on the base of the lithosphere may act as an upside-down drainage pattern. Since the lithosphere cools and thickens as a function of age with increasing distance from a spreading ridge, the buoyant plume material can flow mainly upward toward the ridge axis. It should be noted that the lithosphere thickness is an important factor controlling the amount of decompressional melting at both on-ridge and off-ridge hotspots, which makes the lithosphere thickness distribution another important parameter in models of plume-ridge interaction.

Also notable is the study of Morgan (1978), which proposed that plume material potentially flows in a sublithospheric channel toward the closest mid-ocean ridge segment. This long-distance flow might progressively carve a thermal channel into the lithosphere and could thus be an explanation for the narrow crustal lineaments that seem to link hotspots and ridges regardless of the directions of the plate motions. Examples are the Wolf-Darwin lineament close to Galápagos and the Rodrigues Ridge close to La Réunion.

For on-ridge hotspots, hot plume material, which can be recognized by its distinct geochemical signature, is expected to flow laterally along the ridge axis as for example evidenced by the V-shaped ridges on both sides of the Reykjanes Ridge close to Iceland (Albers and Christensen, 2001; Ito et al., 2003).

Plume-ridge interaction is even considered to be able to cause jumps of mid-ocean ridge segments toward nearby hotspots (Mittelstaedt et al., 2011, see Figure 1.5), thus altering the global configuration of tectonic plate boundaries.

In summary, the effects of plume-ridge interaction are expected to play a major role in the development in many hotspot tracks and hence require special attention in numerical simulations of mantle plumes.

1.3 Seismological Images of Mantle Plumes

Since deep mantle plumes cannot be directly observed and studied, their physical properties and origin have been vigorously debated by geoscientists over the last decades and their existence has even been entirely questioned (e.g. Anderson and Natland, 2005; Foulger, 2011).

The most promising – although indirect – technique to confirm the existence of deeply rooted plumes in the mantle is seismic tomography, which uses the low seismic velocity anomaly associated with the hot, upwelling material to image plume structures in the mantle. In contrast to geodynamic models or laboratory experiments, seismic tomography captures only the present-day state of the mantle. Difficulties arise however from the limited ray coverage around the often remotely located oceanic hotspot islands and a drastically decreasing resolution at greater depths (e.g. Nolet et al., 2007; Zhao, 2007). Moreover, the relatively narrow plume tail conduits may be entirely hidden due to the destructive interference of diffracted and direct waves – an effect known as wavefront healing (Nolet and Dahlen, 2000; Hung et al., 2001; Hwang et al., 2011).

The first reasonable evidence of deep plumes from seismic tomography was not provided until the studies of Montelli et al. (2004), Zhao (2004), Montelli et al. (2006), and Suetsugu et al. (2009) – more than 30 years after Morgan's original hypothesis. More recently, the study of French and Romanowicz (2015), based on a whole-mantle seismic imaging technique, achieved results with a highly improved resolution. Figure 1.6 shows the 20 plumes listed as primary plumes (such as Hawaii and Iceland) and clearly resolved plumes (such as Réunion and Kerguelen) with vertically continuous conduits in the depths between 1000 – 2800 km.

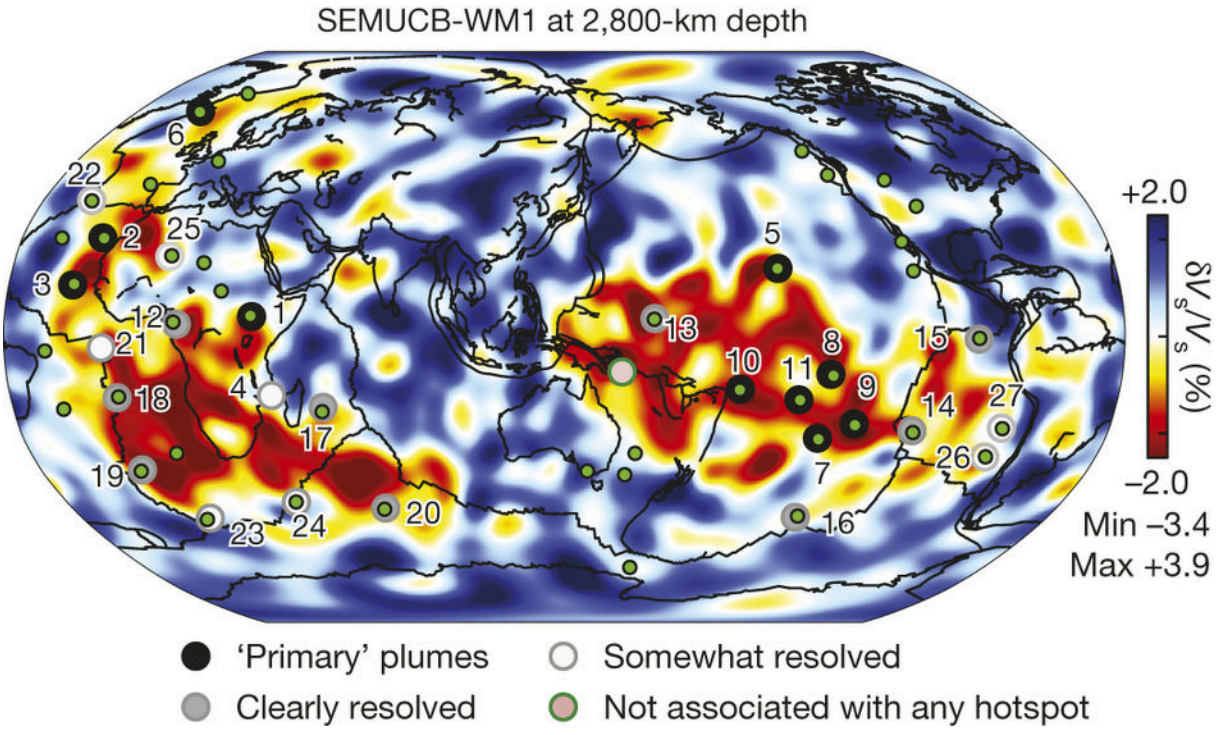

Figure 1.6: Global distribution of plumes with vertically continuous conduits in the lower mantle from the seismic tomography study of French and Romanowicz (2015). 6 – Iceland, 17 – Réunion, 20 – Kerguelen.

The colors in Figure 1.6 correspond to the S-wave velocity variations at 2800 km depth relative to global average velocities at that depth. The two large clusters of red colored areas show the African and Pacific Large Low Shear Velocity Provinces (LLSVPs) at the base of the mantle

(Garnero et al., 2007). The LLSVPs are thought to represent almost antipodal, large-scale, long-lived piles of chemically distinct and denser material in the lowermost mantle (e.g. Mulyukova et al., 2015), which are expected to have strong impacts on the large-scale flow in the deep mantle (Dziewonski et al., 2010).

Moreover, Figure 1.6 illustrates that deep plumes are not randomly distributed. Instead, they seem to rise from the margins of the two LLSVPs, which are considered to be Plume Generation Zones (PGZs), since they do not only correspond to the present-day locations of the plumes with potentially deep origins, but also to the reconstructed eruption sites of the LIPs (Torsvik et al., 2006; Burke et al., 2008).

For the context of his thesis, it should be noted that the Réunion, Iceland, and Kerguelen plumes are thought to originate from the deep mantle and, more specifically, from the margins of the African LLSVP.

1.4 Geodynamic Models of Mantle Plumes

Numerical models are an important tool to study features in the Earth's deep interior that are inaccessible to direct observations such as mantle plumes. In contrast to seismic tomography, they do not only provide insights into the current state, but also into the temporal development of plumes. Compared to laboratory experiments, they are able to consider much more complicated scenarios, such as a nonlinear mantle rheology with a strong temperature and stress dependence (for an extensive review, see e.g. Ribe et al., 2007).

However, the available computing power and time – even though constantly increasing – limits the complexity as well as the resolution of numerical models. Therefore, models are not designed to incorporate all the physical properties constrained by previous studies, but instead, they are set up individually with specific purposes and make use of appropriate simplifications. This also makes it easier to investigate how specific input parameters influence the model evolution.

Models are well suited to include data obtained from other geoscientific disciplines. For example, the excess temperature of a plume, derived from the heat flux at a hotspot by geochemical methods (e.g. Schilling, 1991; Putirka, 2008) is a valuable input parameter for a plume model. The model results can then be used to constrain further plume parameters, such as the buoyancy flux, or to compare how well the model fits observations of processes in the Earth's mantle or features at the surface, such as hotspot swells (regional topographic highs at active hotspot sites).

After many general models of plumes (with different rheologies) interacting with the lithosphere, moving plates, mid-ocean ridges or triple junctions, etc., (summarizing all studies and their results is outside the scope of this introduction), there have also been models that resemble a certain hotspot regarding the geometry of nearby ridges or plume parameters derived from geochemical studies. For example, the plumes underneath Iceland (Ito et al., 1996, 1999; Howell et al., 2014; Ito et al., 2015; Koptev et al., 2017), Hawaii (Ballmer et al., 2013) and Galápagos (Ito et al., 1997; Mittal and Richards, 2017) have been modeled in previous studies.

However, all these previous models have considered the respective plume as an isolated feature in the mantle, neglecting the influence of the large-scale global mantle flow, which is likely able to deflect structures in the mantle. The first regional model taking into account the global flow field surrounding a plume was presented by Gassmöller et al. (2016), which reconstructed the geodynamic history of the Tristan plume in the South Atlantic (also counted as a clearly resolved plume by French and Romanowicz (2015) – number 19 in Figure 1.6 and rising from the margin of the African LLSVP). The model setup and velocity boundary conditions from Gassmöller et al. (2016) – more precisely, R. Gassmöller, J. Dannberg, E. Bredow, B. Steinberger and T. H. Torsvik (2016) – are shown in Figure 1.7. For the geodynamic models described in this thesis, this preceding setup has been extended as necessary in order to focus on the three (increasingly complex) individual histories of the Réunion, Iceland, and Kerguelen mantle plumes and, in particular, on their interaction with nearby spreading ridges.

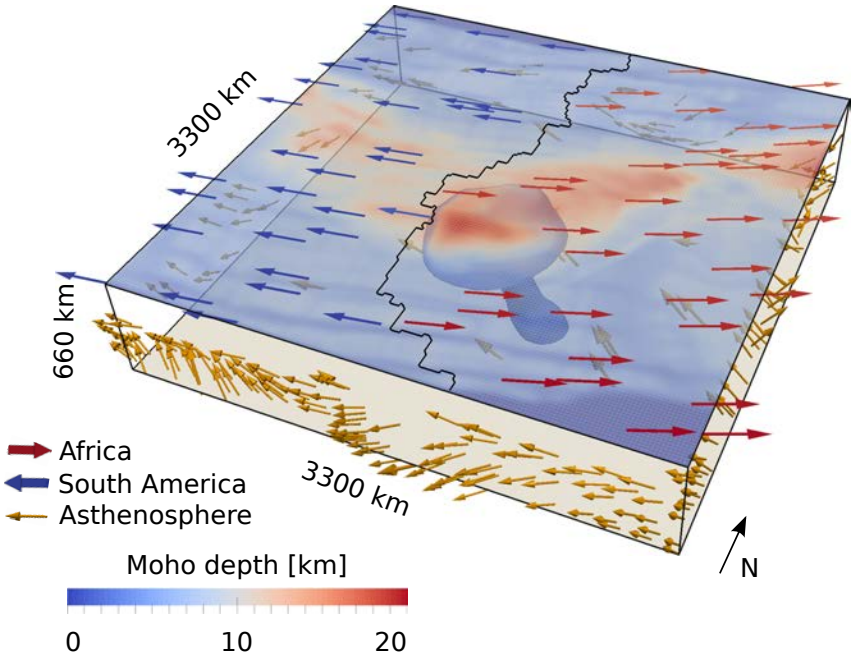

Figure 1.7: Model setup of the Tristan plume model from Gassmöller et al. (2016), which prescribes global flow velocities at the side boundaries and the bottom of the model domain (yellow arrows).

1.5 Aims of this Thesis

The overall objective of this thesis is to test how well a regional geodynamic model with a plume can predict a specific LIP and hotspot track – regarding the timing of the melt generation, the distribution of volcanic material (including small-scale features) and the produced crustal thickness. The model result – a map showing the crustal thickness contribution of the plume – can be compared to age dates of the volcanic provinces associated with hotspot activities, present-day topographic structures and crustal thickness estimates derived from seismic studies. A reasonable match between the model predictions and surface observations provides evidence

that the reconstructed plate boundaries, plate motions, global flow velocities and lithosphere thickness distributions used as time-dependent input parameters in the model are most likely reliable. Consequently, the present-day state of the model can be regarded as a true "prediction" for the current thermal state of the upper mantle that can be compared to seismic tomography images and thus to observations of structures in the mantle, not only on the surface.

Moreover, as already mentioned in section 1.1, not every hotspot has left an exemplary record of a LIP and a linear hotspot track leading to an active volcano, which means that the classical plume hypothesis alone cannot entirely explain each system, especially smaller, yet characteristic features. Previous studies have attributed highly complicated properties to specific plumes to account for complex observations. For example, solitary waves in the plume conduit are expected to generate pulses of volcanic activities, or plumes are considered to be unusually hot or buoyant, or multiple plumes relatively close to each other are considered to be responsible for widely distributed and numerous volcanic provinces, etc. The regional models in this thesis can therefore provide a geodynamic context for the creation of complicated structures and be used to constrain the properties of each individual plume.

1.6 Overview of the Manuscripts and Author Contributions

The main chapters of this thesis consist of three manuscripts that have been submitted to peer-reviewed scientific journals. At the time of writing, Manuscript 1 has been published, whereas Manuscripts 2 and 3 are still being reviewed.

The three manuscripts all study plume-ridge interaction on regional scales and investigate the dynamic histories of the Réunion, Iceland, and Kerguelen mantle plumes using the same model setup, but addressing different open questions in regard to each respective hotspot history.

1. Manuscript: How plume-ridge interaction shapes the crustal thickness pattern of the Réunion hotspot track

The first manuscript comprises the case study of the Réunion mantle plume and its interaction with the Central Indian Ridge over time. It mainly addresses the question of whether a numerical model with a plume can account for the present-day thickness and distribution of crust in the Indian Ocean and focusses particularly on the development of two small-scale features: the gap in the hotspot track between the Maldives and the Chagos Bank and the crustal lineament forming the Rodrigues Ridge.

This study includes a very detailed description of the regional model setup as well as an extensive parameter study.

This work was carried out as part of the French-German RHUM-RUM project (Réunion Hotspot and Upper Mantle - Réunions Unterer Mantel; more information can be found at http://www.rhum-rum.net/).

Authors: Eva Bredow, Bernhard Steinberger, Rene Gassmöller and Juliane Dannberg

Contributions: All authors jointly developed the structure and objectives of this study, designed the models and analysed the results. R.G., J.D. and E.B. implemented additional features in ASPECT that were required to use the lithosphere thickness reconstructions as initial and boundary conditions as well as the dehydration rheology, depletion buoyancy and changes in the rheology. B.S. provided the plate reconstructions, lithosphere thickness models and global flow models used as initial and boundary conditions in ASPECT. E.B. set up and performed the computations and designed the parameter study, created the figures and wrote the main part of the paper, with help from all other authors.

2. Manuscript: Widespread Cenozoic volcanism in the North Atlantic-Greenland region explained by the Iceland plume

The second manuscript comprises the case study of the Iceland mantle plume. It focusses on the extremely widespread volcanic material attributed to activities of the Iceland mantle plume during the past ≈62 Ma. The model results agree with highly resolved tomographic images that show an east-west corridor of thin lithosphere across Greenland and demonstrate how plume material may have accumulated in this channel and led to simultaneous melt generation west and east of Greenland, explaining the widespread volcanic material observed today, not resembling a typical hotspot track at all.

Authors: Bernhard Steinberger, Eva Bredow, Sergei Lebedev, Andrew Schaeffer and Trond H. Torsvik

Contributions: S.L. and B.S. conceived the paper. B.S. wrote the paper, with help from all other authors. E.B. set up and performed the computations with ASPECT and created the figure showing the numerical model. B.S. and E.B. analysed and interpreted the modeling results. A.S. and S.L. provided tomography and lithosphere thickness models. T.H.T. provided plate reconstructions and data on the distribution of volcanics. All authors jointly contributed to discussions.

3. Manuscript: Variable melt production rate of the Kerguelen hotspot due to long-term plume-ridge interaction

The third manuscript comprises the case study of the Kerguelen mantle plume and its uncommon and long-term magmatic history and especially considers its interaction with nearby spreading ridges. Our model demonstrates that a single and not unusually hot or buoyant plume can result in a variable melt production rate as implied by previous studies and explain further unusual characteristics attributed to the Kerguelen hotspot. The results indicate that the Ninetyeast Ridge was created by volcanism along the ridge axis between the Indian and Australian plate

and that the Amsterdam-Saint Paul Plateau might be generated by plume material flowing toward the closest segment of the Southeast Indian Ridge.

Authors: Eva Bredow and Bernhard Steinberger

Contributions: Both authors developed the objectives of this study. B.S. provided the plate reconstructions, lithosphere thickness models and global flow models used as initial and boundary conditions in the models. E.B. set up and performed the computations, analysed and interpreted the modeling results, created the figures and wrote the paper, supported by B.S.

References

Albers, M. and U. R. Christensen (2001), Channeling of plume flow beneath mid-ocean ridges, *Earth Planet. Sci. Lett.*, 187(1), 207 –220, doi: 10.1016/S0012-821X(01)00276-X.

Anderson, D. L. and J. H. Natland (2005), A brief history of the plume hypothesis and its competitors: concept and controversy, *Geological Society of America Special Papers*, 388, 119–145, doi: 10.1130/0-8137-2388-4.119.

Ballmer, M. D., G. Ito, C. J. Wolfe, and S. C. Solomon (2013), Double layering of a thermochemical plume in the upper mantle beneath Hawaii, *Earth Planet. Sci. Lett.*, 376, 155 –164, doi: 10.1016/j.epsl.2013.06.022.

Bryan, S. E. and R. E. Ernst (2008), Revised definition of Large Igneous Provinces (LIPs), *Earth-Science Reviews*, 86(1), 175–202, doi: 10.1016/j.earscirev.2007.08.008.

Burke, K., B. Steinberger, T. H. Torsvik, and M. A. Smethurst (2008), Plume Generation Zones at the margins of Large Low Shear Velocity Provinces on the core-mantle boundary, *Earth Planet. Sci. Lett.*, 265(1-2), 49–60, doi: 10.1016/j.epsl.2007.09.042.

Coffin, M. F., R. A. Duncan, O. Eldholm, J. G. Fitton, F. A. Frey, H. C. Larsen, J. J. Mahoney, A. D. Saunder, R. Schlich, and P. J. Wallace (2006), Large Igneous Provinces and Scientific Ocean Drilling: Status Quo and A Look Ahead, *Oceanography*, 19(4), 150–160, doi: 10.5670/oceanog.2006.13.

Courtillot, V. E. and P. R. Renne (2003), On the ages of flood basalt events, *C. R. Geosci.*, 335(1), 113–140, doi: 10.1016/S1631-0713(03)00006-3.

Courtillot, V., A. Davaille, J. Besse, and J. Stock (2003), Three distinct types of hotspots in the Earth's mantle, *Earth Planet. Sci. Lett.*, 205(3-4), 295–308, doi: 10.1016/S0012-821X(02)01048-8.

Dordevic, M. and J. Georgen (2016), Dynamics of plume–triple junction interaction: Results from a series of three-dimensional numerical models and implications for the formation of oceanic plateaus, *J. Geophys. Res.*, 121(3), 1316–1342, doi: 10.1002/2014JB011869.

Dziewonski, A. M., V. Lekic, and B. A. Romanowicz (2010), Mantle Anchor Structure: An argument for bottom up tectonics, *Earth Planet. Sci. Lett.*, 299(1), 69 –79, doi: 10.1016/j.epsl.2010.08.013.

Ernst, R. E. and N. Youbi (2017), How Large Igneous Provinces affect global climate, sometimes cause mass extinctions, and represent natural markers in the geological record, *Palaeogeography, Palaeoclimatology, Palaeoecology*, 478, 30 –52, doi: 10.1016/j.palaeo.2017.03.014.

Farnetani, D. G. and M. A. Richards (1995), Thermal entrainment and melting in mantle plumes, *Earth Planet. Sci. Lett.*, 136(3), 251 –267, doi: 10.1016/0012-821X(95)00158-9.

Foulger, G. R. (2011), *Plates vs plumes: a geological controversy*. John Wiley & Sons.

French, S. W. and B. Romanowicz (2015), Broad plumes rooted at the base of the Earth's mantle beneath major hotspots, *Nature*, 525, 95–99, doi: 10.1038/nature14876.

Garnero, E. J., T. Lay, and A. McNamara (2007), Implications of lower-mantle structural heterogeneity for the existence and nature of whole-mantle plumes, *Spec. Pap. Geol. Soc. Am.*, 430, 79–101, doi: 10.1130/2007.2430(05).

Gassmöller, R., J. Dannberg, E. Bredow, B. Steinberger, and T. H. Torsvik (2016), Major influence of plume-ridge interaction, lithosphere thickness variations, and global mantle flow on hotspot volcanism – The example of Tristan, *Geochem. Geophys. Geosyst.*, 17, 1454–1479, doi: 10.1002/2015GC006177.

Georgen, J. E. (2011), Lithospheric control on the spatial pattern of Azores hotspot seafloor anomalies: Constraints from a model of plume-triple junction interaction, *Geophys. Res. Lett.*, 38(19). L19305, doi: 10.1029/2011GL048742.

Georgen, J. E., J. Lin, and H. J. B. Dick (2001), Evidence from gravity anomalies for interactions of the Marion and Bouvet hotspots with the Southwest Indian Ridge: effects of transform offsets, *Earth Planet. Sci. Lett.*, 187(3), 283–300, doi: 10.1016/S0012-821X(01)00293-X.

Griffiths, R. W. and I. H. Campbell (1990), Stirring and structure in mantle starting plumes, *Earth Planet. Sci. Lett.*, 99(1), 66 –78, doi: 10.1016/0012-821X(90)90071-5.

Howell, S. M., G. Ito, A. J. Breivik, A. Rai, R. Mjelde, B. Hanan, K. Sayit, and P. Vogt (2014), The origin of the asymmetry in the Iceland hotspot along the Mid-Atlantic Ridge from continental breakup to present-day, *Earth Planet. Sci. Lett.*, 392, 143–153, doi: 10.1016/j.epsl.2014.02.020.

Hung, S.-H., F. A. Dahlen, and G. Nolet (2001), Wavefront healing: a banana–doughnut perspective, *Geophys. J. Int.*, 146(2), 289–312, doi: 10.1046/j.1365-246x.2001.01466.x.

Hwang, Y. K., J. Ritsema, P. E. van Keken, S. Goes, and E. Styles (2011), Wavefront healing renders deep plumes seismically invisible, *Geophys. J. Int.*, 187(1), 273–277, doi: 10.1111/j.1365-246X.2011.05173.x.

Ito, G., J. Lin, and D. Graham (2003), Observational and theoretical studies of the dynamics of mantle plume–mid-ocean ridge interaction, *Rev. Geophys.*, 41(4). 1017, doi: 10.1029/2002RG000117.

Ito, G., R. Dunn, and A. Li (2015), The origin of shear wave splitting beneath Iceland, *Geophys. J. Int.*, 201(3), 1297–1312, doi: 10.1093/gji/ggv078.

Ito, G. and J. Lin (1995), Oceanic spreading center–hotspot interactions: Constraints from along-isochron bathymetric and gravity anomalies, *Geology*, 23(7), 657–660, doi: 10.1130/0091-7613(1995)023⟨0657:OSCHIC⟩2.3.CO;2.

Ito, G., J. Lin, and C. W. Gable (1996), Dynamics of mantle flow and melting at a ridge-centered hotspot: Iceland and the Mid-Atlantic Ridge, *Earth Planet. Sci. Lett.*, 144(1), 53 –74, doi: 10.1016/0012-821X(96)00151-3.

Ito, G., J. Lin, and C. W. Gable (1997), Interaction of mantle plumes and migrating mid-ocean ridges: Implications for the Galápagos plume-ridge system, *J. Geophys. Res. Solid Earth*, 102(B7), 15403–15417, doi: 10.1029/97JB01049.

Ito, G., Y. Shen, G. Hirth, and C. J. Wolfe (1999), Mantle flow, melting, and dehydration of the Iceland mantle plume, *Earth Planet. Sci. Lett.*, 165(1), 81–96, doi: 10.1016/S0012-821X(98)00216-7.

Kellogg, L. H. and S. D. King (1997), The effect of temperature dependent viscosity on the structure of new plumes in the mantle: Results of a finite element model in a spherical, axisymmetric shell, *Earth Planet. Sci. Lett.*, 148(1), 13 –26, doi: 10.1016/S0012-821X(97)00025-3.

King, S. D. and C. Adam (2014), Hotspot swells revisited, *Physics of the Earth and Planetary Interiors*, 235, 66 –83, doi: 10.1016/j.pepi.2014.07.006.

Koptev, A., S. Cloetingh, E. Burov, T. François, and T. Gerya (2017), Long-distance impact of Iceland plume on Norway's rifted margin, *Scientific Reports*, 7(1), 10408, doi: 10.1038/s41598-017-07523-y.

McKenzie, D. and J. Sclater (1971), The evolution of the Indian Ocean since the Late Cretaceous, *Geophys. J. Int.*, 24(5), 437–528, doi: 10.1111/j.1365-246X.1971.tb02190.x.

Mittal, T. and M. A. Richards (2017), Plume-ridge interaction via melt channelization at Galápagos and other near-ridge hotspot provinces, *Geochem. Geophys. Geosyst.*, 18(4), 1711–1738, doi: 10.1002/2016GC006454.

Mittelstaedt, E. and G. Ito (2005), Plume-ridge interaction, lithospheric stresses, and the origin of near-ridge volcanic lineaments, *Geochem. Geophys. Geosyst.*, 6, Q06002, doi: 10.1029/2004GC000860.

Mittelstaedt, E., G. Ito, and J. van Hunen (2011), Repeat ridge jumps associated with plume-ridge interaction, melt transport, and ridge migration, *J. Geophys. Res. Solid Earth*, 116, B01102, doi: 10.1029/2010JB007504.

Montelli, R., G. Nolet, F. A. Dahlen, G. Masters, E. R. Engdahl, and S.-H. Hung (2004), Finite-frequency tomography reveals a variety of plumes in the mantle, *Science*, 303(5656), 338–343, doi: 10.1126/science.1092485.

Montelli, R., G. Nolet, F. A. Dahlen, and G. Masters (2006), A catalogue of deep mantle plumes: New results from finite-frequency tomography, *Geochem. Geophys. Geosyst.*, 7, Q11007, doi: 10.1029/2006GC001248.

Morgan, W. J. (1971), Convection plumes in the lower mantle, *Nature*, 230, 42–43, doi: 10.1038/230042a0.

Morgan, W. J. (1972), Deep mantle convection plumes and plate motions, *AAPG bulletin*, 56(2), 203–213.

Morgan, W. J. (1978), Rodriguez, Darwin, Amsterdam, ..., A second type of Hotspot Island, *J. Geophys. Res.*, 83(B11), 5355–5360, doi: 10.1029/JB083iB11p05355.

Mulyukova, E., B. Steinberger, M. Dabrowski, and S. V. Sobolev (2015), Survival of LLSVPs for billions of years in a vigorously convecting mantle: Replenishment and destruction of chemical anomaly, *J. Geophys. Res. Solid Earth*, 120(5), 3824–3847, doi: 10.1002/2014JB011688.

Nolet, G. and F. Dahlen (2000), Wave front healing and the evolution of seismic delay times, *J. Geophys. Res. Solid Earth*, 105(B8), 19043–19054, doi: 10.1029/2000JB900161.

Nolet, G., R. Allen, and D. Zhao (2007), Mantle plume tomography, *Chemical Geology*, 241(3), 248 –263, doi: 10.1016/j.chemgeo.2007.01.022.

Putirka, K. (2008), Excess temperatures at ocean islands: Implications for mantle layering and convection, *Geology*, 36(4), 283–286, doi: 10.1130/G24615A.1.

Ribe, N. M. (1996), The dynamics of plume-ridge interaction: 2. Off-ridge plumes, *J. Geophys. Res. Solid Earth*, 101(B7), 16195–16204, doi: 10.1029/96JB01187.

Ribe, N. M. and U. R. Christensen (1994), Three-dimensional modeling of plume-lithosphere interaction, *J. Geophys. Res. Solid Earth*, 99(B1), 669–682, doi: 10.1029/93JB02386.

Ribe, N., A. Davaille, and U. Christensen (2007), "Fluid dynamics of mantle plumes". *Mantle plumes*. Springer, 1–48.

Ribe, N., U. Christensen, and J. Theißing (1995), The dynamics of plume-ridge interaction, 1: Ridge-centered plumes, *Earth Planet. Sci. Lett.*, 134(1), 155 –168, doi: 10.1016/0012-821X(95)00116-T.

Richards, M. A., R. A. Duncan, and V. E. Courtillot (1989), Flood Basalts and Hot-Spot Tracks: Plume Heads and Tails, *Science*, 246, 103–107, doi: 10.1126/science.246.4926.103.

Schilling, J. G., G. Thompson, R. Kingsley, and S. Humphris (1985), Hotspot-migrating ridge interaction in the South Atlantic, *Nature*, 313, 187–191.

Schilling, J.-G. (1991), Fluxes and excess temperatures of mantle plumes inferred from their interaction with migrating mid-ocean ridges, *Nature*, 352, 397–403, doi: 10.1038/352397a0.

Schubert, G., D. L. Turcotte, and P. Olson (2001), *Mantle convection in the Earth and planets*. Cambridge Univ. Press, Cambridge, U. K.

Sleep, N. H. (1990), Hotspots and mantle plumes: Some phenomenology, *J. Geophys. Res.*, 95(B5), 6715–6736, doi: 10.1029/JB095iB05p06715.

Sleep, N. H. (1997), Lateral flow and ponding of starting plume material, *J. Geophys. Res.*, 102(B5), 10001–10012, doi: 10.1029/97JB00551.

Smith, W. H. F. and D. T. Sandwell (1997), Global Sea Floor Topography from Satellite Altimetry and Ship Depth Soundings, *Science*, 277(5334), 1956–1962, doi: 10.1126/science.277.5334.1956.

Sobolev, S. V., A. V. Sobolev, D. V. Kuzmin, N. A. Krivolutskaya, A. G. Petrunin, N. T. Arndt, V. A. Radko, and Y. R. Vasiliev (2011), Linking mantle plumes, large igneous provinces and environmental catastrophes, *Nature*, 477, 312–316, doi: 10.1038/nature10385.

Steinberger, B. (2000), Plumes in a convecting mantle: Models and observations for individual hotspots, *J. Geophys. Res.*, 105(B5), 11,127–11,152, doi: 10.1029/1999JB900398.

Suetsugu, D., T. Isse, S. Tanaka, M. Obayashi, H. Shiobara, H. Sugioka, T. Kanazawa, Y. Fukao, G. Barruol, and D. Reymond (2009), South Pacific mantle plumes imaged by seismic observation on islands and seafloor, *Geochem. Geophys. Geosyst.*, 10(11). Q11014, doi: 10.1029/2009GC002533.

Torsvik, T. H., M. A. Smethurst, K. Burke, and B. Steinberger (2006), Large igneous provinces generated from the margins of the large low-velocity provinces in the deep mantle, *Geophys. J. Int.*, 167(3), 1447–1460, doi: 10.1111/j.1365-246X.2006.03158.x.

van Keken, P. (1997), Evolution of starting mantle plumes: a comparison between numerical and laboratory models, *Earth Planet. Sci. Lett.*, 148(1), 1 –11, doi: 10.1016/S0012-821X(97)00042-3.

Whitehead, J. A. and D. S. Luther (1975), Dynamics of laboratory diapir and plume models, *Journal of Geophysical Research*, 80(5), 705–717, doi: 10.1029/JB080i005p00705.

Wilson, J. T. (1963), A possible origin of the Hawaiian islands, *Canadian Journal of Physics*, 41(6), 863–870, doi: 10.1139/p63-094.

Zhao, D. (2004), Global tomographic images of mantle plumes and subducting slabs: insight into deep Earth dynamics, *Physics of the Earth and Planetary Interiors*, 146(1), 3 –34, doi: 10.1016/j.pepi.2003.07.032.

Zhao, D. (2007), Seismic images under 60 hotspots: Search for mantle plumes, *Gondwana Research*, 12(4), 335 –355, doi: 10.1016/j.gr.2007.03.001.

2 How plume-ridge interaction shapes the crustal thickness pattern of the Réunion hotspot track

A version of this chapter has been published as Bredow, E., B. Steinberger, R. Gassmöller, and J. Dannberg (2017), How plume-ridge interaction shapes the crustal thickness pattern of the Réunion hotspot track, Geochem. Geophys. Geosyst., 18, 2930–2948, doi:10.1002/2017GC006875.

Abstract

The Réunion mantle plume has shaped a large area of the Earth's surface over the past 65 million years: from the Deccan Traps in India along the hotspot track comprising the island chains of the Laccadives, Maldives, and Chagos Bank on the Indian plate and the Mascarene Plateau on the African plate up to the currently active volcanism at La Réunion Island. This study addresses the question how the Réunion plume, especially in interaction with the Central Indian Ridge, created the complex crustal thickness pattern of the hotspot track. For this purpose, the mantle convection code ASPECT was used to design three-dimensional numerical models, which consider the specific location of the plume underneath moving plates and surrounded by large-scale mantle flow. The results show the crustal thickness pattern produced by the plume, which altogether agrees well with topographic maps. Especially two features are consistently reproduced by the models: the distinctive gap in the hotspot track between the Maldives and Chagos is created by the combination of the ridge geometry and plume-ridge interaction; and the Rodrigues Ridge, a narrow crustal structure which connects the hotspot track and the Central Indian Ridge, appears as the surface expression of a long-distance sublithospheric flow channel. This study therefore provides further insight how small-scale surface features are generated by the complex interplay between mantle and lithospheric processes.

2.1 Introduction

2.1.1 Geodynamic History of the Réunion Plume

The mantle plume currently inducing volcanic activities on La Réunion Island in the western Indian Ocean (Figure 2.1) has continuously affected the surface of the Earth over the past 65.5 Myr (e.g., Duncan, 1990; Courtillot et al., 2003; Hofmann et al., 2000; Schoene et al., 2015). When the ascending plume head arrived at the base of the lithosphere and induced partial melting, the subsequent surface volcanism created the Deccan Traps in India, a Large Igneous Province (LIP) that marks the spatial and temporal beginning of the Réunion hotspot track (Richards et al., 1989). Most of these continental flood basalts were erupted in less than 1 Myr (Courtillot et al., 1986, 1988) and this relatively short period of vigorous magmatic activity is associated with the mass extinction at the Cretaceous/Tertiary boundary (Courtillot and Renne, 2003). Between 67 and 51 Ma, India moved with anomalously high plate velocities

of up to 16 cm/yr, which van Hinsbergen et al. (2011) partly attributed to the Réunion plume, since the plume head impinging on the lithosphere may have acted as a lubricant to accelerate the plate. Cande and Stegman (2011) proposed the rapid movement of the Indian plate to be caused only by the pushing force of the rising plume head. The Indian plate and later the African plate moved above the relatively fixed plume tail and created the Réunion hotspot track (Duncan and Hargraves, 1990; Duncan and Richards, 1991), a linear chain of age-progressive islands, seamounts, and plateaus (Figure 2.1). From its initiation at the Deccan Traps, the hotspot track can be followed southward along the island chains of the Laccadives, the Maldives and across a rather uncommon gap along the Chagos Bank on the Indian and Australian plate and southwestward along the Mascarene Plateau including the Mascarene Islands Mauritius and Réunion on the African plate (Duncan, 1990). Seafloor-spreading at the Central Indian Ridge has split the once continuous hotspot track between the Chagos Bank and the Northern Mascarene Plateau (McKenzie and Sclater, 1971). Today, the frequent eruptions of the Piton de la Fournaise at La Réunion represent the surface activities of the plume (Richards et al., 1989).

An unusual feature associated with the Réunion hotspot is the third Mascarene Island Rodrigues (Figure 2.1), situated above a narrow volcanic ridge that seems to connect a recent part of the hotspot track with the closest segment of the Central Indian Ridge. Already Morgan (1978) interpreted the Rodrigues Ridge as the result of a sublithospheric flow channel created by long-distance plume-ridge interaction. Even more exceptional for a hotspot track is the hypothesis of Torsvik et al. (2013) and Ashwal et al. (2017), who analyzed the ages of Mauritian zircons from basaltic beach sand samples and zircons recovered from trachytic rocks, respectively, and concluded that Mauritius and the Mascarene Plateau overlie and conceal a Precambrian microcontinent underneath the hotspot track.

2.1.2 Deep Origin of the Réunion Plume

Apart from the LIP, the hotspot track and the still active volcanism, several additional characteristics indicate that the origin of the Réunion hotspot is a deep plume rising from the lowermost mantle (e.g., Morgan, 1971; Courtillot et al., 2003). A broad topographic swell around the present-day hotspot has been noted by Crough (1983) and Davies (1988). The Réunion plume is considered sufficiently buoyant to ascend through the entire mantle and cause volcanic activity on the surface (Sleep, 1990; Courtillot et al., 2003). Geochemical observations report a high isotopic $^3He/^4He$ ratio of volcanic rocks from La Réunion Island that differs from typical values of mid-ocean ridge basalt (MORB) (Farley and Neroda, 1998; Courtillot et al., 2003). Around 20°S along the Central Indian Ridge, a geochemical anomaly has been associated with plume-ridge interaction by Mahoney et al. (1989), Schilling (1991), Nauret et al. (2006), and Füri et al. (2011). Furthermore, the reconstructed eruption site of the Deccan Traps as well as the present-day hotspot position are located almost exactly above the margin of the African Large Low Shear Velocity Province (LLSVP) (Garnero et al., 2007), which is considered to act as a plume generation zone at the core-mantle boundary (Torsvik et al., 2006; Burke et al., 2008). Seismic evidence of a deep Réunion plume has been implied by previous global tomography

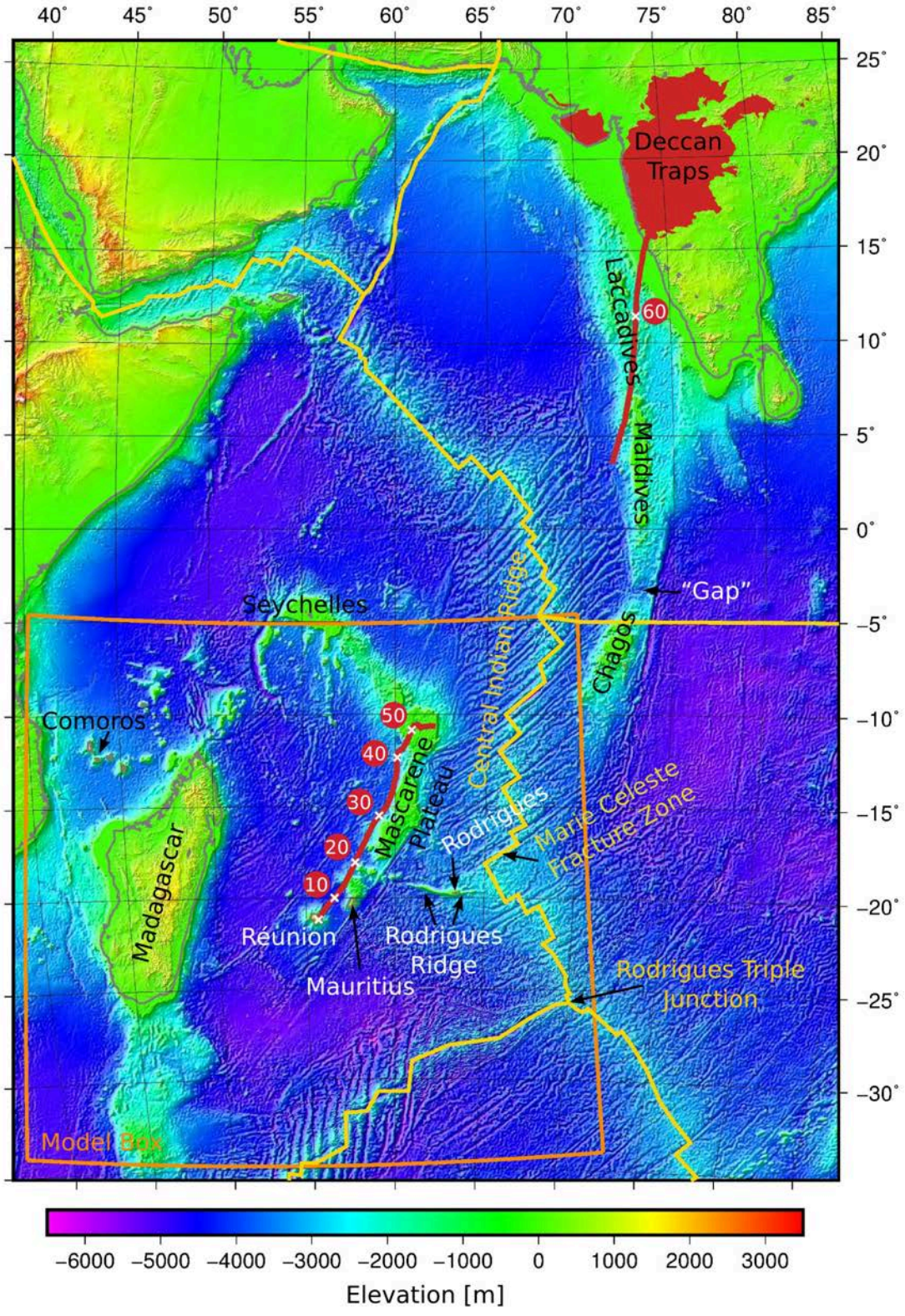

Figure 2.1: Topographic map of the northwestern Indian Ocean showing the entire hotspot track from the Deccan Traps in India to the currently active plume position at Réunion Island. The red line shows the predicted hotspot track after Torsvik et al. (2013) with plume positions (in Ma), the extent of the model box is depicted by the orange outline and plate boundaries are shown as yellow lines.

studies (Montelli et al., 2004, 2006; French and Romanowicz, 2015) and is currently investigated by the French-German RHUM-RUM project (Réunion Hotspot and Upper Mantle – Réunions Unterer Mantel), the largest seismological experiment to image a deep oceanic mantle plume so far (Barruol and Sigloch, 2013).

2.1.3 Motivation for Modeling the Réunion Plume

The main purpose of this study, which is part of the RHUM-RUM project, is to investigate how the Réunion plume, especially in interaction with the Central Indian Ridge, created the hotspot track, i.e., if the current crustal thickness pattern in the Indian Ocean may be explained by a numerical model with a plume. Apart from the large-scale pattern, two smaller features and their origins are particularly interesting: first, it remains unclear which mechanisms in this specific geographic setting formed the gap between the Maldives and the Chagos Bank and second, the Rodrigues Ridge was suggested to be the surface expression of a sublithosphere flow channel by Morgan (1978). However, there is no quantitative analysis so far that shows which dynamic processes might lead to melt production along the Rodrigues Ridge and thus support the feasibility of Morgan's hypothesis.

2.2 Model Setup

2.2.1 Numerical Model

The model setup for studying the Réunion plume is based on the procedure described in Gassmöller et al. (2016), which presented several software extensions for ASPECT in order to focus on a specific mantle plume – in that case the Tristan da Cunha plume in the South Atlantic. ASPECT (Advanced Solver for Problems in Earth's ConvecTion) is an open-source mantle convection code using finite elements and adaptive meshes (Kronbichler et al., 2012; Bangerth et al., 2017). The extended ASPECT version of Gassmöller et al. (2016) was modified as necessary for creating a regional numerical model of the upper part of the Réunion plume.

The model domain is a three-dimensional Cartesian box, extending 3300 km × 3300 km horizontally and 660 km vertically (see Figure 2.2a). To cover the entire geodynamic development of the Réunion plume, the time evolution starts at 80 Ma. The boundary conditions for the box are chosen in such a way that the model explicitly represents the region around the Réunion plume: on the top boundary and the uppermost 200 km of the side boundaries, reconstructed tectonic plate velocities are prescribed to simulate plate motions. In this simplified approach based on the reference frame of Doubrovine et al. (2012), the velocities of each plate are kept constant for 10 Myr intervals, but the position of the mid-ocean ridges are updated in 1 Myr intervals (interpolated from the plate reconstructions of Torsvik et al. (2010)).

Below 200 km at the side boundaries and at the bottom of the box, time-dependent global flow velocities are prescribed to take into account the large-scale mantle circulation. The mantle flow velocities are derived from a global mantle convection model with a lower resolution (an update

of Doubrovine et al. (2012)), which derives the present-day mantle flow from a density model based on seismic tomography, a surface boundary condition in agreement with plate motions and the radial viscosity structure of Steinberger and Calderwood (2006), whereas the mantle flow in the past is computed by backward-advecting density anomalies with global plate motions. The global flow on the edges of the model box does not exceed a few cm/yr. Its direction is dominated by the large-scale convection cell from the upward flow above the African LLSVP southwest of the box toward the downward flow at the Sunda Trench northeast of the box.

At 200 km depth at the side boundaries, approximately corresponding to the lithosphere-asthenosphere boundary, the plate velocities, and global flow velocities are interpolated to ensure a smooth transition between the different velocity values. More details about the boundary conditions and their conversion into Cartesian coordinates suitable for the box geometry can be found in Gassmöller et al. (2016).

Regarding the hotspot motion model, the plume position in the coarser global model is tracked over time at the appropriate depth of 660 km and used as time-dependent plume inflow position at the bottom of the box in order to set up a reference model where the hotspot surface position is approximately matched. The inflow position moves relatively slow: approximately 150 km eastward and 200 km southward over 67 Myr.

The initial temperature profile of the model is adiabatic with a potential surface temperature of 1613 K and a nonadiabatic cold lithospheric layer on top. The base of the lithosphere is considered to be represented by the 1613 K isotherm, which initially varies between 10 and 210 km depth in the reference model (and between 10 and 300 km depth in model variation LithThickNew). The initial lithosphere thickness is converted into half-space cooling ages and temperature profiles to be prescribed as initial temperature condition and later as boundary condition (updated in 1 Myr intervals) in ASPECT (see section 2.2.2). Note that except for the initial state of the model, the lithosphere thickness is only imposed on the boundaries – inside the model domain, the lithosphere thickness evolves fully dynamically. The viscosity depends on the temperature and considers lateral variations besides the radial structure of Steinberger and Calderwood (2006) (see section 2.2.3).

The occurrence of temperature-dependent and pressure-dependent melting is calculated based on the parametrization for batch melting of anhydrous peridotite (Katz et al., 2003). As a postprocessing step, the melt generated in each time step is instantly extracted, accumulated at the surface and moved along with the tectonic plate motions (instant melt extraction method of Gassmöller et al. (2016)). This procedure assumes that melt ascends through channels and dikes in the lithosphere and produces magmatic crust vertically above the origin of the melt. Note that lateral melt motion is neglected since the ascent through channels and dikes occurs much faster than motion in the mantle. The final result shows the present-day crustal thickness pattern of the Réunion hotspot track (see section 2.3.2).

Every model run is computed twice, using the net mass flux from the first model run to correct the velocity boundary conditions used in the second computation, to assure that there is no net mass influx or outflux. This compensates in particular for the plume inflow. Only the

second computation is presented as a result and interpreted. The boundary velocity correction is equally distributed over the asthenosphere (below 200 km depth) of the four side boundaries and except for the time of the plume head inflow, the corrections do not exceed 0.3 cm/yr.

Since every model has to be computed twice, each run taking about 10 h on 768 processors, each variation of the model requires approximately 15,000 core hours of computing time and has about 12 million degrees of freedom. The adaptive mesh refinement enables a better resolution of the plume and the lithosphere, where melting occurs. The smallest mesh cells in the uppermost 200 km have a size of 10.3 km.

2.2.2 Lithosphere Thickness Values as Initial and Boundary Conditions

The geodynamic processes in the Western Indian Ocean are challenging for a localized model setup. At the start time of the model, the top of the box is not completely covered by continents, therefore an initially homogeneous lithosphere thickness is rather unrealistic. Another intricacy is caused by the plate motions on top of the box. Since they do not symmetrically diverge from the Central Indian Ridge, most of the lithosphere thickness is controlled by the boundary conditions instead of being self-consistently generated by the model. Therefore, the global lithospheric thickness model of Steinberger (2016) (or model LITHO1.0 of Pasyanos et al. (2014) with a formal lateral resolution of 1° in modified model LithThickNew) was used to initialize and prescribe the thermal structure at the model boundaries and the time of model initiation according to the backward rotated positions of oceans and continents. (Note that Steinberger (2016) uses a different isotherm to define lithosphere thickness.) The backward-rotation was carried out using absolute plate motions from Doubrovine et al. (2012) and relative rotations from Torsvik et al. (2010). In the oceans, the lithosphere thickness is derived from the Earthbyte ocean floor age (version 3.6 of Müller et al. (2008)), i.e., the present-day age grid is backward-rotated and converted to a half-space cooling temperature profile using a thermal diffusivity value $\kappa = 8 \times 10^{-7} \mathrm{m^2 s^{-1}}$ (more details available in supporting information Text S4 in Gassmöller et al. (2016)).

Note that the microcontinent described by Torsvik et al. (2013) and Ashwal et al. (2017) is not considered in these boundary conditions, since the age grid of Müller et al. (2008) (with a formal resolution of 6 arc min) differentiates only between continents and oceans and apart from the Seychelles, the entire area of the microcontinent is classified as ocean.

2.2.3 Dehydration Rheology and Depletion Buoyancy

When rising mantle material crosses the solidus and starts to melt, water is extracted and this dehydration effect leads to an immediate viscosity increase that stiffens the lithosphere and suppresses buoyancy-driven flow, lowering the melt production rate. Including a dehydration rheology is therefore a mechanism known to reduce the melting rate and thus produce thinner crust (Ito et al., 1999; Howell et al., 2014). Due to the neglect of this process, Gassmöller et al. (2016) report very high crustal thickness values in some small regions of their result, which

inspired the incorporation of a dehydration rheology for the Réunion model.

The numerical implementation of this sudden viscosity jump is achieved by a preexponential factor A controlling the viscosity. While Ito et al. (1999) chose the constant factor of $A = 1$ below and $A = 50$ above the dry solidus, Howell et al. (2014) used a term depending on the percentage of water dissolved in the solid mantle material: $A = (C/C_0)^{-1}$ describes the dependence on the water concentration in the solid, C, proportionally to the water dissolved at the beginning, C_0, if a dehydration effect is desired. The equivalent dehydration prefactor after Katz et al. (2003) yields

$$A = \left(\frac{C}{C_0}\right)^{-1} = \frac{D_{H_2O} + F(1 - D_{H_2O})}{D_{H_2O}} \tag{2.1}$$

where D_{H_2O} is a bulk partitioning coefficient with a value of 0.01 and F is the current weight fraction of melt or degree of depletion. In the absence of melt, i.e., $F = 0$, the viscosity should not be altered by the dehydration prefactor, therefore the denominator is D_{H_2O}. The viscosity finally simulated in the Réunion plume models combines the dehydration rheology from Howell et al. (2014) and a slightly modified version of the temperature-dependence and depth-dependence in Steinberger and Calderwood (2006) and thus is a product of the dehydration prefactor, the radial viscosity $\eta_r(z)$ and the lateral viscosity:

$$\eta(z,T) = \frac{D_{H_2O} + F(1 - D_{H_2O})}{D_{H_2O}} \cdot \eta_r(z) \cdot \exp\left(-\frac{(E + pV)(T - T_{\mathrm{adi}}(z))}{nRTT_{\mathrm{adi}}(z)}\right) \tag{2.2}$$

where $T_{adi}(z)$ is the depth-dependent adiabatic temperature, n is the stress exponent, and R is the universal gas constant.

Further, the depth-dependent activation enthalpy profile $H(z)$ of Steinberger and Calderwood (2006) was replaced by the term $E+pV$ with the activation energy $E = 3.75 \times 10^5$ J/mol and the activation volume $V = 6 \times 10^{-6}$ J/(mol Pa) and $n = 1$ after Hirth and Kohlstedt (2003). This rheology leads to more realistic viscosities, because only considering the temperature dependence of viscosity from Steinberger and Calderwood (2006) but disregarding the effect that higher strain rates inside a plume yield lower viscosities would underestimate the effective lateral viscosity variations (Christensen, 1983). The viscosity contrast between plume and ambient mantle is increased from a factor of 4 before the change to a range of 6 – 20 afterward.

Additionally, the density calculation in this study includes a depletion density decrease of up to 15 kg/m^3, which increases the effective buoyancy when melt is extracted (e.g., Dupeyrat et al., 1995; Manglik and Christensen, 1997; Ribe and Christensen, 1999).

2.2.4 Reference Model and Parameter Variations

The parameters for the reference model were chosen in accordance with published values and varied in a series of additional simulations in order to constrain the influence of each parameter on the predicted pattern and thickness of the hotspot track (see Table 2.1 for an overview of the model setups).

The plume head inflow at the bottom of the box is simulated by a spherical velocity anomaly (a circular inflow area, which changes its radius over time) with an excess temperature ΔT,

Table 2.1: Model Setups

Model	Excess Temperature ΔT_{tail} (K)	Inflow Velocity v_{tail} (cm/yr)	Inflow Radius R_{tail} (km)	Buoyancy Flux B_{tail} (kg/s)
Reference	250	6.0	140	1250 – 1500
DeltaT200	200	4.8	140	700 – 850
DeltaT300	300	7.2	140	2100 – 2450
Flux950	250	5.6	120	850 – 1050
Flux1900	250	6.3	160	1650 – 2050
FixedPlume	Plume inflow position fixed at its initial position below Deccan Traps			
PlumePosVar5	Hotspot motion starts further north and ends further west			
PlumePosVar9	Hotspot moves westward from its initial position below Deccan Traps			
LithThickNew	Lithosphere thickness based on Pasyanos et al. (2014)			
HomLith	Homogeneous lithosphere thickness as initial and boundary conditions			
NoGlobalFlow	Without global flow (pure plume buoyancy flux = 1150 kg/s)			
NoDehyd	No dehydration rheology			
NoDepl	No depletion buoyancy			
DefaultVisc	Viscosity contrast of Gassmöller et al. (2016)			
+ respective NoPlume models in order to extract the contribution of the plume				

radius R, and a vertical inflow velocity v. The parameters of the plume head in the reference model are $\Delta T_{head} = 300\,\mathrm{K}$, $R_{head} = 250\,\mathrm{km}$, and $v_{head} = 20\,\mathrm{cm/yr}$ corresponding to the values of Gassmöller et al. (2016), based on the argument that the magma volumes of the Paraná-Etendeka flood basalts and the Deccan Traps are similar. More specifically, published volumes for the Deccan Traps range from $1 \times 10^6\,\mathrm{km}^3$ to $> 2 \times 10^6\,\mathrm{km}^3$ (Officer et al., 1987; Jay and Widdowson, 2008; Turcotte and Schubert, 2002; Richards et al., 1989; Todal and Eldholm, 1998; Courtillot et al., 2003). At 68 Ma, the plume head reaches the boundary between lower and upper mantle and enters the reference model. It continues ascending up to the base of the lithosphere and the first melt is generated at 66 Ma, which represents the first volcanic activities at the Deccan Traps site. This timing agrees with geological age studies (e.g., Courtillot et al., 2003).

The plume head is followed by the plume tail, prescribed as an inflow with a Gaussian circular temperature and velocity distribution at the bottom of the box. Estimations of the excess temperature of the Réunion plume tail ΔT_{tail} cover a wide range of values between 174 and 240 K (Schilling, 1991; Putirka, 2008; Turcotte and Schubert, 2002; Sleep, 1990; Herzberg and Gazel, 2009). The value chosen for the plume inflow at the bottom of the reference model is 250 K and varied between 200 and 300 K in model DeltaT200 and DeltaT300, respectively. These values exceed the published estimates to account for the heat loss of approximately 40 K due to adiabatic cooling and thermal conduction while the plume material rises from the inflow depth of 660 km to the depth of the melting region. Consequently, the plume excess temperature upon

melting is approximately 210 K and within the range of published estimates. In the reference model, $v_{tail} = 6$ cm/yr and $R_{tail} = 140$ km.

The plume buoyancy flux can be determined as $B_{tail} = \pi \cdot R_{tail}^2 \cdot v_{tail} \cdot (\rho_{mantle} - \rho_{tail})$, where ρ_{mantle} is the density of the ambient mantle and ρ_{tail} is the plume density (Turcotte and Schubert, 2002). Estimated values for the Réunion plume tail are distributed over a broad spectrum from 900 to 1900 kg/s (Davies, 1988; Schilling, 1991; Turcotte and Schubert, 2002; Sleep, 1990). In the reference model, the buoyancy flux ranges from 1250 to 1500 kg/s. It varies over time, because the global flow velocities at the bottom boundary interfere with the plume inflow velocity. The pure plume buoyancy flux can be measured in the model without global flow and yields 1150 kg/s. The variation of B_{tail} for other model configurations is achieved indirectly by changing v_{tail} and R_{tail} while ΔT_{tail} remains constant and yields ranges between 850 and 1050 kg/s (model Flux950) and 1650 and 2050 kg/s (model Flux1900).

Further parameters that were varied to examine their respective effects are the hotspot motion model (manually varied to a fixed or differently moving plume inflow position), the lithosphere thickness values used as initial and boundary conditions (using different reconstructions or a simplified constant lithosphere thickness), the global flow, the dehydration rheology, the depletion buoyancy, and the implemented viscosity contrast.

2.3 Results

2.3.1 Model Development

Figures 2.2 and 2.3 illustrate the chronological development of the plume in the reference model. While Figure 2.2 shows the plume-ridge interaction in relation to the plate motions prescribed as top boundary conditions, Figure 2.3 illustrates how the plume interacts with the relief of the lithospheric base. For an animated view see supporting information Movie 2.S1; Figures 2.S1 and 2.S2 show corresponding figures of model NoGlobalFlow.

At 65 Ma, the Indian plate is moving extremely fast with about 16 cm/yr (Figure 2.2a), while the plume head reaches the base of the thick continental lithosphere of India (Figure 2.3a), underneath the reconstructed site of the Deccan Traps. The onset of melting illustrates the beginning volcanic activities of the LIP, which agrees temporally with identified geological ages (e.g., Courtillot et al., 2003). However, melting does not occur at the location of the Deccan Traps, because the plume material flows southeastward (despite the northeastward plate motions and global flow) toward thinner oceanic lithosphere before it starts to melt, a process known as upside-down drainage (Sleep, 1997).

Over the following 5 Myr, the bulk of the asymmetrically shaped Deccan Traps southeast of the Indian continent is generated in the model (Figures 2.2b and 2.3b). Geological studies concluded that most of the LIP was formed within 1 Myr (Courtillot et al., 1986, 1988), but this process takes longer in the simulation. These slightly longer time scales are likely caused by the assumption of a pure diffusion creep rheology – dislocation creep would lower the viscosity within the plume and accelerate its spreading below the lithosphere – and mechanically treating

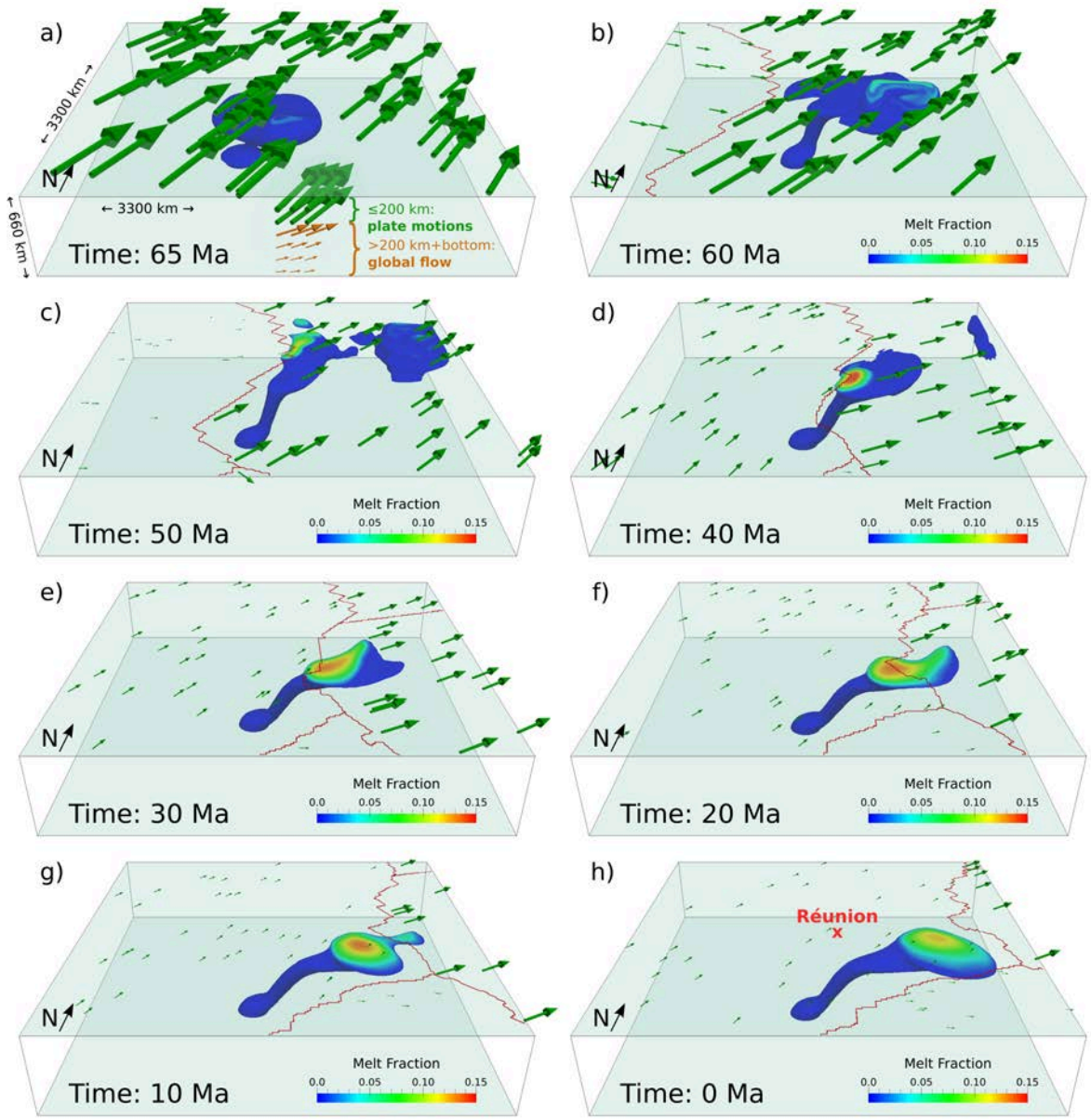

Figure 2.2: Development of the reference model: plume and plume-ridge interaction over time. The plume is represented by the $\Delta T = 100\,\mathrm{K}$ isosurface and colored according to the melt fraction. Mid-ocean ridges are marked as red lines, the plate velocities are depicted by green arrows. (a) Additionally illustrates the velocity side boundary conditions: orange arrows show the global flow on the same scale as the plate motions. (h) Represents the present-day state and shows the position of Réunion Island.

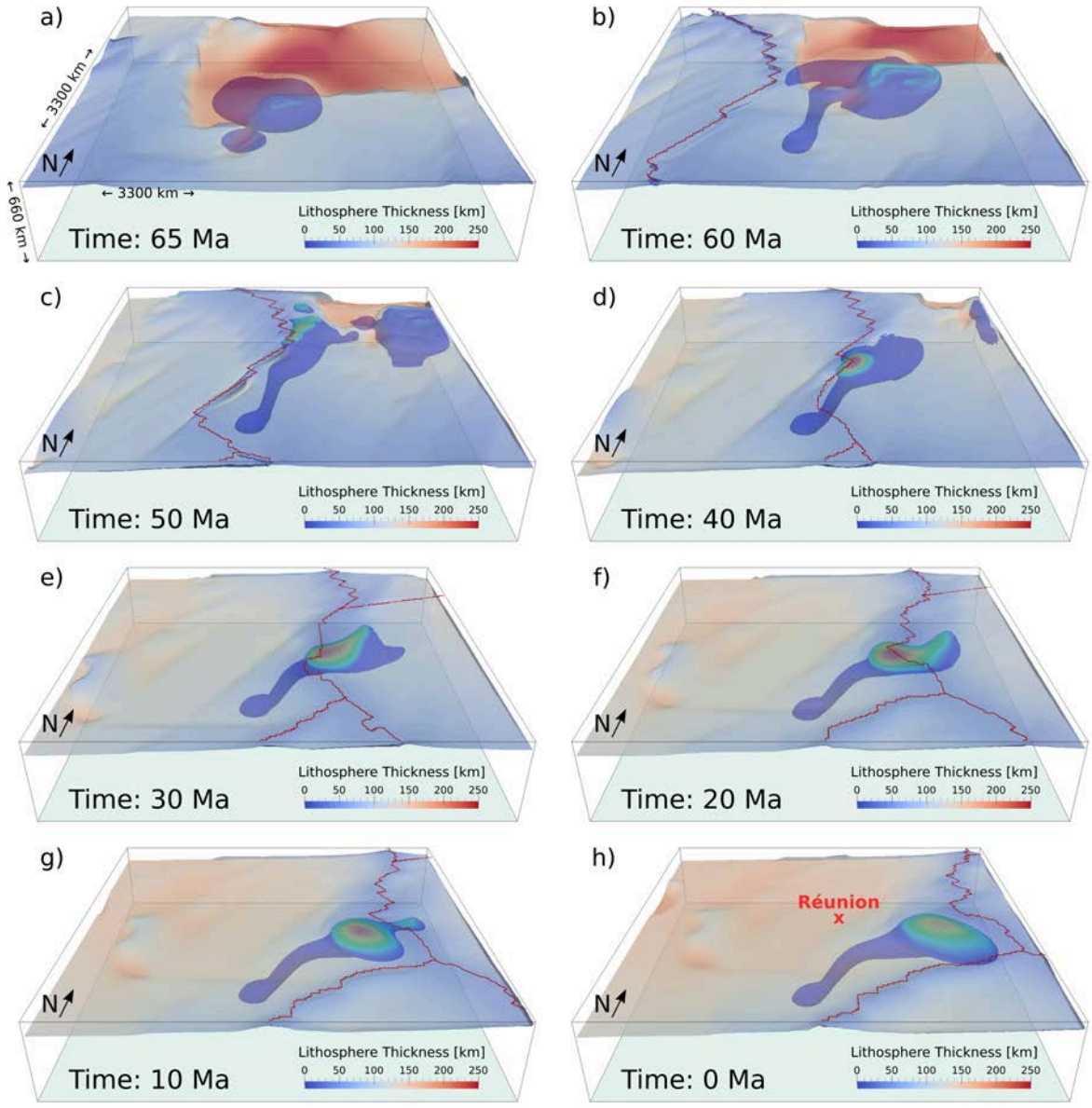

Figure 2.3: Development of the reference model: lithospheric thickness evolution and plume-ridge interaction over time. The plume is colored according to the melt fraction (as in Figure 2.2), mid-ocean ridges are marked as red lines and the base of the lithosphere is color-coded according to the depth. (h) Represents the present-day state and shows the position of Réunion Island.

the material as solid, neglecting the thinning of the lithosphere that would be induced by the transport and freezing of melt (Sobolev et al., 2011). Note how the initially vertical plume tail starts to be tilted toward the northeast, due to the plate motions and especially the global flow (see supporting information Figures 2.S1 and 2.S2 for a comparison to the model without global flow). In accordance with the plate motions and plate boundaries of Doubrovine et al. (2012) and Torsvik et al. (2010), the mid-ocean ridge between the Indian and the African plate appears in the model domain at 61 Ma and approaches the plume from the west afterward.

At 50 Ma, the Indian plate has slowed down from the record velocities, but is still moving northeastward (Figure 2.2c), causing India and the Deccan Traps to leave the model domain. The plume is now in the vicinity of the Central Indian Ridge and gets captured. Plume-ridge interaction increases the melt fraction and initiates the beginning of the on-ridge hotspot track. Note that the lithospheric thickness close to the ridge is self-consistently determined by the model (Figure 2.3c), while boundary conditions determine the thickness in the west and south.

At 40 Ma, major plume-ridge interaction takes place with the highest melt fraction of 14.5 % above the plume (Figures 2.2d and 2.3d). And while the Central Indian Ridge continues to move northeastward, the absolute plate motions at both sides of the ridge do not move apart symmetrically, but in similar directions and at increasingly different speeds.

In Figures 2.2e and 2.3e, most of the plume is located below the African plate, but the plate motions still push it toward the ridge, thereby increasing the tilt of the plume tail. Consequently, melting still occurs at the ridge, not beneath the African plate. This differs significantly from other hotspots such as Tristan, where the plume jumps completely to the other plate due to plate motions directed away from both sides of the Mid-Atlantic Ridge (Gassmöller et al., 2016).

In the subsequent evolution of the simulation, the plume moves further underneath the African plate, while plume and ridge are still interacting (Figures 2.2f and 2.3f). At 10 Ma, the upper part of the plume shape becomes more spherical and off-ridge-like, but it is still connected to the ridge (Figures 2.2g and 2.3g). From the west, Madagascar and the eastern tip of Africa move into the model domain (Figures 2.3e – 2.3h), agreeing with the extent of the model box in Figure 2.1. Figures 2.2h and 2.3h represent the present-day state of the plume. The tail is extremely tilted – stronger than in the global model, which was used to determine the plume inflow position in the model box – and stretched toward the ridge and while the shape resembles an off-ridge state, melting does not occur at the position of the plume arrival approximately below La Réunion Island, but only much closer toward the ridge below thinner lithosphere.

2.3.2 Predicted Crustal Thickness Map

The crustal thickness map (Figure 2.4) is computed as described in section 2.2.1 and shows the present-day pattern of the Réunion hotspot track as predicted by the numerical model. For reasons of clarity, the figure shows only the crust produced by the plume and neglects the crust that is generated separately at the mid-ocean ridges. This is achieved by subtracting the result of the same model without a plume from the result of the original model, thus leaving the contribution of the plume.

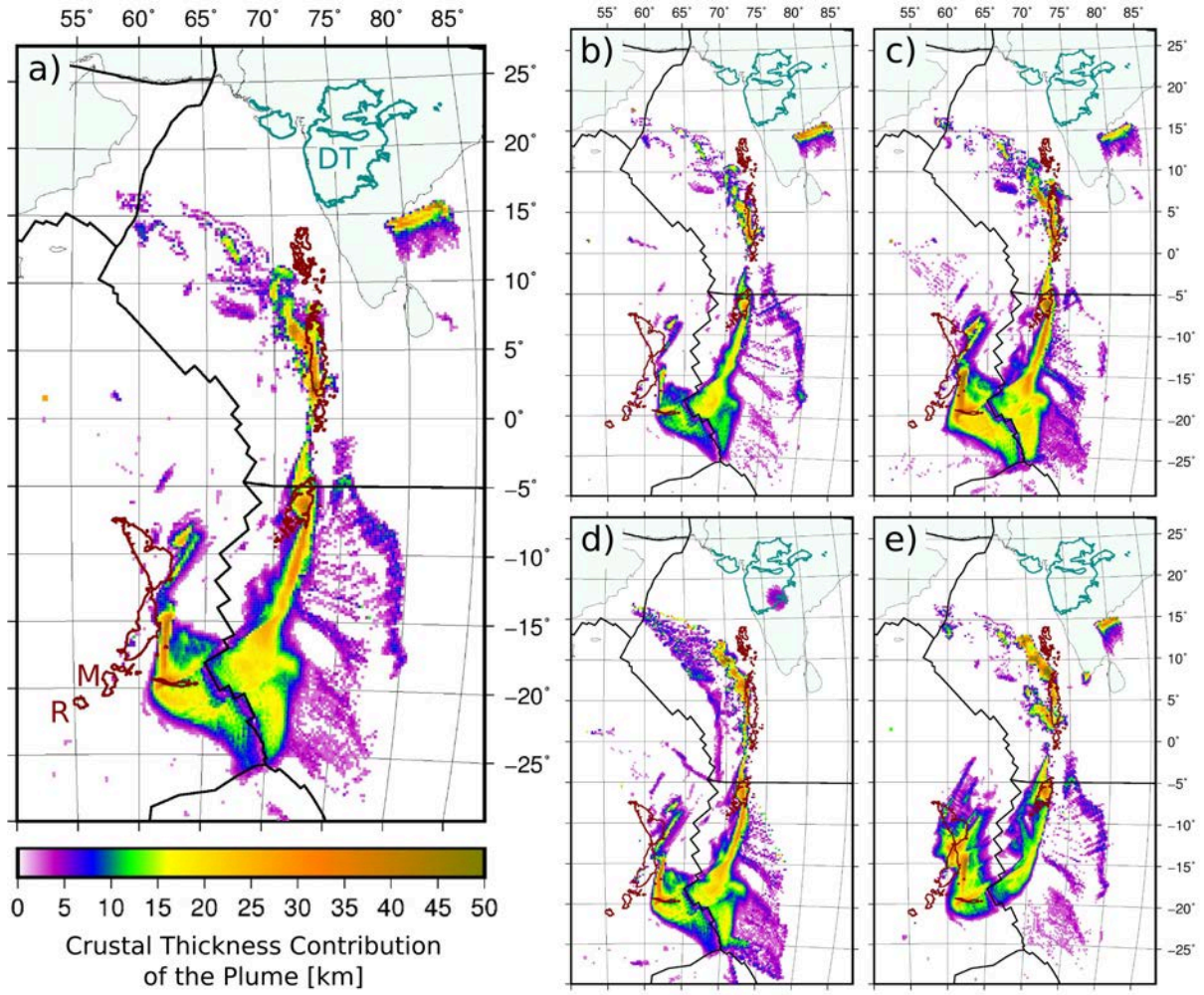

Figure 2.4: Present-day model state: crustal thickness pattern solely produced by the plume in various models. (a) Reference Model without any crust at the Deccan Traps (DT) or close to Mauritius (M) or Réunion (R). (b) DeltaT200, (c) DeltaT300, (d) HomLith, and (e) NoGlobalFlow. The dark red outlines show the observed hotspot track, represented by the -1500 m topography contours.

Assuming that topography and crustal thickness correspond to each other, the general resemblance with the currently observable hotspot track is evident (dark red outlines in Figure 2.4 or topography in Figure 2.1). Accurate comparisons can also be achieved with crustal thickness estimates from previous studies in this region, either determined by gravity anomaly inversion (such as shown in Figure 1 in Torsvik et al. (2013), which reaches maximum crustal thickness values of about 35 km in several areas of the hotspot track), based on seismic refraction profiles (such as Charvis et al. (1999) and Gallart et al. (1999)) or obtained from receiver function studies (such as Gupta et al. (2010) or Fontaine et al. (2015)). Apart from single peak values, the maximum crustal thickness of Figure 2.4a is about 45 km. More detailed comparisons for individual islands are described in section 2.4.2.

While many features of the observed hotspot track are matched well by the model, one prominent disagreement is the position of the Deccan Traps. Although the plume reaches the base of the lithosphere below the observed location of the LIP, the continental lithosphere of India is too

thick to enable melting in the model. Possible explanations for this disagreement are discussed in section 2.4.1.

The Laccadives and Maldives, however, appear as island chains at their correct positions (although the northern end of the Laccadives seems to be misplaced along with the Deccan Traps). Moreover, a narrow gap in the track is visible around 2° S between the Maldives and Chagos. This result remarkably coincides with the topography and is generated even though the plume inflow in the model is continuous and unchanged over time. The physical processes creating the gap are described in detail in section 2.3.4.

The shape of the predicted Chagos Bank resembles the topographic appearance as well. Further south on the Australian plate, the model predicts a wide area covered by crust that is not observed in the topography. This is caused by the long-term plume-ridge interaction already noted during the model evolution. On the African side, the Mascarene Plateau appears shifted to the East and not as prominent as in the topography. As seen in the model development, no crust at all is generated at Mauritius or La Réunion Island. Consequently, the youngest part of the hotspot track differs from observations, although the plume arrives at the base of the lithosphere close to La Réunion Island, and potential reasons for this are discussed in section 2.4.1.

An interesting young feature that nevertheless fits the observations is the long crustal segment heading from Mauritius toward the Central Indian Ridge – it is slightly rotated (trending from east-northeast to west-southwest compared to the east-west running topographic feature), but clearly resembles the shape of the Rodrigues Ridge. A thorough explanation for the origin of this feature can be found in section 2.3.5.

2.3.3 Effects of Parameter Variations

Figures 2.4b – 2.4e show a selection of crustal thickness maps achieved by varying one parameter in contrast to the reference model in each case. Additional maps can be found in supporting information Figure 2.S3. In particular, the properties of the plume were varied to investigate which model generates a realistic crustal thickness, and the plume inflow position over time was varied to illuminate which hotspot motion model matches the observed distribution of magmatic crust best. To ensure that the inflow velocity of the plume at the bottom of the model domain stays consistent with the velocity of the plume inside the model for different model setups, the plume excess temperature ΔT_{tail}, the inflow velocity v_{tail}, and the inflow area $A_{tail} = \pi R_{tail}^2$ are changed collectively, such that $\Delta T_{tail}\, A_{tail}\, v_{tail}^{-1} = \text{const.}$ in agreement with Stokes' law for the rising or sinking velocity of a sphere in a viscous medium. The main results of the parameter variations are as follows:

1. Decreasing the excess temperature of the plume tail to 200 K (model DeltaT200, Figure 2.4b) results in a smaller amount of crust distributed over a smaller area and reduces the maximum crustal thickness to about 40 km. Increasing the excess temperature to 300 K (model DeltaT300, Figure 2.4c) has the opposite effect and yields about 50 km of maximum crustal thickness.

2. Varying the plume's buoyancy flux (models Flux950 and Flux1900) has very similar effects: the amount of crust, the thickness, and width of the hotspot track decrease with decreasing buoyancy flux, while an increase has the contrary effect.

3. Keeping the plume inflow position constant at its initial position underneath the Deccan Traps (model FixedPlume) alters the recent part of the hotspot track such that it fits the topographic map slightly better than the result of the reference model.

4. Even for a plume motion starting 140 km further north and ending 400 km west of the respective positions of the reference model (model PlumePosVar5), the Deccan Traps are still misplaced on thin oceanic lithosphere. Also the tilt of the plume tail gets even stronger and present-day melting still takes place at the Central Indian Ridge, not closer to La Réunion.

5. In model PlumePosVar9, the plume inflow starts at the same position as in the reference model, but moves westward in order to position the present-day plume underneath La Réunion Island at the boundary between lithosphere and asthenosphere. However, melting is still not initiated at La Réunion.

6. Model LithThickNew uses input files based on the LITHO1.0 model of Pasyanos et al. (2014) with the intention of using a different lithosphere thickness distribution underneath India that might lead to correctly located Deccan Traps, but the result shows only minor differences from the reference model.

7. Switching to the simplified assumption of a homogeneous lithosphere thickness with a half-space cooling age of 55 Myr (model HomLith, Figure 2.4d) enables melting at the site of the Deccan Traps, because the uniformly 125 km thick lithosphere is much thinner than the continental lithosphere in the reference model.

8. Gassmöller et al. (2016) reported the strong impact of the global flow on the tilt of the plume tail and the associated change of the melt volume. Despite the changes in rheology, this observation seems to be equally valid in the case of the Réunion model (model NoGlobalFlow, Figure 2.4e). Altogether, the crustal thickness pattern without applied global flow seems to match the topographic pattern better than the result of the reference model, especially in the southern part of the hotspot track and the Mascarene Plateau, because the much less tilted plume tail positions the plume much earlier underneath the African plate (see supporting information Figures 2.S1 and 2.S2).

9. Excluding the rheological effect of dehydration (model NoDehyd) leads to an enormously increased crustal thickness exceeding 100 km.

10. Neglecting the effect of the depletion buoyancy (model NoDepl) hardly differs from the result of the reference model.

11. In model DefaultVisc, the viscosity inside the plume is higher and the viscosity contrast between plume and ambient mantle is lower than in the reference model. This leads to a slightly broader and less tilted plume, but does not significantly change the crustal thickness pattern.

In summary, regarding the properties of the plume, model DeltaT200 with a plume temperature of 200 K and a buoyancy flux of ∼800 kg/s produces a maximum crustal thickness of about 40 km that agrees best with the maximum of about 35 km reported by Torsvik et al. (2013). Concerning the plume inflow position over time, model PlumePosVar9 features a plume that arrives below the reconstructed position of the Deccan Traps, reproduces the observed topography of the hotspot track and reaches the base of the lithosphere below La Réunion Island at present day. While this means that the plume motion model seems to agree well with observations, there is still no melt generated at the position of the Deccan Traps and La Réunion, which is discussed in more detail in section 2.4.1.

The most important finding, however, is that the gap between the Maldives and Chagos as well as the Rodrigues Ridge are clearly reproduced more or less distinct in all the varied model setups despite the parameter modifications. The origins of these features are therefore described in more detail in the following two sections.

2.3.4 Formation of the Gap in the Hotspot Track

The gap interrupting the typically continuous hotspot track between the Maldives and the Chagos Bank was formed around 50 Ma, approximately coinciding with the India-Asia collision (Patriat and Achache, 1984). In the numerical model, this tectonic event is indirectly considered by the abrupt velocity decrease of the Indian plate at 50 Ma (note the velocity difference between Figures 2.2b and 2.2c or Figures 2.5a and 2.5b, respectively). However, since the direction of the Indian plate motion hardly changes, this has only a minor effect on the creation of the gap, which is illustrated in Figure 2.5 (see supporting information Movie 2.S1 for an animated view).

The ridge geometry (illustrated by the red line) appears as a series of steps, reflecting the distribution of transform faults at the Central Indian Ridge. While decompression melting occurs along the ridge axis, almost no melt is generated along the transform faults. At 52 Ma (Figure 2.5a), the hot rising plume material is in the vicinity of the ridge axis, coinciding with the place of origin of the Laccadives and Maldives (dashed yellow line). Over time, the ridge moves northeastward and the plume surface position migrates accordingly southward along the ridge, jumping from one ridge segment to another and as long as the transform faults are sufficiently small, this process results in continuous island chains on the Indian plate. But at 47 Ma (Figure 2.5b), the plume is located underneath a particularly long transform fault that disrupts the melt generation and thus creates a gap until the plume reaches the next ridge segment around 44 Ma. At this time melting starts again and the Chagos archipelago is formed (second dashed yellow line in Figure 2.5c). While the position of the gap fits observations very well, the timing is slightly shifted: age estimations at the northern end of the Chagos Bank

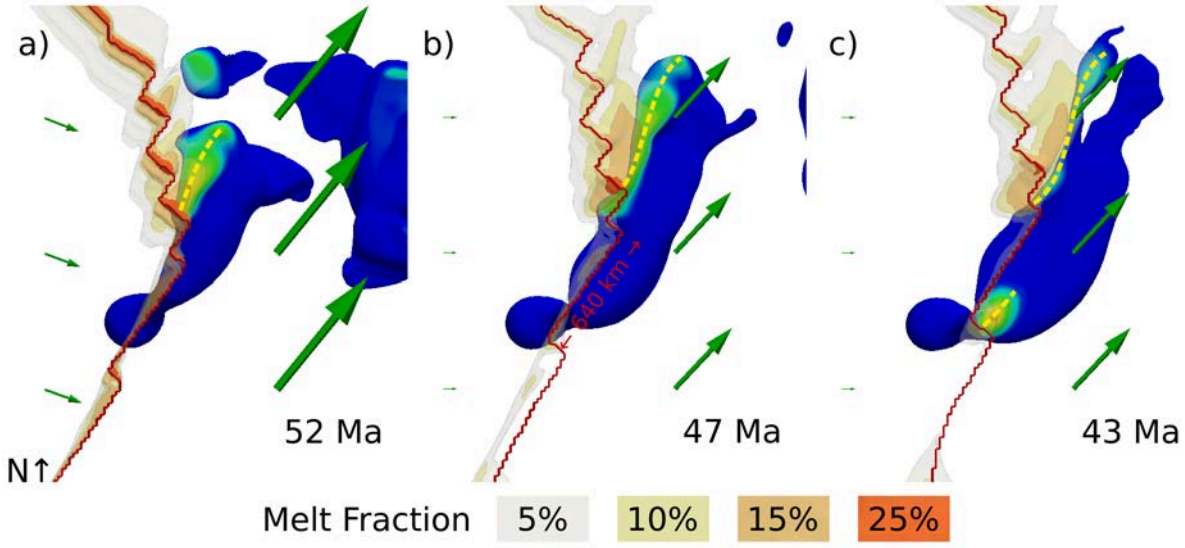

Figure 2.5: Top view of the plume (colored as in Figure 2.2) illustrating the formation of the gap in the hotspot track. Green arrows depict the velocities of the African and Indian plate and the isosurfaces along the Central Indian Ridge (red line) show total melt fractions above 5% in the entire model domain. The dashed yellow lines represent the zones where the Laccadives and Maldives are created, followed by the Chagos archipelago after the gap.

yielded 49.3 Myr ± 0.6 Myr (Duncan and Hargraves, 1990) instead of 44 Myr observed in the model, a difference that could be easily explained by a slightly shifted plume position.

In conclusion, the gap in the model originates from a combination of the ridge geometry, in particular the distribution of transform faults, plate motions and plume-ridge interaction. This result differs significantly from previous studies that investigated similar phenomena and explained the gaps between off-ridge and on-ridge hotspot tracks by plume material being ponded by membrane compression (Sleep, 2002) or attributed the formation of discrete islands within a hotspot track to shear instabilities of the involved mantle plume (Skilbeck and Whitehead, 1978; Ihinger, 1995), solitary waves in the plume (Schubert et al., 1989) or the interaction of rising magma and lithospheric flexure (Hieronymus and Bercovici, 1999).

2.3.5 Origin of the Rodrigues Ridge

The Rodrigues Ridge is a narrow volcanic lineament that was formed between 10 and 7 Ma (Dyment et al., 2007) and seems to connect the younger end of the Réunion hotspot track with the closest part of the Central Indian Ridge, which is located more than 1000 km east of Réunion Island. The pronounced west-east trend of the Rodrigues Ridge deviates from the northeastward motion of the African plate and the regular hotspot track along the Mascarene Plateau. Despite the great distance, the Rodrigues Ridge seems to be evidence of plume-ridge interaction as indicated by the geochemical anomaly around 20°S at the Central Indian Ridge (Mahoney et al., 1989; Schilling, 1991; Nauret et al., 2006; Füri et al., 2011). The first qualitative interpretation of this unusual feature was given by Morgan (1978), who explained the long-distance plume-

ridge interaction by an asthenospheric channel in which plume material is flowing toward the ridge.

All crustal thickness maps predicted by the model variations (Figure 2.4 and supporting information Figure 2.S3) show a distinctive, although slightly rotated crustal lineament at the position of the Rodrigues Ridge. Supporting information Movie 2.S1 reveals that its origin is strongly dependent on the ridge geometry, similar to the formation of the gap between the Maldives and the Chagos Bank in the hotspot track (see section 2.3.4). A major feature in ridge geometry in this region is the Marie Celeste Fracture Zone (Figure 2.1), a transform fault where no decompression melting occurs over the last 20 Myr in the model. During this time, the plume material approaches the surface southwest of the fracture zone and then flows toward the closest part of the ridge, in this case the corner between the Marie Celeste Fracture Zone and the adjacent ridge segment. Hence, over an extended period of time, melt is always produced at the southwestern end of the fracture zone, and the generated crust forms a lineament parallel to it. It appears like a prolongation of the Marie Celeste Fracture Zone and thus resembles a slightly rotated Rodrigues Ridge.

Figure 2.6a shows the present-day state of the plume in a cross section of model PlumePosVar9, where the plume reaches the lithosphere-asthenosphere boundary underneath La Réunion (see white dashed line). The combined effects of the plate motions, the global flow, upside-down drainage, and negative dynamic pressures generated by the plate motions at the ridge direct the uprising plume material toward regions of thinner lithosphere at the Central Indian Ridge. In spite of the long distance, the plume reaches the ridge axis where the lithosphere is thin enough to initiate melting in an area extending as far as the Rodrigues Ridge. This explicitly supports the existing hypothesis of continuous long-distance plume-ridge interaction and the existence of a sublithospheric flow channel (Morgan, 1978). The same also applies for the almost vertical plume in model NoGlobalFlow (Figure 2.6b), where the plume material still flows toward the ridge and melting occurs almost exclusively underneath the African plate.

2.4 Discussion

2.4.1 Melt Generation at the Deccan Traps and Réunion Island

The main focus of this study is the interaction of the Réunion plume with the Central Indian Ridge, and the presented models plausibly explain the development of the gap in the hotspot track between the Maldives and the Chagos Bank and the creation of the Rodrigues Ridge. However, crustal production below the lithosphere further away from the ridge is not captured as well. In particular, both the beginning and the end of the modeled hotspot track deviate from observations: no melt is generated on the Indian continent – at the reconstructed position of the Deccan Traps – and the present-day plume does not produce any melt close to La Réunion or Mauritius. In both cases, the plume in model PlumePosVar9 reaches the base of the lithosphere at the position expected from observations (below India and Réunion Island, respectively), but does not melt because of the high lithospheric thickness (>200 km for India, 125 km for

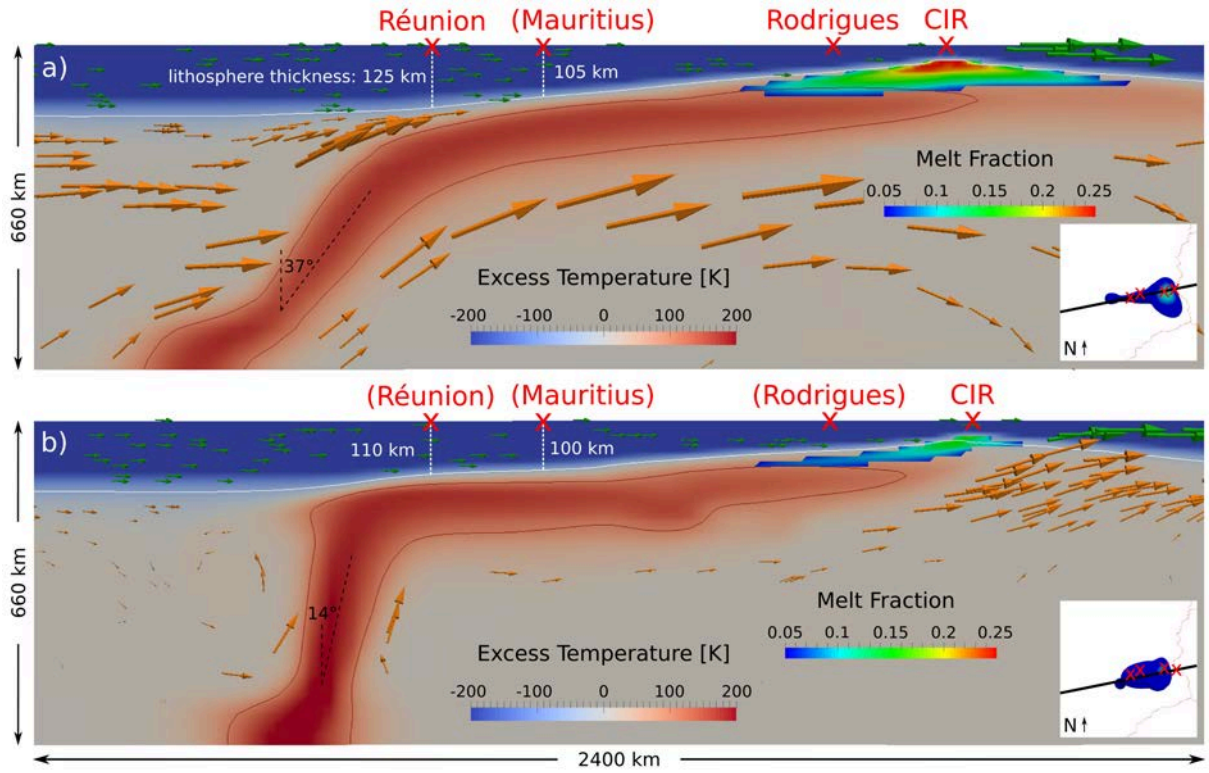

Figure 2.6: Cross sections of the present-day state showing the sublithospheric flow channel from the Réunion plume along the Rodrigues Ridge toward the Central Indian Ridge (CIR) in (a) model PlumePosVar9 and (b) model NoGlobalFlow, slightly shifted to the south to cut through the plume conduit. Colors show the excess temperature relative to the adiabat and the area exceeding 5% melt fraction, respectively. The dark red contour outlines the plume and the white contour the base of the lithosphere. Orange arrows depict the global flow, green arrows the plate motions. The inset map shows the position of the cross section in a top view of the model.

La Réunion, and 105 km for Mauritius; see Figure 2.6a). Instead, hot plume material flows toward regions of thinner lithosphere, where melt is generated due to decompression.

There are a number of potential explanations for this behavior. First, the models potentially overestimate the lithospheric thickness, and employing a model that predicts thinner lithosphere could lead to a more realistic melt production away from the ridge (as demonstrated by the correctly located Deccan Traps in model HomLith, Figure 2.4d). In the case of India, the continental lithosphere might have been thinner before the plume impingement, and some of the thick lithosphere visible in seismic models today may have been generated during and after the massive melting event of the plume through dehydration stiffening. For Mauritius and La Réunion, lithospheric thickness is not generated self-consistently in the model, because it was created outside the model domain. Instead, the thermal structure is prescribed as a boundary condition based on lithospheric age models (see section 2.2.2). Plate-cooling models such as GDH1 (Stein and Stein, 1992) predict thinner lithosphere for a given lithospheric age than the half-space cooling model utilized in this study and could therefore possibly facilitate melting at La Réunion Island. Much thinner lithosphere has also been suggested by a recent receiver

function study (Fontaine et al., 2015), which estimated 70 km thick lithosphere beneath La Réunion and 50 km thick lithosphere underneath Mauritius – values small enough to enable melting underneath these islands and thus yield a more realistic present-day crustal distribution as a model result.

Second, the modeled plume does neither contain enriched components like eclogite, which would lead to melting at higher pressures (Sobolev et al., 2007; Sobolev et al., 2011), nor volatiles, known to decrease the solidus of mantle rocks (e.g., Katz et al., 2003). For the case of La Réunion, a plume with an excess temperature of 200 K containing recycled crust would already start to melt at 180 km depth (Sobolev et al., 2011), whereas the modeled purely thermal (peridotitic) plume only starts to melt at 115 km depth, closer to the ridge (see Figure 2.6). In the case of the Deccan Traps, as soon as melting occurs, the amount of melt could be tremendously increased by thermomagmatic erosion of the lithosphere (Sobolev et al., 2011), a mechanism that is related to the transport and reaction of generated melt, and is not included in the models. Other disregarded processes such as dislocation creep could also lead to mechanical thinning of the lithosphere above the plume, thus increasing melt production.

By optimizing the lithospheric thickness used as initial and boundary conditions and the composition of the plume, the geodynamic model could presumably be tuned to also reproduce the magmatic crust generated at Réunion Island and the Deccan Traps. However, as the focus is on plume-ridge interaction, this is outside the scope of the present study.

It has recently been proposed by Glišović and Forte (2017) – who reconstruct large-scale plume and mantle structures in the past based on present-day seismic tomography in contrast to the forward modeling approach and much higher resolved plume in this study (due to a considerably smaller model domain and the adaptive mesh refinement) – that the northern part of the Deccan Traps was generated by an additional unrecognized plume underneath the Comoros. Since this study is not designed to handle melting in continental environments, a second plume beneath India around 65 Ma would likely result in additional flow toward thinner oceanic lithosphere (regardless of a correct plume timing and position as discussed above). However, the model evolution does not indicate a need for a second plume to accurately shape the Réunion hotspot track.

2.4.2 Crustal Thickness Values

The overall crustal thickness contribution of the plume predicted by the models is approximately in the same range as what is inferred from observations, in particular in comparison to models of plume-ridge interaction without dehydration rheology where the crust generated by the plume exceeds 100 km (supporting information Figure 2.S3g or models in Gassmöller et al. (2016)). A plume with an excess temperature of 200 K (model DeltaT200) produces up to 40 km of magmatic crust (see Figure 2.4b), which is comparable to the crustal thickness map of Torsvik et al. (2013) that features maximum values of about 35 km at the Maldives, the Chagos Bank, and the Mascarene Plateau.

Nevertheless, the model predictions still exceed the expected values, especially when taking

into account that the crust produced at the mid-ocean ridges (which is not included in Figure 2.4) contributes additionally to the absolute values, and that Torsvik et al. (2013) attribute the thick crust partly to underlying continental fragments.

More detailed comparisons of model DeltaT200 with results from previous studies in the region of the hotspot track also indicate that the model results are at the upper end of the range of expected values. For the Laccadives, the inversion of teleseismic receiver functions of Gupta et al. (2010) reported an oceanic crust of 16 km thickness underplated by an 8 km thick high-velocity layer, while the modeled plume produces about 25 km excess crustal thickness. For the Maldives, the receiver function study of Fontaine et al. (2015) estimated 6 – 7 km crust and a 14 – 11 km thick underplated layer, whereas the modeled plume generates up to 40 km excess crustal thickness. From bathymetry and gravity data, Henstock and Thompson (2004) modeled mean crustal thicknesses of 12 – 27 km for the Chagos-Laccadive ridge. Fontaine et al. (2015) suggested 8 km crust and a 5 km thick underplated layer underneath Chagos; the plume in the model produces excess crustal thickness of up to 35 km. On the African plate, Fontaine et al. (2015) identified 10 km crust and a 7 km thick underplated layer underneath Mauritius, 6 km crust and a 2 km thick underplated layer underneath La Réunion and 6 km crust beneath Rodrigues. Along the Rodrigues Ridge, the modeled plume yields up to 30 km excess crustal thickness. In summary, the published estimates indicate that the excess temperature of the plume is most likely at the lower end of values tested in this study (i.e., model DeltaT200).

A potential explanation for the higher values in the computation is the fact that the used melting model (Katz et al., 2003) is an equilibrium batch melting model (as opposed to a fractional melting model). While it considers the decrease in melt productivity with increasing depletion, this effect would be even stronger in case of fractional melting, due to the associated changes in composition. As incremental batch melting – presumably occurring in a mantle plume – has a productivity somewhere between batch melting and fractional melting, the models overestimate the amount of generated crust.

Moreover, the melt extraction method applied in this study considers the entirety of plume induced melt to ascend through the lithosphere and create crustal material – whereas melt close to a mid-ocean ridge is expected to migrate toward the ridge instead of rising vertically (Braun and Sohn, 2003). The neglect of possible lateral melt transport could therefore also provide an explanation for the high amounts of crust produced by the modeled plume.

2.4.3 Global Flow and Present-day State of the Plume

At the present-day state of the model, the plume is highly tilted (by approximately 37°) and most of the plume material is drawn eastward, in the direction of the Central Indian Ridge. If the plume inflow position is manually moved further away from the ridge as in model PlumePosVar5, the tilt is even more pronounced (approximately 39°). Comparing the reference model or model PlumePosVar9 with the tilt of 14° in model NoGlobalFlow (Figures 2.6a and 2.6b, respectively, or supporting information Movie 2.S1) provides evidence that the main factor which deflects the plume from its vertical ascent is the global flow prescribed as boundary conditions.

In the global mantle convection model from which the boundary input files are derived, the global flow at the latitude of the Réunion plume at recent times is vastly influenced by the fast ascent of hot material above the African LLSVP. The main direction of the global flow is therefore eastward, relatively fast and almost unaffected by the (relatively slow) northeastward plate motions above. This provides an explanation why the plume in the reference model is deflected more to the east than to the northeast and consequently produces melt too far south along the Central Indian Ridge, whereas the plume-ridge interaction in model NoGlobalFlow matches the region of the plume-related geochemical anomaly between 12°S and 22°S along the ridge (Schilling, 1991) (Figures 2.4a and 2.4e, respectively). The direction of the modeled plume tilt is consistent with the plume tilt in the global model from which the global flow is derived – between east-northeastward and northeastward at present.

One possible explanation for this major role of the global flow in the model, and that it deflects plume material to a part of the ridge where no geochemical anomaly or excess crustal thickness is observed, could be that large-scale mantle circulation is in fact more sluggish than prescribed in the model, a view recently championed by Kevin Burke (Torsvik et al., 2016). Considering that the much more vertical plume tail in model NoGlobalFlow produces a crustal thickness pattern that fits the topography of the southern part of the hotspot track well – especially the Mascarene Plateau and the region along the Central Indian Ridge up to the Rodrigues Triple Junction (Figure 2.4e) – an optimized model of global mantle flow would likely feature slower movements and a flow direction slightly rotated to the northeast in accordance with the plate motions.

To compare the geodynamic model results to seismological tomographic models or shear-wave splitting observations, the present-day state of the model is essential. Figure 2.6 shows two feasible model predictions for the current state of the plume, reaching the base of the lithosphere under Réunion Island (even though no melt is generated there, as discussed above). Consistent with the northeastward large-scale plate motion and the eastward global flow – and the idea of an Indian Ocean "conveyor belt" (Becker and Faccenna, 2011) – the plume approaches La Réunion from west-southwest, the direction of the LLSVP at the core-mantle boundary. In contrast to a recent seismic anisotropy analysis beneath islands on or close to the hotspot track, which suggested the plume conduit to be located 100 – 200 km north of La Réunion Island (Barruol and Fontaine, 2013), the plume in the models presented in this study arrives below the lithosphere close to La Réunion as in previous models (Steinberger, 2000; Steinberger and Antretter, 2006; Boschi et al., 2007; Steinberger and Torsvik, 2012) and consistent with global seismological studies by Montelli et al. (2006) and model SMEAN2 (see supporting information Figure 2.S4 for a cross section of the Réunion plume). More insights on the present-day state and particularly the tilt of the plume are to be expected from the seismological results of the RHUM-RUM project.

2.5 Conclusions and Outlook

The motivation for this study was to investigate the interaction between the Réunion plume and the Central Indian Ridge, and how it shaped the crustal thickness pattern of the Réunion hotspot track. Comparing the model results to the observed topographic expression of the hotspot track, the following conclusions can be drawn:

The continuous ocean-island chains of the Laccadives and Maldives fit into the widely accepted concept of an age-progressive hotspot track. The subsequent gap in the hotspot track between the Maldives and the Chagos Bank does not contradict this interpretation. Rather it is a direct consequence of the interaction between the Central Indian Ridge and the Réunion plume, which at this time moved along a particularly long ridge transform fault, thus creating a pause in volcanic activity. Only after the ridge traveled far enough for the plume to arrive close to the next ridge segment, the Chagos Bank was generated. This conclusion holds true for all variations of model parameters in this study.

After the Central Indian Ridge overrode the plume, the edge between the Marie Celeste Fracture Zone and the adjacent ridge segment acted as a focal point to which a part of the plume material was dragged and where thinner lithosphere enabled melting and the creation of the Rodrigues Ridge. This provides computational support for the theory of Morgan (1978), showing that plume-ridge interaction is possible up to distances on the order of 1000 km. Altogether, the models illustrate how small-scale surface features originate from the complex interaction between processes in the mantle and the lithosphere.

As discussed above, to capture the full plume evolution from the Large Igneous Province to the melt generation beneath La Réunion today, a number of additional complexities will need to be considered. In particular, a more complex melt generation model that includes enriched source components in the plume, and the potential for thermomagmatic erosion is required to accurately model the generation of a Large Igneous Province on thick continental lithosphere. Additionally, to resolve the generation of volcanic chains as narrow features (like the Rodrigues Ridge) as opposed to broad zones of magmatic crust, a plastic material rheology coupled to a melt migration model might proof crucial to achieve the necessary focusing of melt.

At the present-day state, the modeled plume arrives approximately below La Réunion Island and features a strong eastward tilt in the upper mantle, even though the plates are moving northeastward. The models suggest that this tilt is mainly caused by the eastward surrounding flow field. Although the speed of global mantle flow is debated (as discussed above), comparisons between the model results, in particular the degree of plume tilting, and future high-resolution seismic studies within the RHUM-RUM project will therefore allow to estimate the actual speed of upper mantle flow below the Indian Ocean.

Acknowledgments

The geodynamic models were computed with the open-source software ASPECT (http://aspect.dealii.org) and the necessary data to reproduce the models is included in the supporting information. The constructive comments of two anonymous reviewers have been appreciated. This project is funded by the Deutsche Forschungsgemeinschaft (DFG) under grant STE 907/11-1 to B.S. as part of the RHUM-RUM project (Réunion Hotspot and Upper Mantle – Réunions Unterer Mantel). The computational resources were provided by the North-German Supercomputing Alliance (HLRN) as part of project bbp00006: "Numerical geodynamic modeling of a mantle plume under La Réunion and its interaction with large-scale 3D mantle flow". J.D. and R.G. were partially supported by the Computational Infrastructure for Geodynamics initiative (CIG), through the National Science Foundation under Awards EAR-0949446 and EAR-1550901, administered by The University of California-Davis, and the National Science Foundation under award OCI-1148116 as part of the Software Infrastructure for Sustained Innovation (SI2) program.

2.6 Supporting Information

Supplementary Movie 2.S1 and Data Set 2.S1 can be found online at http://dx.doi.org/10.1002/2017GC006875 (freely available from August 2019) or on the enclosed CD.

2.6.1 Movie 2.S1

Development of the reference model (top row) and model NoGlobalFlow (bottom row) over the past 80 Myr.

(left) Plume and plume-ridge interaction over time, corresponding to Figure 2.2. The plume is colored according to the melt fraction. Mid-ocean ridges are marked as red lines and the plate velocities are depicted by green arrows, all on the same scale.

(center) Lithospheric thickness evolution and plume-ridge interaction over time, corresponding to Figure 2.3. The plume is colored according to the melt fraction, mid-ocean ridges are marked as red lines and the base of the lithosphere is color-coded according to the depth.

(right) Top view of the model, corresponding to Figure 2.5. The plume is colored according to the melt fraction. Green arrows depict the equally scaled velocities of the plates and the isosurfaces show total melt fractions above 5% (gray), 10% (yellow), 15% (light orange) and 25% (dark orange).

2.6.2 Data Set 2.S1

The numerical models of this study were created with an extended version of the mantle convection code ASPECT. The used source code is available online at: https://github.com/ebredow/aspect/tree/reunion_plume_model.

The data files used as boundary conditions for the plate motions, the global flow and the plume inflow positions can be found in Data Set 2.S1. For detailed descriptions see the supplementary information in Gassmöller et al. (2016), in the captions of Data Set S2 – S5.

2.6.3 Figures 2.S1 to 2.S4

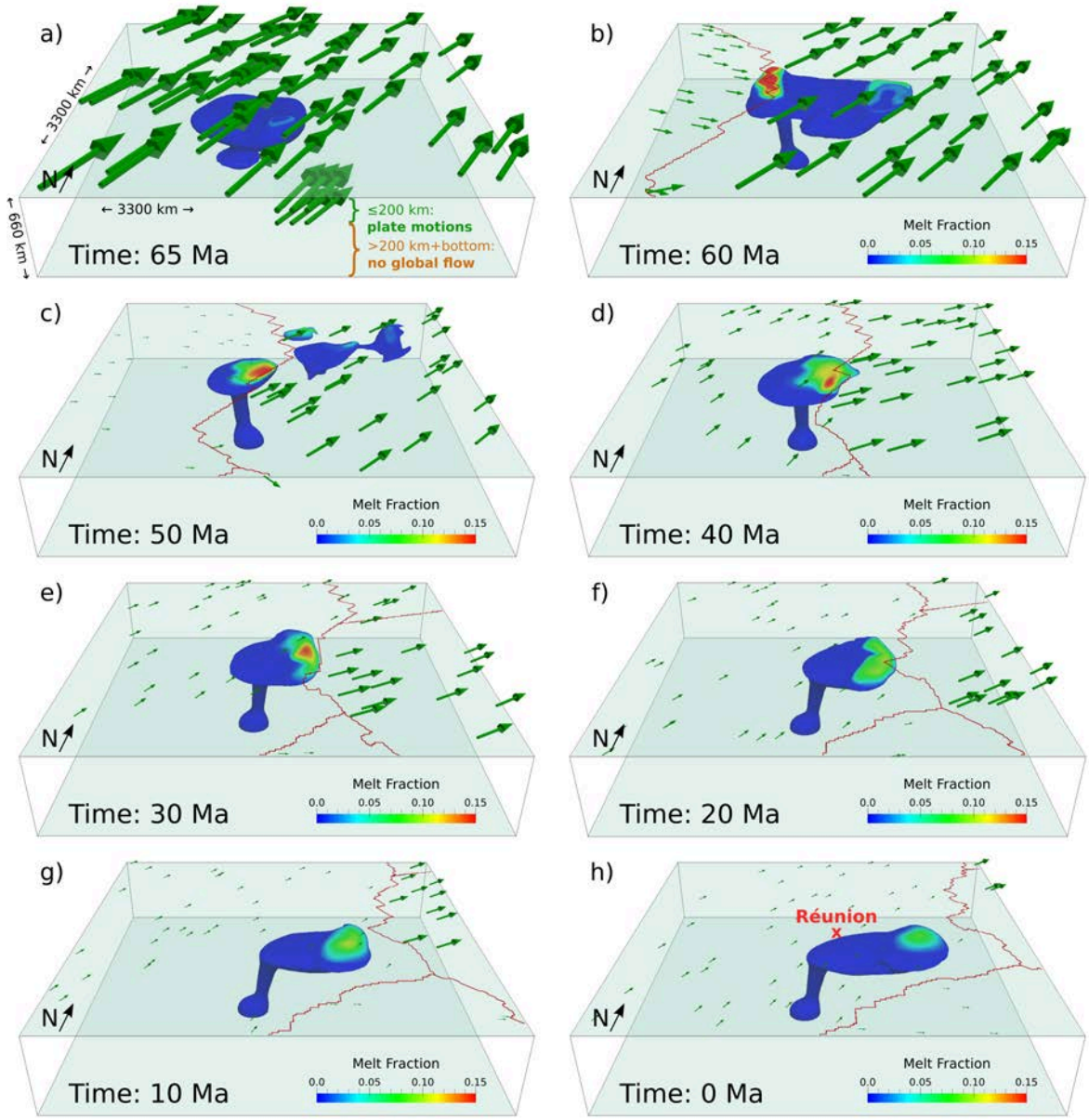

Figure 2.S1: Development of model NoGlobalFlow: plume and plume-ridge interaction over time. The plume is represented by the $\Delta T = 100\,\mathrm{K}$ isosurface and colored according to the melt fraction. Mid-ocean ridges are marked as red lines, the plate velocities are depicted by green arrows. (a) Additionally illustrates the velocity side boundary conditions. (h) Represents the present-day state and shows the position of Réunion Island.

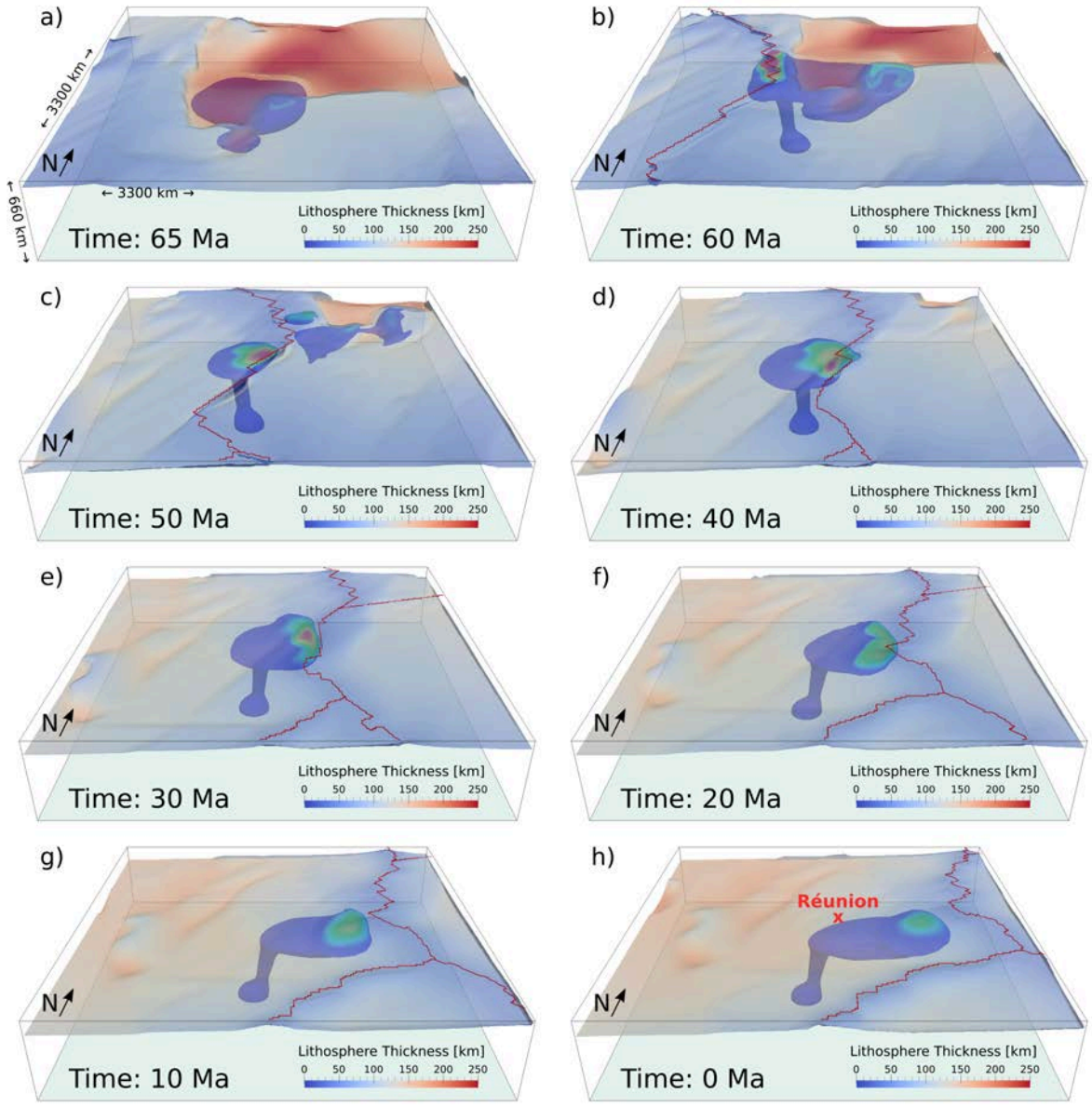

Figure 2.S2: Development of model NoGlobalFlow: lithospheric thickness evolution and plume-ridge interaction over time. The plume is colored according to the melt fraction (as in Figure 2.S1), mid-ocean ridges are marked as red lines and the base of the lithosphere is color-coded according to the depth. (h) Represents the present-day state and shows the position of Réunion Island.

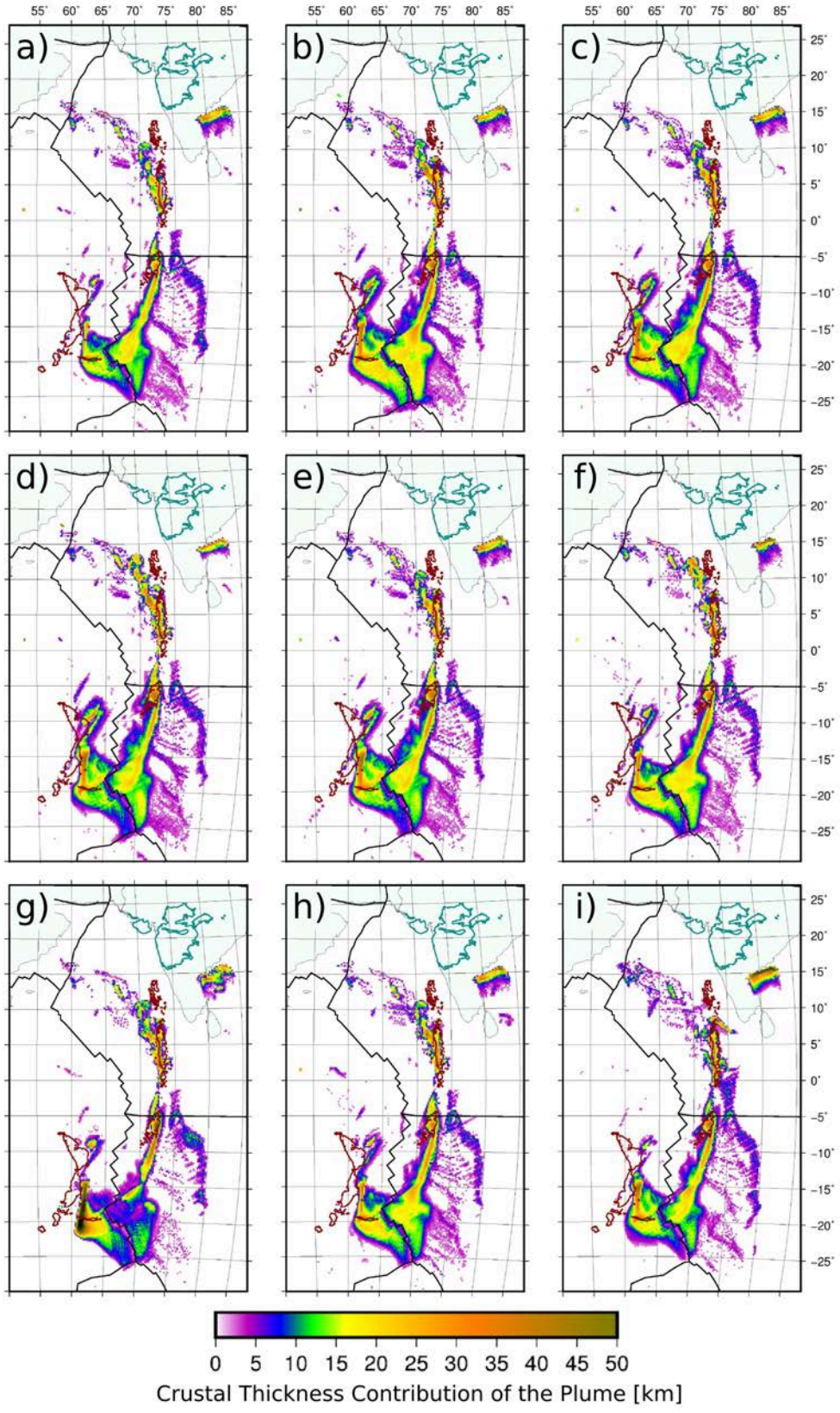

Figure 2.S3: Present-day model state: crustal thickness pattern solely produced by the plume in various models in addition to Figure 2.4. (a) Flux950, (b) Flux1900, (c) FixedPlume, (d) PlumePosVar5, (e) PlumePosVar9, (f) LithThickNew, (g) NoDehyd, (h) NoDepl, and (i) DefaultVisc. The dark red outlines show the observed hotspot track, represented by the -1500 m topography contours.

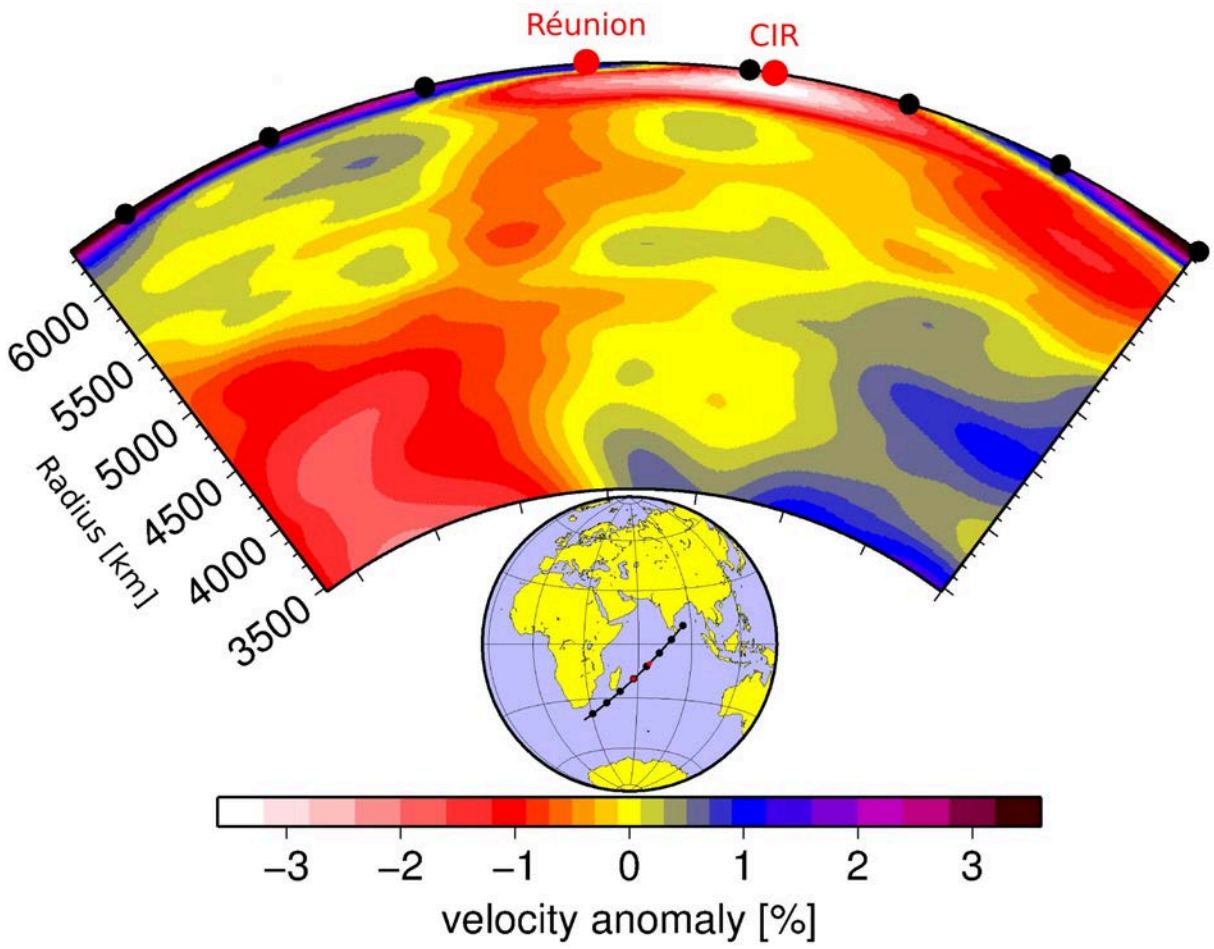

Figure 2.S4: Cross section of model SMEAN2, showing the Réunion plume rising from the edge of the African LLSVP and approaching La Réunion from southwest – in agreement with the model results in this study. SMEAN2 is a global, composite mantle tomography model constructed from models S40RTS (Ritsema et al., 2011), GyPSUM-S (Simmons et al., 2010) and SAVANI (Auer et al., 2014) following the approach Becker and Boschi (2002) used for SMEAN. Black dots along the cross section indicate increments of 10°. Note also the distinct long-distance plume-ridge interaction which agrees well with the present-day state of the plume in the models presented in this study (for comparison, see Figure 2.6 in the main text).

References

Ashwal, L. D., M. Wiedenbeck, and T. H. Torsvik (2017), Archaean zircons in Miocene oceanic hotspot rocks establish ancient continental crust beneath Mauritius, *Nat. Commun.*, 8, 14,086, doi: 10.1038/ncomms14086.

Auer, L., L. Boschi, T. W. Becker, T. Nissen-Meyer, and D. Giardini (2014), Savani: A variable resolution whole-mantle model of anisotropic shear velocity variations based on multiple data sets, *J. Geophys. Res.*, 119, 3006–3034, doi: 10.1002/2013JB010773.

Bangerth, W., J. Dannberg, R. Gassmöller, T. Heister, et al. (2017), *ASPECT: Advanced Solver for Problems in Earth's ConvecTion*. Comput. Infrastruct. for Geodyn., Davis, Calif.

Barruol, G. and F. R. Fontaine (2013), Mantle flow beneath la Réunion hotspot track from SKS splitting, *Earth Planet. Sci. Lett.*, 362, 108–121, doi: 10.1016/j.epsl.2012.11.017.

Barruol, G. and K. Sigloch (2013), Investigating La Réunion hot spot from crust to core, *Eos Trans. AGU*, 94(23), 205–207, doi: 10.1002/2013EO230002.

Becker, T. W. and L. Boschi (2002), A comparison of tomographic and geodynamic mantle models, *Geochem. Geophys. Geosyst.*, 3, 1003, doi: 10.1029/2001GC000168.

Becker, T. W. and C. Faccenna (2011), Mantle conveyor beneath the Tethyan collisional belt, *Earth Planet. Sci. Lett.*, 310(3-4), 453–461, doi: 10.1016/j.epsl.2011.08.021.

Boschi, L., T. W. Becker, and B. Steinberger (2007), Mantle plumes: Dynamic models and seismic images, *Geochem. Geophys. Geosyst.*, 8, Q10006, doi: 10.1029/2007GC001733.

Braun, M. G. and R. A. Sohn (2003), Melt migration in plume–ridge systems, *Earth Planet. Sci. Lett.*, 213(3-4), 417–430, doi: 10.1016/S0012-821X(03)00279-6.

Burke, K., B. Steinberger, T. H. Torsvik, and M. A. Smethurst (2008), Plume Generation Zones at the margins of Large Low Shear Velocity Provinces on the core-mantle boundary, *Earth Planet. Sci. Lett.*, 265(1-2), 49–60, doi: 10.1016/j.epsl.2007.09.042.

Cande, S. C. and D. R. Stegman (2011), Indian and African plate motions driven by the push force of the Reunion plume head, *Nature*, 475(7354), 47–52, doi: 10.1038/nature10174.

Charvis, P., A. Laesanpura, J. Gallart, A. Hirn, J.-C. Lépine, B. de Voogd, T. A. Minshull, Y. Hello, and B. Pontoise (1999), Spatial distribution of hotspot material added to the lithosphere under la Réunion, from wide-angle seismic data, *J. Geophys. Res.*, 104(B2), 2875–2893, doi: 10.1029/98JB02841.

Christensen, U. (1983), Convection in a variable-viscosity fluid: Newtonian versus power-law rheology, *Earth Planet. Sci. Lett.*, 64(1), 153–162, doi: 10.1016/0012-821X(83)90060-2.

Courtillot, V. E. and P. R. Renne (2003), On the ages of flood basalt events, *C. R. Geosci.*, 335(1), 113–140, doi: 10.1016/S1631-0713(03)00006-3.

Courtillot, V., J. Besse, D. Vandamme, R. Montigny, J.-J. Jaeger, and H. Cappetta (1986), Deccan flood basalts at the Cretaceous/Tertiary boundary?, *Earth Planet. Sci. Lett.*, 80(3), 361–374, doi: 10.1016/0012-821X(86)90118-4.

Courtillot, V., G. Féraud, H. Maluski, D. Vandamme, M. G. Moreau, and J. Besse (1988), Deccan flood basalts and the Cretaceous/Tertiary boundary, *Nature*, 333(6176), 843–846, doi: 10.1038/333843a0.

Courtillot, V., A. Davaille, J. Besse, and J. Stock (2003), Three distinct types of hotspots in the Earth's mantle, *Earth Planet. Sci. Lett.*, 205(3-4), 295–308, doi: 10.1016/S0012-821X(02)01048-8.

Crough, S. T. (1983), Hotspot swells, *Ann. Rev. Earth Planet. Sci.*, 11, 165–193, doi: 10.1146/annurev.ea.11.050183.001121.

Davies, G. F. (1988), Ocean bathymetry and mantle convection: 1. Large-scale flow and hotspots, *J. Geophys. Res.*, 93, (B9), 104,67–10,480, doi: 10.1029/JB093iB09p10467.

Doubrovine, P. V., B. Steinberger, and T. H. Torsvik (2012), Absolute plate motions in a reference frame defined by moving hot spots in the Pacific, Atlantic, and Indian oceans, *J. Geophys. Res.*, 117, B09101, doi: 10.1029/2011JB009072.

Duncan, R. (1990), The volcanic record of the Réunion hotspot, *Proc. Ocean Drill. Program Sci. Results*, 115, 3–10, doi: 10.2973/odp.proc.sr.115.206.1990.

Duncan, R. and R. Hargraves (1990), $^{40}Ar/^{39}Ar$ geochronology of basement rocks from the Mascarene Plateau, the Chagos Bank, and the Maldives Ridge, *Proc. Ocean Drill. Program Sci. Results*, 115, 43–51, doi: 10.2973/odp.proc.sr.115.141.1990.

Duncan, R. A. and M. A. Richards (1991), Hotspots, mantle plumes, flood basalts, and true polar wander, *Rev. Geophys.*, 29(1), 31–50, doi: 10.1029/90RG02372.

Dupeyrat, L., C. Sotin, and E. M. Parmentier (1995), Thermal and chemical convection in planetary mantles, *J. Geophys. Res.*, 100(B1), 497–520, doi: 10.1029/94JB01189.

Dyment, J., J. Lin, and E. Baker (2007), Ridge-hotspot interactions : What mid-ocean ridges tell us about deep Earth processes, *Oceanography*, 20, 102–115, doi: 10.5670/oceanog.2007.84.

Farley, K. and E. Neroda (1998), Noble gases in the Earth's mantle, *Annu. Rev. Earth Planet. Sci.*, 26, 189–218, doi: 10.1146/annurev.earth.26.1.189.

Fontaine, F. R., G. Barruol, H. Tkalčić, I. Wölbern, G. Rümpker, T. Bodin, and M. Haugmard (2015), Crustal and uppermost mantle structure variation beneath la Réunion hotspot track, *Geophys. J. Int.*, 203(1), 107–126, doi: 10.1093/gji/ggv279.

French, S. W. and B. Romanowicz (2015), Broad plumes rooted at the base of the Earth's mantle beneath major hotspots, *Nature*, 525, 95–99, doi: 10.1038/nature14876.

Füri, E., D. R. Hilton, B. J. Murton, C. Hémond, J. Dyment, and J. M. D. Day (2011), Helium isotope variations between Réunion island and the Central Indian Ridge (17°–21°S): New evidence for ridge-hot spot interaction, *J. Geophys. Res.*, 116, B02207, doi: 10.1029/2010JB007609.

Gallart, J., L. Driad, P. Charvis, M. Sapin, A. Hirn, J. Diaz, B. de Voogd, and M. Sachpazi (1999), Perturbation to the lithosphere along the hotspot track of la Réunion from an offshore-onshore seismic transect, *J. Geophys. Res.*, 104(B2), 2895–2908, doi: 10.1029/98JB02840.

Garnero, E. J., T. Lay, and A. McNamara (2007), Implications of lower-mantle structural heterogeneity for the existence and nature of whole-mantle plumes, *Spec. Pap. Geol. Soc. Am.*, 430, 79–101, doi: 10.1130/2007.2430(05).

Gassmöller, R., J. Dannberg, E. Bredow, B. Steinberger, and T. H. Torsvik (2016), Major influence of plume-ridge interaction, lithosphere thickness variations, and global mantle flow on hotspot volcanism – The example of Tristan, *Geochem. Geophys. Geosyst.*, 17, 1454–1479, doi: 10.1002/2015GC006177.

Glišović, P. and A. M. Forte (2017), On the deep-mantle origin of the Deccan Traps, *Science*, 355(6325), 613–616, doi: 10.1126/science.aah4390.

Gupta, S., S. Mishra, and S. S. Rai (2010), Magmatic underplating of crust beneath the Laccadive Island, NW Indian Ocean, *Geophys. J. Int.*, 183(2), 536–542, doi: 10.1111/j.1365-246X.2010.04759.x.

Henstock, T. J. and P. J. Thompson (2004), Self-consistent modeling of crustal thickness at Chagos–Laccadive ridge from bathymetry and gravity data, *Earth Planet. Sci. Lett.*, 224(3-4), 325–336, doi: 10.1016/j.epsl.2004.05.021.

Herzberg, C. and E. Gazel (2009), Petrological evidence for secular cooling in mantle plumes, *Nature*, 458, 619–622, doi: 10.1038/nature07857.

Hieronymus, C. F. and D. Bercovici (1999), Discrete alternating hotspot islands formed by interaction of magma transport and lithospheric flexure, *Nature*, 397(6720), 604–607, doi: 10.1038/17584.

Hirth, G. and D. Kohlstedt (2003), Rheology of the upper mantle and the mantle wedge: A view from the experimentalists, in *Inside the Subduction Factory*, edited by J. Eiler, pp. 83–105, AGU, Washington, D. C., doi: 10.1029/138GM06.

Hofmann, C., G. Féraud, and V. Courtillot (2000), $^{40}Ar/^{39}Ar$ dating of mineral separates and whole rocks from the Western Ghats lava pile: Further constraints on duration and age of the Deccan traps, *Earth Planet. Sci. Lett.*, 180(1-2), 13–27, doi: 10.1016/S0012-821X(00)00159-X.

Howell, S. M., G. Ito, A. J. Breivik, A. Rai, R. Mjelde, B. Hanan, K. Sayit, and P. Vogt (2014), The origin of the asymmetry in the Iceland hotspot along the Mid-Atlantic Ridge from continental breakup to present-day, *Earth Planet. Sci. Lett.*, 392, 143–153, doi: 10.1016/j.epsl.2014.02.020.

Ihinger, P. D. (1995), Mantle flow beneath the Pacific plate: Evidence from seamount segments in the Hawaiian-Emperor chain, *Am. J. Sci.*, 295, 1035–1057, doi: 10.2475/ajs.295.9.1035.

Ito, G., Y. Shen, G. Hirth, and C. J. Wolfe (1999), Mantle flow, melting, and dehydration of the Iceland mantle plume, *Earth Planet. Sci. Lett.*, 165(1), 81–96, doi: 10.1016/S0012-821X(98)00216-7.

Jay, A. E. and M. Widdowson (2008), Stratigraphy, structure and volcanology of the SE Deccan continental flood basalt province: Implications for eruptive extent and volumes, *J. Geol. Soc.*, 165(1), 177–188, doi: 10.1144/0016-76492006-062.

Katz, R. F., M. Spiegelman, and C. H. Langmuir (2003), A new parameterization of hydrous mantle melting, *Geochem. Geophys. Geosyst.*, 4(9), 1073, doi: 10.1029/2002GC000433.

Kronbichler, M., T. Heister, and W. Bangerth (2012), High accuracy mantle convection simulation through modern numerical methods, *Geophys. J. Int.*, 191(1), 12–29, doi: 10.1111/j.1365-246X.2012.05609.x.

Mahoney, J. J., J. H. Natland, W. M. White, R. Poreda, S. H. Bloomer, R. L. Fisher, and A. N. Baxter (1989), Isotopic and geochemical provinces of the western Indian Ocean Spreading Centers, *J. Geophys. Res.*, 94(B4), 4033–4052, doi: 10.1029/JB094iB04p04033.

Manglik, A. and U. R. Christensen (1997), Effect of mantle depletion buoyancy on plume flow and melting beneath a stationary plate, *J. Geophys. Res.*, 102(B3), 5019–5028, doi: 10.1029/96JB03623.

McKenzie, D. and J. Sclater (1971), The evolution of the Indian Ocean since the Late Cretaceous, *Geophys. J. Int.*, 24(5), 437–528, doi: 10.1111/j.1365-246X.1971.tb02190.x.

Montelli, R., G. Nolet, F. A. Dahlen, G. Masters, E. R. Engdahl, and S.-H. Hung (2004), Finite-frequency tomography reveals a variety of plumes in the mantle, *Science*, 303(5656), 338–343, doi: 10.1126/science.1092485.

Montelli, R., G. Nolet, F. A. Dahlen, and G. Masters (2006), A catalogue of deep mantle plumes: New results from finite-frequency tomography, *Geochem. Geophys. Geosyst.*, 7, Q11007, doi: 10.1029/2006GC001248.

Morgan, W. J. (1971), Convection plumes in the lower mantle, *Nature*, 230, 42–43, doi: 10.1038/230042a0.

Morgan, W. J. (1978), Rodriguez, Darwin, Amsterdam, ..., A second type of Hotspot Island, *J. Geophys. Res.*, 83(B11), 5355–5360, doi: 10.1029/JB083iB11p05355.

Müller, R. D., M. Sdrolias, C. Gaina, and W. R. Roest (2008), Age, spreading rates, and spreading asymmetry of the world's ocean crust, *Geochem. Geophys. Geosyst.*, 9, Q04006, doi: 10.1029/2007GC001743.

Nauret, F., W. Abouchami, S. Galer, A. Hofmann, C. Hémond, C. Chauvel, and J. Dyment (2006), Correlated trace element-Pb isotope enrichments in Indian MORB along 18–20°S, Central Indian Ridge, *Earth Planet. Sci. Lett.*, 245(1-2), 137–152, doi: 10.1016/j.epsl.2006.03.015.

Officer, C. B., A. Hallam, C. L. Drake, and J. D. Devine (1987), Late Cretaceous and paroxysmal Cretaceous/Tertiary extinctions, *Nature*, 326(6109), 143–149, doi: 10.1038/326143a0.

Pasyanos, M. E., T. G. Masters, G. Laske, and Z. Ma (2014), LITHO1.0: An updated crust and lithospheric model of the Earth, *J. Geophys. Res. Solid Earth*, 119, 2153–2173, doi: 10.1002/2013JB010626.

Patriat, P. and J. Achache (1984), India-Eurasia collision chronology has implications for crustal shortening and driving mechanism of plates, *Nature*, 311(5987), 615–621, doi: 10.1038/311615a0.

Putirka, K. (2008), Excess temperatures at ocean islands: Implications for mantle layering and convection, *Geology*, 36(4), 283–286, doi: 10.1130/G24615A.1.

Ribe, N. M and U. R Christensen (1999), The dynamical origin of Hawaiian volcanism, *Earth Planet. Sci. Lett.*, 171(4), 517–531, doi: 10.1016/S0012-821X(99)00179-X.

Richards, M. A., R. A. Duncan, and V. E. Courtillot (1989), Flood Basalts and Hot-Spot Tracks: Plume Heads and Tails, *Science*, 246, 103–107, doi: 10.1126/science.246.4926.103.

Ritsema, J., A. Deuss, H. J. van Heijst, and J. H. Woodhouse (2011), S40RTS: a degree-40 shear-velocity model for the mantle from new Rayleigh wave dispersion, teleseismic traveltime and normal-mode splitting function measurements, *Geophys. J. Int.*, 184(3), 1223–1236, doi: 10.1111/j.1365-246X.2010.04884.x.

Schilling, J.-G. (1991), Fluxes and excess temperatures of mantle plumes inferred from their interaction with migrating mid-ocean ridges, *Nature*, 352, 397–403, doi: 10.1038/352397a0.

Schoene, B., K. M. Samperton, M. P. Eddy, G. Keller, T. Adatte, S. A. Bowring, S. F. R. Khadri, and B. Gertsch (2015), U-Pb geochronology of the Deccan Traps and relation to the end-Cretaceous mass extinction, *Science*, 347(6218), 182–184, doi: 10.1126/science.aaa0118.

Schubert, G., P. Olson, C. Anderson, and P. Goldman (1989), Solitary waves in mantle plumes, *J. Geophys. Res.*, 94(B7), 9523–9532, doi: 10.1029/JB094iB07p09523.

Simmons, N. A., A. M. Forte, L. Boschi, and S. P. Grand (2010), GyPSuM: A joint tomographic model of mantle density and seismic wave speeds, *J. Geophys. Res.*, 115, B12310, doi: 10.1029/2010JB007631.

Skilbeck, J. and J. Whitehead (1978), Formation of discrete islands in linear chains, *Nature*, 272, 499–501, doi: 10.1038/272499a0.

Sleep, N. H. (1990), Hotspots and mantle plumes: Some phenomenology, *J. Geophys. Res.*, 95(B5), 6715–6736, doi: 10.1029/JB095iB05p06715.

Sleep, N. H. (1997), Lateral flow and ponding of starting plume material, *J. Geophys. Res.*, 102(B5), 10001–10012, doi: 10.1029/97JB00551.

Sleep, N. H. (2002), Ridge-crossing mantle plumes and gaps in tracks, *Geochem. Geophys. Geosyst.*, 3(12), 8505, doi: 10.1029/2001GC000290.

Sobolev, A. V. et al. (2007), The amount of recycled crust in sources of mantle-derived melts, *Science*, 316, 412–417, doi: 10.1126/science.1138113.

Sobolev, S. V., A. V. Sobolev, D. V. Kuzmin, N. A. Krivolutskaya, A. G. Petrunin, N. T. Arndt, V. A. Radko, and Y. R. Vasiliev (2011), Linking mantle plumes, large igneous provinces and environmental catastrophes, *Nature*, 477, 312–316, doi: 10.1038/nature10385.

Stein, C. and S. Stein (1992), A model for the global variation in oceanic depth and heat flow with lithospheric age, *Nature*, 359(1), 123–129, doi: 10.1038/359123a0.

Steinberger, B. (2000), Plumes in a convecting mantle: Models and observations for individual hotspots, *J. Geophys. Res.*, 105(B5), 11,127–11,152, doi: 10.1029/1999JB900398.

Steinberger, B. (2016), Topography caused by mantle density variations: observation-based estimates and models derived from tomography and lithosphere thickness, *Geophys. J. Int.*, 205, 604–621, doi: 10.1093/gji/ggw040.

Steinberger, B. and M. Antretter (2006), Conduit diameter and buoyant rising speed of mantle plumes: Implications for the motion of hot spots and shape of plume conduits, *Geochem. Geophys. Geosyst.*, 7, Q11018, doi: 10.1029/2006GC001409.

Steinberger, B. and A. R. Calderwood (2006), Models of large-scale viscous flow in the Earth's mantle with constraints from mineral physics and surface observations, *Geophys. J. Int.*, 167(3), 1461–1481, doi: 10.1111/j.1365-246X.2006.03131.x.

Steinberger, B. and T. H. Torsvik (2012), A geodynamic model of plumes from the margins of Large Low Shear Velocity Provinces, *Geochem. Geophys. Geosyst.*, 13, Q01W09, doi: 10.1029/2011GC003808.

Todal, A. and O. Eldholm (1998), Continental margin of western India and Deccan large igneous province, *Mar. Geophys. Res.*, 20, 273–291, doi: 10.1023/A:1004640508371.

Torsvik, T. H., M. A. Smethurst, K. Burke, and B. Steinberger (2006), Large igneous provinces generated from the margins of the large low-velocity provinces in the deep mantle, *Geophys. J. Int.*, 167(3), 1447–1460, doi: 10.1111/j.1365-246X.2006.03158.x.

Torsvik, T. H., B. Steinberger, M. Gurnis, and C. Gaina (2010), Plate tectonics and net lithosphere rotation over the past 150 My, *Earth Planet. Sci. Lett.*, 291(1-4), 106–112, doi: 10.1016/j.epsl.2009.12.055.

Torsvik, T. H., H. Amundsen, E. H. Hartz, F. Corfu, N. Kusznir, C. Gaina, P. V. Doubrovine, B. Steinberger, L. D. Ashwal, and B. Jamtveit (2013), A Precambrian microcontinent in the Indian Ocean, *Nat. Geosci.*, 6(3), 223–227, doi: 10.1038/ngeo1736.

Torsvik, T. H., B. Steinberger, L. D. Ashwal, P. V. Doubrovine, and R. G. Trønnes (2016), Earth evolution and dynamics – a tribute to Kevin Burke, *Can. J. Earth Sci.*, 53(11), 1073–1087, doi: 10.1139/cjes-2015-0228.

Turcotte, D. L. and G. Schubert (2002), *Geodynamics,* 2nd ed., Cambridge Univ. Press, Cambridge, U. K.

van Hinsbergen, D. J. J., B. Steinberger, P. V. Doubrovine, and R. Gassmöller (2011), Acceleration and deceleration of India-Asia convergence since the Cretaceous: Roles of mantle plumes and continental collision, *J. Geophys. Res.*, 116, B06101, doi: 10.1029/2010JB008051.

3 Widespread Cenozoic volcanism in the North Atlantic-Greenland region explained by the Iceland plume

A version of this chapter has been submitted to Nature Geoscience as Steinberger, B., E. Bredow, S. Lebedev, A. Schaeffer and T. H. Torsvik (2017), Widespread Cenozoic volcanism in the North Atlantic-Greenland region explained by the Iceland plume.

Abstract

In the classical concept, a hotspot track is a line of age-progressive volcanics, formed as a plate moves over a stationary mantle plume. Defying this concept, intraplate volcanism in the North Atlantic / Greenland region occurred simultaneously over a wide area, particularly around 60 Ma, showing no resemblance to a classical hotspot track. Here we show that most of this volcanism can, nonetheless, be explained solely by the Iceland plume, interacting with spreading ridges, global mantle flow and a lithosphere of strongly variable thickness. An east-west corridor of thin lithosphere across central Greenland, as inferred from new, highly resolved tomographic images, could have formed as Greenland moved westward over the Iceland plume between 90 and 60 Ma. Our geodynamic model demonstrates how plume material may have accumulated in this corridor until it reached areas east and west of Greenland where the lithosphere was thin enough to initiate simultaneous volcanic activities at ≈ 62 Ma.

3.1 Introduction

62 Myr ago, simultaneous volcanism started in western Greenland, eastern Greenland and the British Isles (Torsvik et al., 2001) (Figure 3.1, inset histogram). The age distribution of volcanics peaks around 55 Ma, and it remains an open question whether this voluminous and widespread volcanism was caused by a single plume – either the plume head (Richards et al., 1989) or a preexisting plume (Morgan, 1983; Gaina et al., 2014) – and, if so, where it was positioned, and how large it was. When reconstructing plates to their location at 60 Ma (Figure 3.2), it becomes evident that plume material would still need to flow for more than 1000 km from a putative plume centre beneath eastern Greenland to some of the locations where volcanism occurred. Alternative explanations could be that there are more than one plume responsible (Ganerød et al., 2010; Rickers et al., 2013), a more sheetlike upwelling extended in north-south direction (Steinberger and Torsvik, 2012), or that the excess volcanism is caused by processes other than a mantle plume (Foulger and Anderson, 2005).

To address this question, we combine recent results from plate reconstructions, seismic tomography and geodynamic modeling to assess where the plume impacted and how and where plume material could have flowed beneath the lithosphere so as to give rise to the observed volcanism. The sub-lithospheric flow of hot asthenosphere is strongly influenced by the location of the hotspot relative to spreading ridges (Morgan, 1978) and by variations in lithosphere

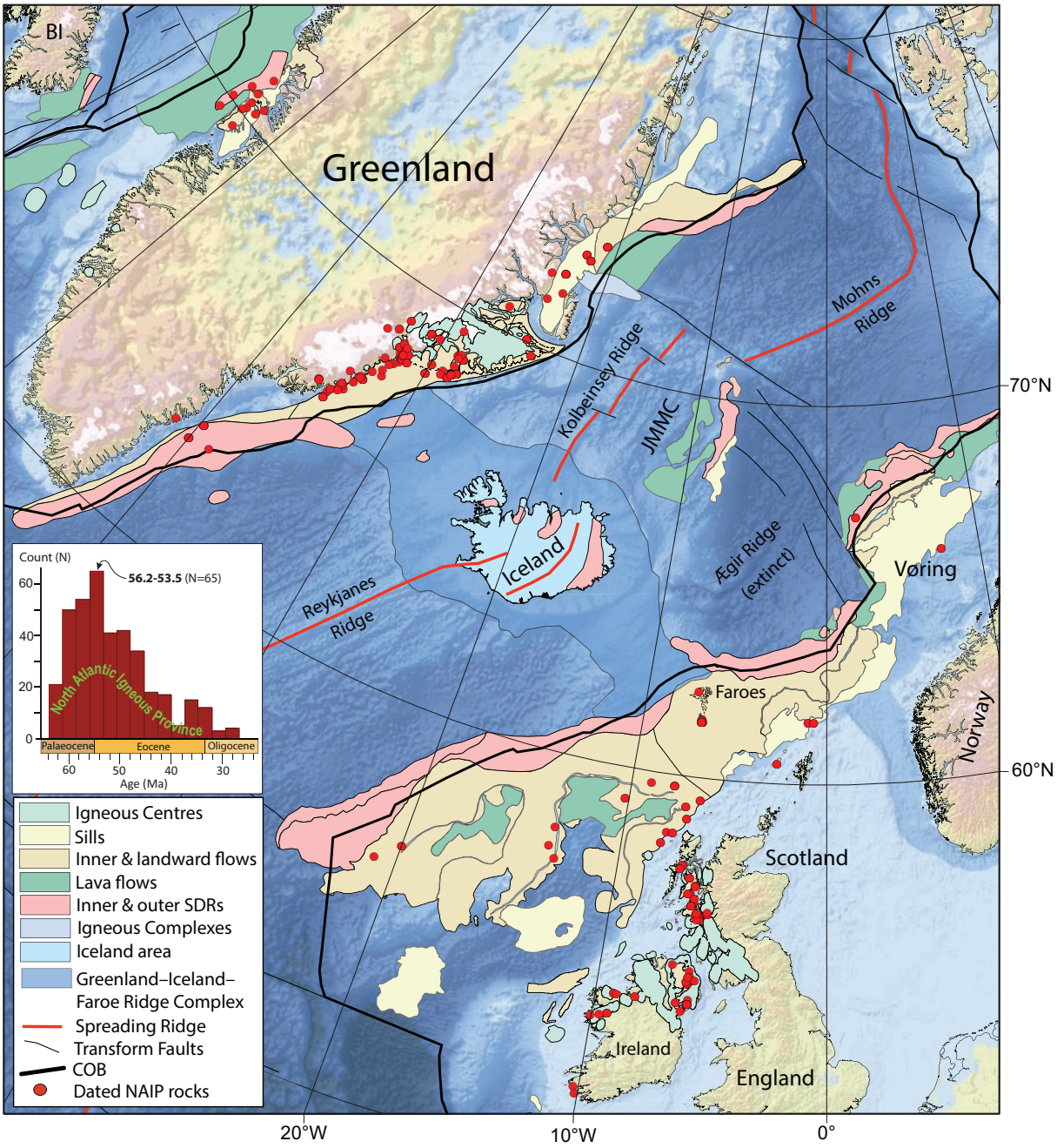

Figure 3.1: Distribution of the main onshore and offshore volcanic facies linked to the North Atlantic Igneous Province (NAIP), Iceland plume and the opening of the North Atlantic. We also show site locations for dated NAIP magmatism (red filled circles (Torsvik et al., 2001, 2015)) draped on a background bathymetry and subglacial topography map (ETOPO1). BI, Baffin Island; COB, Transition between continental and oceanic crust; JMMC, Jan Mayen microcontinent; SDRs, seaward dipping reflectors. Volcanic facies drawn from many sources, including Abdelmalak et al. (Abdelmalak et al., 2015). Inset histogram based on a compilation (Torsvik et al., 2015) of 383 isotope ages from NAIP.

thickness (Sleep, 1997), which can be estimated for the past by combining seismic tomography with plate reconstructions. We will first discuss how combining these ingredients may help qualitatively explain the distribution of volcanics. We will then test whether these findings can be substantiated by numerical simulations.

3.2 Past plume location

Presently, Iceland is an anomaly along the North Atlantic Ridge, with much thicker crust than normal sea floor, caused by the more intensive volcanism. Seismic tomography models show evidence for a hot upwelling in the upper mantle (Wolfe et al., 1997); some tomography models also indicate a lower mantle origin (Bijwaard and Spakman, 1999; French and Romanowicz, 2015), with the position of Iceland near the northern tip of the African Large Low Shear Velocity Province (LLSVP) a likely location from which the plume rises (Steinberger et al., 2015). Since it is the most suitable candidate, we will only consider the Iceland plume as possible source for widespread volcanism around 60 Ma, although other plumes such as Canary or Azores (Ganerød et al., 2010) or a more sheetlike upwelling (Steinberger and Torsvik, 2012) may also be responsible for some of the volcanics.

The motion of the Iceland plume is controlled by large-scale flow, which tilts and distorts the plume conduit as it rises through the slowly convecting mantle. When this motion is taken into account, models typically predict that around 60 Myr ago the Iceland plume was a few hundred km further east in the mantle than its present location, and has moved westward according to the predominant flow direction at the top of the lower mantle (Mihalffy et al., 2008; Torsvik et al., 2015).

3.3 Lithospheric plates and large-scale mantle flow through time

When the plate and plume motions are added, it turns out that the Iceland plume was most likely located beneath eastern (Doubrovine et al., 2012; Torsvik et al., 2015) or central (O'Neill et al., 2005) Greenland around 60 Ma. Here we will assume an East Greenland location. For comparison, assuming fixed hotspots has led to a predicted location in western Greenland (Lawver and Müller, 1994), although even earlier models (Vink, 1984; Morgan, 1981) also predicted a hotspot location in eastern Greenland at that time.

We derived present-day lithosphere thickness from seismic tomography for continents and sea floor ages (Müller et al., 2008) for oceans (see Methods). Lithosphere may become thicker with age, or thinner due to the influence of the plume (Rogozhina et al., 2016) or even thicken due to plume influence, if depleted material is left behind after volcanism underplates the base of the lithosphere (Yuan et al., 2017). However, here we simply backward-rotate continents, using our plate reconstruction (Doubrovine et al., 2012), while in the oceans we additionally consider that the lithosphere was thinner in the past because of its younger age. Figure 3.2 shows reconstructed lithosphere thickness and plume location.

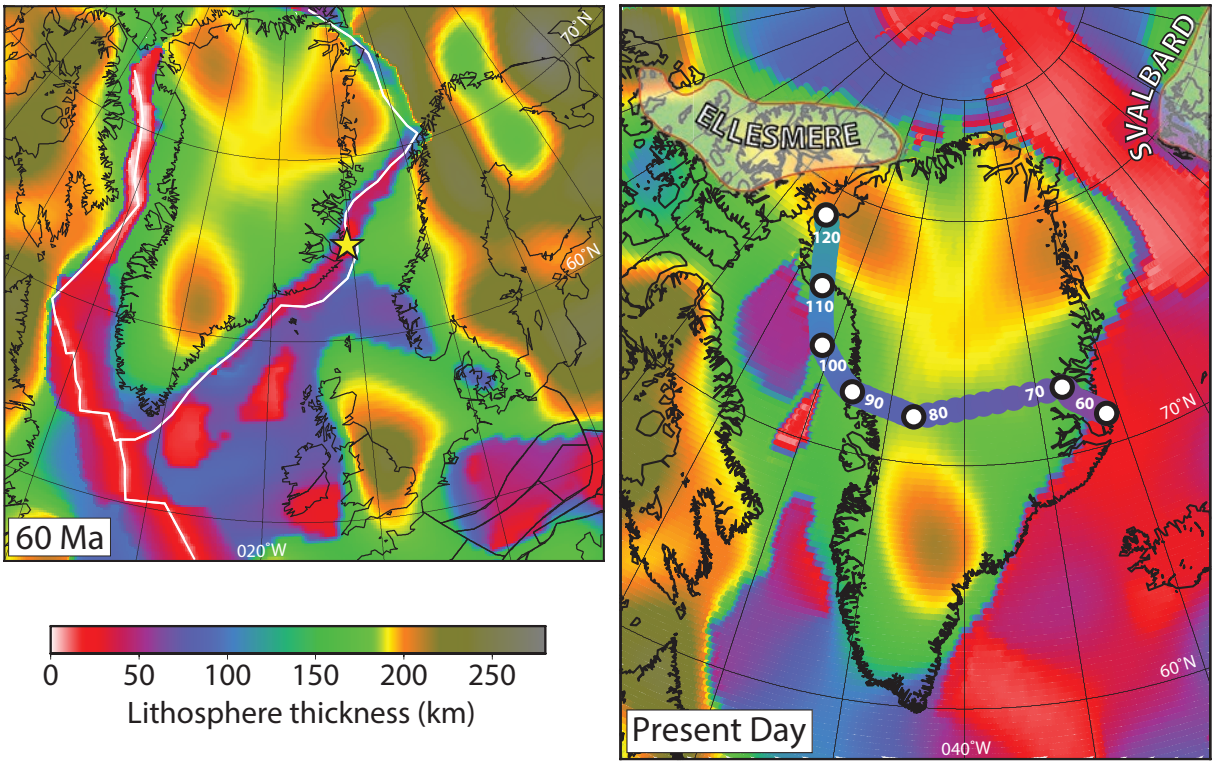

Figure 3.2: Lithosphere thickness and plume position at 60 Ma and present-day. In the present-day panel, lithosphere thickness is derived (Steinberger, 2016) from the Arctic tomography model AMISvArc (Lebedev et al., 2017) only, using the same parameters as for SL2013sv (Schaeffer and Lebedev, 2013), whereas for the 60 Ma reconstruction, it is also based on ocean floor ages (see Methods). White lines are plate boundaries. Plume position (Doubrovine et al., 2012) is shown as golden star. In the right panel, the reconstructed track on Greenland (Doubrovine et al., 2012; Torsvik et al., 2010) is shown for 120 – 60 Ma on the same color scale (ages [Ma] instead of lithosphere thickness [km]). As mantle flow reconstructions and hence hotspot motion become increasingly uncertain in the more distant past, we assume a fixed hotspot for ages > 60 Ma. Regions labelled Ellesmere and Svalbard are two parts of the High Arctic Large Igneous Province.

A large-scale mantle flow model is derived from global tomography converted to density anomalies and used as boundary condition for our regional numerical model. In more general terms, Steinberger et al. (2015) argued for an overall large-scale flow in a north-northwestern direction, consistent with the location of Iceland relative to the LLSVP, and tomographic images. Such a flow direction is also consistent with shear wave splitting results (Ito et al., 2015).

3.4 Qualitative model of plume-lithosphere interaction

The qualitative scenario that emerges if we combine models of plume motion, lithosphere thickness through time and large-scale mantle flow is similar to Vink (1984) in that the Iceland plume has been close to the North Atlantic spreading ridge since the initiation of spreading, and therefore the most voluminous volcanism did not occur directly above the hotspot but at the ridge location closest to the hotspot. This first formed the Vøring Plateau offshore central Norway (Figure 3.1) and later on the Greenland-Faeroe plateau.

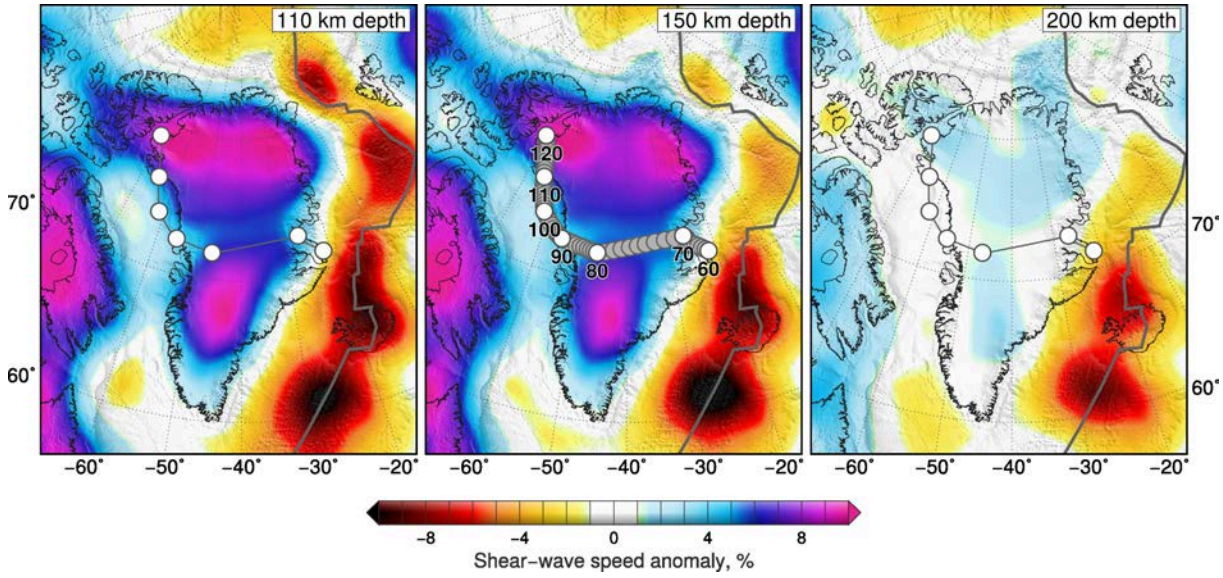

Figure 3.3: Arctic tomography model AMISvArc (Lebedev et al., 2017) beneath Greenland and surroundings. The reference value of the vertically-polarized S-wave speed in the mantle is 4.38 km/s. This value and deviations from it are at the reference period 50 s. Reconstructed hotspot track as in Figure 3.2 right.

Critically, where plume material is flowing to and where it comes close to the surface, and hence where volcanism can be expected, is affected by large-scale flow and lithosphere thickness. An east-west oriented thin-lithosphere corridor that we see in our models provides a simple yet elegant mechanism for how a single plume could feed roughly simultaneous volcanism on the east and west coasts of Greenland. This corridor is evident when looking at the tomography model AMISvArc which shows significantly reduced seismic velocities beneath the inferred passage of the Iceland hotspot, indicative of relatively warmer and thinner lithosphere (Lebedev et al., 2017) (Figure 3.3). Hot asthenosphere could flow westward following this corridor and, furthermore, the corridor itself could have been created by the earlier Late Cretaceous passage of Greenland over the plume (Figure 3.2 right), thus accumulating and trapping plume material in this corridor underneath thick continental lithosphere. Even earlier, around 130 – 120 Ma, parts of the High Arctic Large Igneous Province (HALIP), Ellesmere and Svalbard (Torsvik and Cocks, 2017) are reconstructed near the plume location, as is evident from the hotspot tracks in Figure 3.3 and 3.2, and could therefore be causally linked to the Iceland plume (see also Gaina et al. (2014)).

Although the lithosphere thickness may have changed during the rifting process, our reconstruction indicates that there may have already been a region of thin lithosphere between Greenland and Europe – even though they were much closer to each other – especially south of the plume, at 60 Ma. Material from the plume could then have been channelled along that corridor and led to volcanism in the British Tertiary Igneous Province (White and McKenzie, 1989) at $\approx$ 60 Ma.

3.5 A numerical model of plume melting beneath a moving lithosphere of variable thickness

In order to assess the spatial distribution and amount of basaltic volcanism due to a plume interacting with moving lithospheric plates of variable thickness and nearby spreading ridges, we set up a numerical model, using recently developed and validated methods (Gassmöller et al., 2016; Bredow et al., 2017) (see Methods). The plume is initiated with a large plume head at the base of the upper mantle at either 64 Ma (Model64Ma) or 115 Ma (Model115Ma). We use a plume head radius of 250 km, an excess temperature of 300 K and an inflow velocity of 20 cm/yr (comparable with recent models of the Tristan da Cunha (Gassmöller et al., 2016) and Réunion (Bredow et al., 2017) mantle plumes). The plume tail has an excess temperature of 250 K in agreement with literature estimates, which range between 186 K and 300 K (Putirka, 2008; Sleep, 1990; Schilling, 1991; Spice et al., 2016), a radius of 140 km and an inflow velocity of 6 cm/yr. These values result in a pure plume buoyancy flux of approximately 1150 kg/s, which is heightened by the global flow to a total range between 1250 kg/s and 2000 kg/s, in accordance with estimated values (Sleep, 1990; Schilling, 1991).

Figure 3.4 shows results for 68 Ma and 59 Ma for Model115Ma. At 68 Ma, plate motions are divergent between Greenland and North America. The plume has spread widely beneath the lithosphere, and trapped large amounts of hot material in the corridor across Greenland, above which the continental lithosphere is relatively thin, but too thick to enable melting. An arm extending to the south of Greenland is a remnant of the even more widely spread earlier plume head. At 59 Ma, accelerated rifting has started beneath Greenland and Europe, and volcanic activity occurs simultaneously both east and west of Greenland, as soon as the ponded plume material reaches areas where thin lithosphere and decompression along the mid-ocean ridges enable melting. This marks the onset of intense plume-ridge interaction, which is supported by plate motions and mantle flow, and continues until the present-day state of the model. The resulting total amount of plume-related melt in Model64Ma is shown in Figure 3.5 (top) and compared with a crustal thickness map derived from gravity inversion (Figure 3.5 bottom (Torsvik et al., 2015)). Features that are common to both maps include relatively thick crust along the Iceland-Greenland Ridge, near the Faroes, along the Norwegian continental margin, and on the Jan Mayen Microcontinent. The thickest oceanic crust occurs in the southeastern part of Iceland in both maps.

The distribution of melt produced in different time intervals is shown in Figure 3.6 and compared to locations of dated volcanics of same age. Again, we find considerable similarities, although melt is not produced quite as far south as the Tertiary volcanics in Scotland and Ireland. For Model64Ma (Fig. 3.6 top left), where the plume has always been beneath eastern Greenland or the Atlantic, volcanism only occurs within or near the opening Atlantic. However, with a plume active since 115 Ma, simultaneous volcanism around 60 Ma also occurs in Baffin Bay west of Greenland (Fig. 3.6 top right). Despite the much earlier impingement of the plume beneath the lithosphere, the first volcanics in this model only occur at 61 Ma. Before that, plume

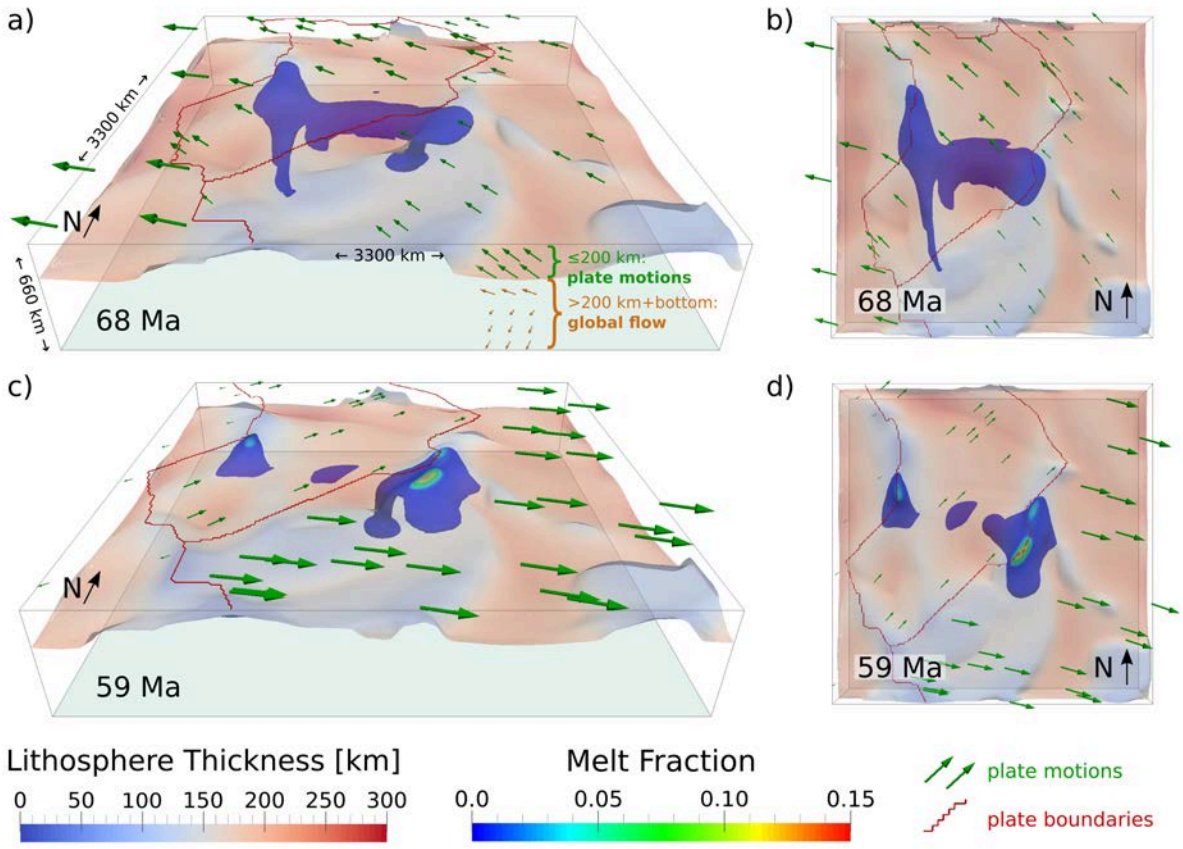

Figure 3.4: Numerical model (Model115Ma) of the Iceland plume, represented by the 100 K isocontour colored according to melt fraction. The plume is initiated at 115 Ma and we show two representative time frames in oblique and top view. Red lines are plate boundaries, green arrows represent plate velocities. The top left panel also illustrates side boundary conditions, based on plate motions and global mantle flow (see Methods).

material spreads beneath thick lithosphere, without any melt generation. Only around that time, due to rifting and incipient spreading, the lithosphere in Baffin Bay has sufficiently thinned such that the first melts are produced. At the same time, Greenland has moved westward, such that the plume is located sufficiently close to the nascent North Atlantic and can also produce melts there. Melting in Baffin Bay continues until the time interval 55 – 45 Ma in Model115Ma. Apart from this, the results for the two models are rather similar after 55 Ma, and Model115Ma results are therefore not shown for these later times.

3.6 Discussion

Interaction of a plume head or large pulse with a lithosphere of strongly variable thickness can create a distribution of volcanics very different from a classical hotspot track. If the Iceland plume was located near the eastern continental margin of Greenland around 60 Ma, a pulse at that time would have caused volcanism mainly along the opening rift between Greenland and Europe. Our numerical model yields plume-related volcanics along a large stretch of the

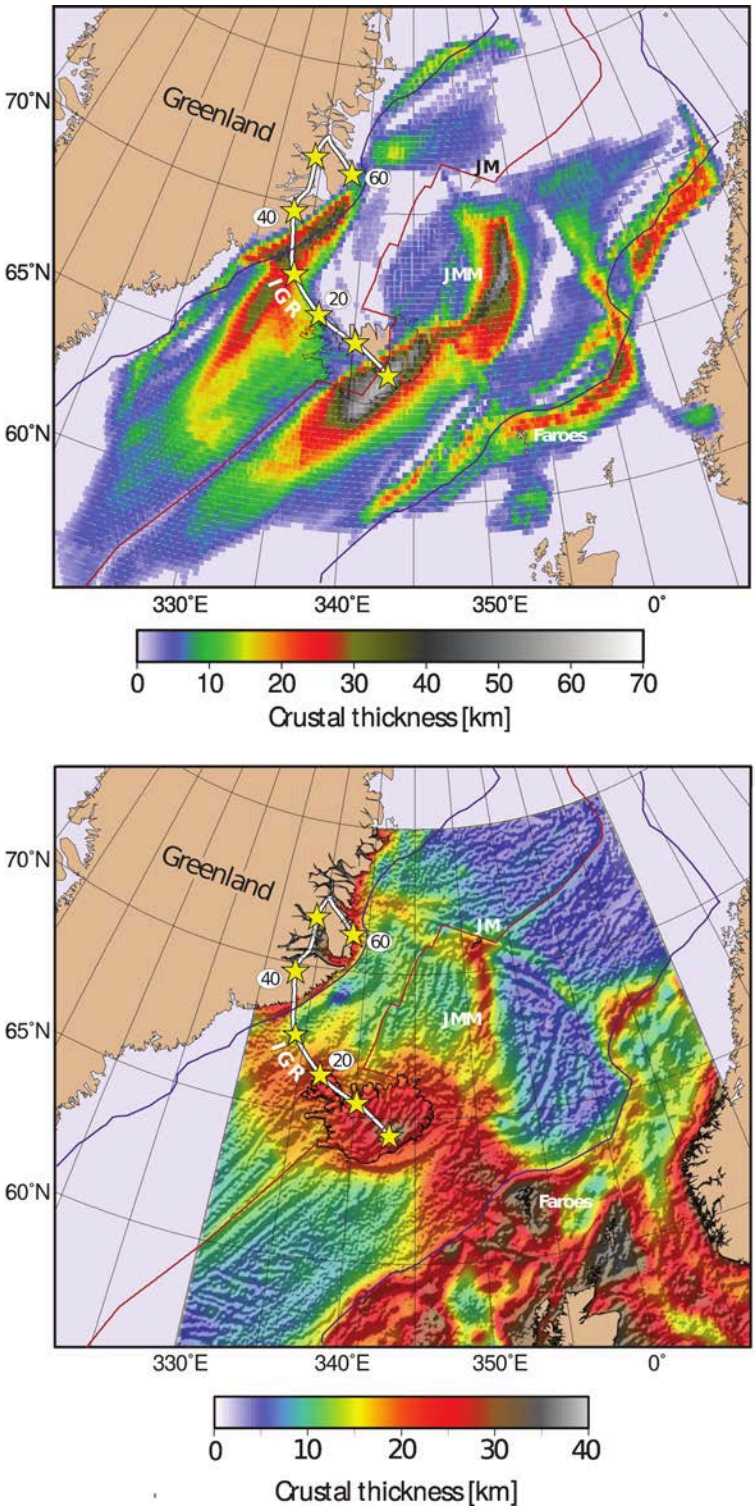

Figure 3.5: Top: Computed total crustal thickness produced by the plume only in Model64Ma. Melt that is generated is immediately extracted to the surface and rotated to its present location according to the plate reconstruction (Doubrovine et al., 2012; Torsvik et al., 2010). Bottom: Crustal thickness map based on gravity inversion (Torsvik et al., 2015). Yellow stars connected with white line show the 60 – 0 Ma Iceland hotspot track (Doubrovine et al., 2012; Torsvik et al., 2010). Red line is the North Atlantic spreading ridge, blue lines are the Continent-Ocean transition zones (Torsvik et al., 2015). IGR = Iceland Greenland Ridge; JM = Jan Mayen; JMM = Jan Mayen Microcontinent.

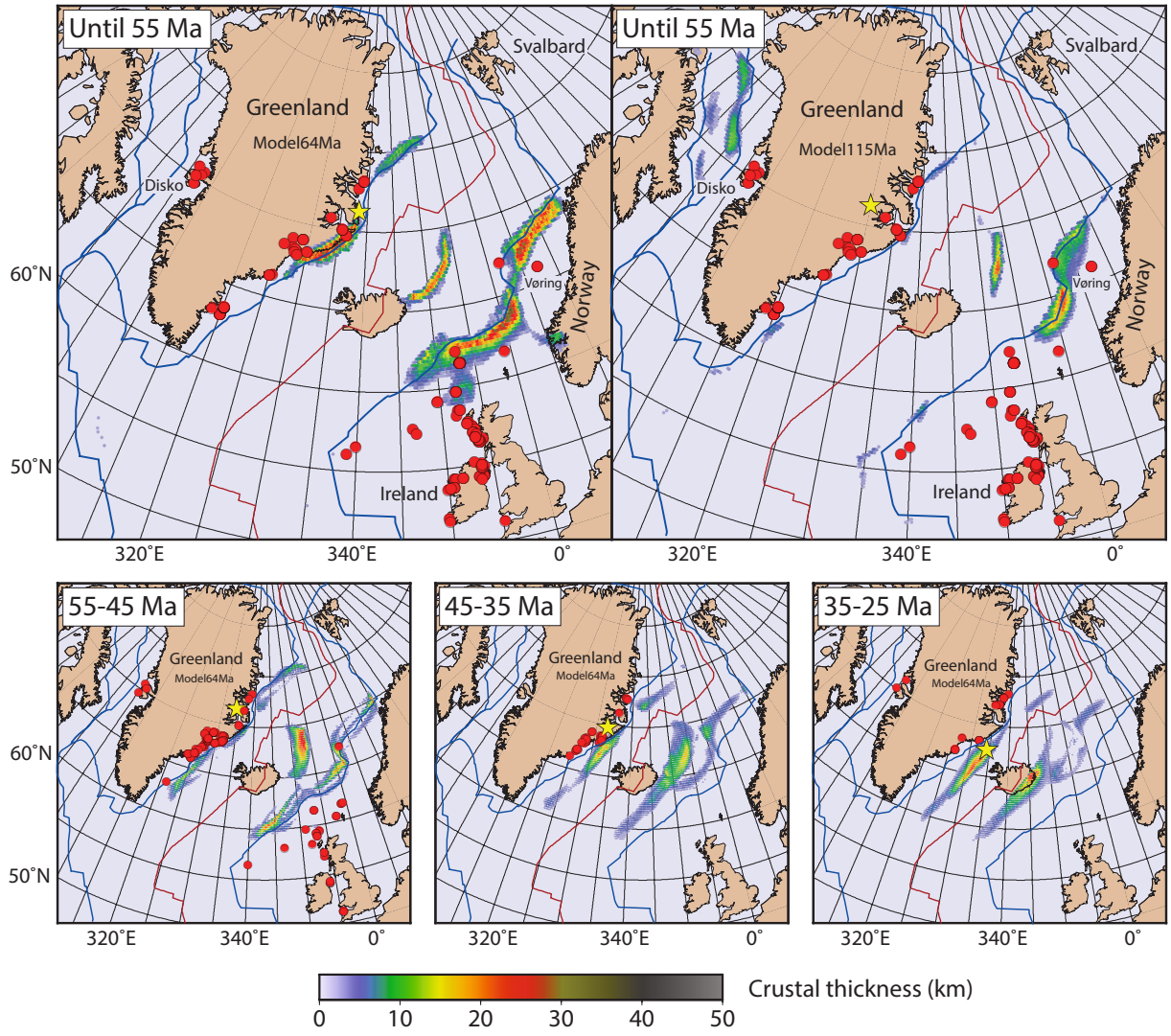

Figure 3.6: Computed melt produced in different time intervals, represented as present-day crustal thickness contribution (as in Figure 3.5). In Model115Ma the plume is initiated at 115Ma and has been displaced 300 km westward at 60 Ma, but at the same position as in Model64Ma from 50 Ma onward. This is meant to represent a smoothed-out Greenland plate motion, but instead of modifying the plate reconstructions (Doubrovine et al., 2012; Torsvik et al., 2010), we changed the hotspot position. All other panels are for Model64Ma. Corresponding hotspot location relative to Greenland at 60, 50, 40 and 30 Ma is shown as yellow stars. Red dots show dated volcanics in the same time intervals for an updated compilation (Torsvik et al., 2001).

rift that developed into the North Atlantic – on the European side between Faroes and North of Scotland, up to ≈ 800 km toward the southwest of the plume. However, a plume head of 500 km diameter, as assumed here, does not lead to volcanics as far away as western Scotland and Ireland where they also occurred around that time. A more sheet-like upwelling, extending in a north-south direction, which occurs in geodynamic models (Steinberger and Torsvik, 2012) at the northern tip of the African LLSVP could help explaining that the north-south extent of simultaneous volcanism that occurred around 60 Ma was even larger than modelled here. Assuming today's lithospheric thickness in Greenland, a plume head that impinged near the East Greenland margin around 60 Ma does not lead to volcanism west of Greenland around that time. However, if the plume has pre-existed, a sufficient amount of hot plume material may have accumulated, particularly along a corridor of relatively thin lithosphere, which is inferred from tomography, across Greenland toward Baffin Bay. After plate divergence thinned the lithosphere in Baffin Bay around 60 Ma, this could have led to volcanism. Comparison with computed hotspot tracks indicates that this corridor could have even been created by the passage of Greenland across the plume, heating and thinning the lithosphere. If the thin-lithosphere corridor is due to Greenland's passage over the hotspost at 60 – 80 Ma, the lithosphere within the corridor is likely to have been significantly thinner at 60 Ma than it is now, after cooling for 60 Myr. It is thus possible that even more hot asthenosphere of plume origin could have reached the west coast of Greenland than predicted by our model.

Compared to previous analytical and numerical models (Vink, 1984; Mihalffy et al., 2008; Ito et al., 2015) this work takes advantage of key new evidence yielded by new tomography, tomography-derived lithosphere thickness models, and plate reconstructions, as well as improved numerical modeling capabilities. Many previous tomography models included in a recent compilation (Steinberger et al., 2015) show evidence for thin lithosphere in eastern Greenland, near the supposed 60 Ma plume location, but not further west. Recently, thinned lithosphere beneath north-central Greenland has been proposed (Rogozhina et al., 2016) based on a P-wave (Jakovlev et al., 2012) and an S-wave (Rickers et al., 2013) tomographic model, as well as high geothermal flux inferred from ice-penetrating radar and ice core drilling data. The inferred thin lithosphere was linked to its passage over the Iceland plume. The thin-lithosphere corridor seen in our new tomography and lithospheric models is likely to show the complete extent of Greenland's lithosphere modified by the Iceland hotspot, as Greenland moved across it. Unlike the previously proposed areas of thinned lithosphere, the corridor connects the locations of abundant volcanism at the west and east coasts of Greenland, in contrast with the tomography models used by Rogozhina et al. (Rogozhina et al., 2016), which suggested cold, thick lithosphere beneath the volcanic areas on the Greenland's western coast, difficult to reconcile with the voluminous volcanism in those areas. The improvements in tomographic resolution given by our model is mainly due to waveform inversion of a very large dataset of fundamental and higher mode surface waves that constrained it, using all available broadband stations in the region and exploiting the high sensitivity of waveform data to lithospheric structure (Lebedev et al., 2017) (see Methods).

Compilations (Rogozhina et al., 2016; Gaina et al., 2014) show that the various proposed fixed and moving hotspot tracks across Greenland are substantially different. Our model considers motion of the Iceland plume from 60 Ma onwards. For earlier times, models of mantle flow, and hence hotspot motion, are increasingly unreliable, and we therefore assume a fixed hotspot position. This is presumably a reasonable approximation, as the Iceland plume appears to be a nearly stationary upwelling from the northern tip (Lekic et al., 2012) of the African LLSVP, and numerical models (Mihalffy et al., 2008; Doubrovine et al., 2012) yield limited hotspot motion also after 60 Ma. Importantly, the corresponding hotspot track (Doubrovine et al., 2012) provides one of the best matches with the East-West corridor across Greenland detected by tomography. Assuming hotspot fixity prior to 60 Ma, the earlier parts of the plume track follows the West coast of Greenland, where subsequently Baffin Bay opened, beginning near Ellesmere Island at 120 Ma, where parts of the HALIP formed around the same time (Gaina et al., 2014; Torsvik and Cocks, 2017).

The distribution of volcanism compares well with a crustal thickness map inferred from gravity inversion. However, some of the thick crust may be due to continental material, including fragments in the middle of the ocean (Torsvik et al., 2015). With the assumed size (500 km diameter) of the plume head or pulse around 60 Ma, volcanism does not spread as far south as Scotland and Ireland. Given that the estimates of $5-10\times10^6\,\mathrm{km}^3$, compiled (Storey et al., 2007) for the volume of volcanics, are very large compared to other LIPs, the 500 km diameter plume head may be considered a conservative estimate; it was more likely larger rather than smaller. The immediate cause of the British Tertiary Igneous Province could be thinning of the lithosphere, triggered potentially by a mantle upwelling, or, perhaps, by laterally transported hot asthenosphere. Alternatively, it could be due to deformation during the opening of the North Atlantic. The distribution of the volcanism (North Atlantic Volcanic Province) is a good proxy for thin lithospheres. The Irish Sea may have been relatively far from the hotspot, but locations of NAVP volcanism are scattered between them, and those can be taken as fingerprints left by the hot asthenosphere flow at the time. Lithosphere thickness variations lead to a pattern of melting that is not radially symmetric; for example, our model predicts regions of volcanism extending toward Scotland and Southern Norway (Figure 3.5 bottom). However, the dynamics of the plume itself may lead to viscous fingering (Schoonman et al., 2017).

Our model helps to reconcile seemingly contradictory older models: On one hand, it has been proposed that the large volcanic outpourings in the incipient North Atlantic are caused by the initial Iceland plume head. On the other hand, a much earlier origin has been proposed, perhaps linking the Iceland plume to volcanics in Ellesmere and Svalbard. Here we find that even with a plume much older than 60 Ma, volcanism only starts around this time, when plume material finally finds its way to regions of thin lithosphere east and west of Greenland. However, before that time, plume material has been accumulated at the base of the lithosphere such that, when melting finally occurs, it is rather massive. This resembles the impinging of a plume head, even though plume material has gradually accumulated over tens of millions of years. In this way, the amounts and distribution of volcanism east of Greenland are in fact rather similar in the

cases where a plume head hits at around 62 Ma, and where the plume has continuously existed since much earlier. We suggest that flood basalts do not always represent the arrival of plume heads from the deep mantle (Richards et al., 1989) but may also occur due to interaction of a plume with a lithosphere (Sleep, 1997) with thickness varying in space and time.

Acknowledgements

The geodynamic models were computed with the open-source software ASPECT (http://aspect.dealii.org) and performed with resources provided by the North-German Supercomputing Alliance (HLRN). We thank Juliane Dannberg, Simon Williams and Nicky White for comments and suggestions. This publication has emanated from research supported in part by research grants from Science Foundation Ireland (SFI) under grant number 13/CDA/2192 and grant number 13/RC/2092, co-funded under the European Regional Development Fund and by iCRAG industry partners. B.S. and T.H.T. also acknowledge support from the Research Council of Norway, through its Centre of Excellence scheme, project number 223272 (CEED).

3.7 Methods

3.7.1 Geodynamic model

Apart from minor modifications, the work flow essentially follows the steps described in Bredow et al. (Bredow et al., 2017): The computations are carried out with the mantle convection code ASPECT (Bangerth et al., 2017; Kronbichler et al., 2012) in a 3-D Cartesian box of dimensions length × width × height = 3300 × 3300 × 660 km from an inital time (120 Ma or 80 Ma) until present. The temperature field is prescribed at first to take into account the reconstructed lithosphere thickness distribution at the initial time and later as time-dependent boundary conditions. Velocity boundary conditions at the surface and the upper 200 km of the side boundaries simulate plate motions and are derived from a plate reconstruction model (see next subsection). The global flow surrounding the model domain is derived from a global mantle flow model (see below) and prescribed at the side boundaries below 200 km and at the base of the model box. All boundary conditions are time-dependent and prescribed at all times. Since – due to the transformation from spherical to Cartesian coordinates – the global flow and plate velocities do not exactly correspond to each other, they are smoothly interpolated at 200 km depth at the side boundaries. In addition, plume inflow at the bottom of the box is prescribed at a location inferred from a global model (see below). To maintain conservation of mass, every simulation runs twice and the net mass flux from the first simulation is used to correct the velocity boundary conditions for the second simulation. This correction is rather small and results with and without are visually very similar.

Global mantle flow is computed in terms of spherical harmonics (Hager and O'Connell, 1979, 1981), for a given 3-dimensional mantle density structure, radial viscosity profile, prescribed surface plate motions (see next subsection) and a free-slip core-mantle boundary (CMB). These

plate motions include a net rotation component, and in order to maintain this surface net rotation, but with strongly reduced net rotation in the deep mantle, we use a fixed CMB for the toroidal degree one flow component only. Density anomalies are backward advected (Steinberger and O'Connell, 1998) in the flow field to 68 Ma, and kept constant before that. The global flow model for present-day has been described in (Steinberger, 2016): The density model is based on surface wave tomography model (Schaeffer and Lebedev, 2013) in the upper 200 km and the 2010 update of a whole-mantle model (Grand, 2002) below that. For most of the mantle, we use a thermal scaling to density (Figure 3A of Steinberger (Steinberger, 2016)), however, given that both continental lithosphere and the LLSVP of the lowermost mantle are likely chemically distinct, we use a different scaling there: Inside the continental lithosphere (see subsection below) shallower than 150 km depth we instead set the density anomaly to a constant 0.2 %. Inside the LLSVPs, a density anomaly of 1.2 % has been added. LLSVPs are assumed to be in the lowermost 300 km of the mantle wherever seismic anomalies are more than 1 % negative. For viscosity, we use the red profile in Figure 3A of Steinberger (Steinberger, 2016), with viscosity increasing from $\approx 10^{20}$ Pas in the asthenosphere to nearly 10^{23} Pas in the lower mantle, but again decreasing to below 10^{21} Pas at the CMB.

The motion of the plume is computed following the method first developed by Steinberger and O'Connell (1998) with parameters as in Steinberger et al. (2004): The plume conduit is assumed to be initially (at 60 Ma) vertical and subsequently distorted in, but also buoyantly rising through mantle flow. A vertical plume conduit at 60 Ma corresponds to the assumption that the plume conduit was established by a plume head rising comparatively fast through the mantle. Alternatively, in case a pre-existing plume is assumed, it may represent a large pulse rising through, and straightening out the conduit. In this case, we had used an earlier tomography model (Becker and Boschi, 2002), and somewhat different viscosity and scaling from seismic velocity to density (Steinberger and Calderwood, 2006) (model 2b of that paper; scaling from seismic velocity to density reduced by a factor 0.5 in the upper 220 km) to compute flow. Since this model fits the geoid well, we expect that it gives a realistic prediction of large-scale flow in the lower mantle, which is relevant for hotspot motion. In contrast, the model used to compute inflow and outflow at the boundaries of the box gives a better prediction of dynamic topography, therefore we expect that it realistically includes more details of upper mantle flow. From this global model of hotspot motion, the plume position at depth 660 km is extracted to prescribe the plume influx into the regional model box. Since the regional model is initiated at 64 Ma to allow for rising of the plume head, a constant position is assumed 64 – 60 Ma. In Model115Ma, it is kept in the same position as the reference case until 80 Ma, is 300 km further west 70 – 60 Ma, 150 km further west and 100 km further south at 55 Ma, and in the same position as the reference case from 50 Ma, with linear interpolation. This is meant to compensate for a kink in the plate motion model, and should mimic the case where the plume moves in the same way after 60 Ma and is fixed before that, with a smoothed-out plate motion model. Given the increasing uncertainties in models of mantle flow and hotspot motion further back in time, we regard it as justified to revert to a model meant to represent a fixed hotspot before 60 Ma.

Melting in the geodynamic model depends on pressure and temperature and is calculated based on the parametrization for batch melting of anhydrous peridotite (Katz et al., 2003). In a postprocessing routine, the melt produced in each time step is instantly extracted to the surface and moved with the according plate motions. As in Bredow et al. (2017), we employ a dehydration rheology and a depletion buoyancy in our models.

3.7.2 Plate reconstructions

Where the plume was located relative to the overlying lithosphere depends on both plate motions and the motion of the plume in the same reference frame. Here we adopt absolute plate motions in a global moving hotspot reference frame (GMHRF) (Doubrovine et al., 2012). This reference frame is aimed at optimally fitting geometry of and age progression along several hotspot tracks while taking hotspot motion into account. Since the Iceland plume does not show a classical hotspot track, it is not included in devising this reference frame. Hotspot reference frames that are only for the Indo-Atlantic hemisphere (O'Neill et al., 2005) somewhat differ from a global reference frame that also takes hotspot tracks in the Pacific (Doubrovine et al., 2012) into account. In particular, around 60 Ma, in an Indo-Atlantic reference frame the Iceland plume is located further west relative to Greenland – beneath central to eastern Greenland rather than beneath its eastern coast.

Relative plate motions and plate boundaries in 10 Myr intervals are initally from (Torsvik et al., 2010), but plate boundaries are transferred with a routine described in that paper to the GMHRF (Doubrovine et al., 2012). They are then converted to cartesian box coordinates with a Lambert azimuthal equal-area projection centered on 17° W 64° N. The same projection and conversion is also used for the models of large-scale mantle flow, hotspot motion and lithosphere thickness models described in this methods section. Interpolation from the 10 Myr intervals to 1 Myr is done using a semi-automated procedure where essentially corresponding features in the plate boundaries (ridge segments, transform faults) are identified and matched by eye, and then automatically interpolated.

3.7.3 Mantle Tomography model AMISvArc

AMISvArc is a new upper-mantle shear-wave speed model of the circum-Arctic region (Lebedev et al., 2017). It is constructed as a global model using the same methodology and similar datasets as the recently published models Sl2016svA (Schaeffer et al., 2016), SL2013NA (Schaeffer and Lebedev, 2014), and SL2013sv (Schaeffer and Lebedev, 2013), but with substantially more data in the Arctic.

The inversion procedure comprises three steps. First, the Automated Multimode Inversion of surface and S wave-forms (AMI (Lebedev et al., 2005)) is applied to a pre-processed dataset of displacement seismograms. AMI performs accurate, automated processing of massive volumes of broadband waveform data, applying elaborate case-by-case selection of time-frequency windows and relative weighting of the fundamental and higher mode arrivals (S and multiple-S waves),

while enforcing a strict misfit criterion across all windows. Each successfully fit seismogram yields a set of linear equations with uncorrelated uncertainties that describe 1D perturbations in S- and P-wave velocities within approximate finite-width sensitivity volumes between the source and receiver, with respect to a global 3D reference model. The 3D reference model comprises the crustal model CRUST2 (Bassin et al., 2000) smoothed across its 2° cell boundaries and augmented with global topographic and bathymetric databases and, beneath the Moho, the global 1D reference model AK135 (Kennett et al., 1995), recomputed at a reference period of 50 s. Crustal structure, i.e., the deviations from the 3D reference model at the 3 – 4 crustal grid knots (depths of 7, 20, 36 and 56 km) are solved for in the inversion, instead of adopting the common assumption of fixed crustal structure or of crustal corrections. Errors in the Moho depth are compensated primarily by changes in the lower-crustal and uppermost mantle velocities (Lebedev et al., 2013).

In the second step, linear equations from all seismograms successfully fit by AMI (for a detailed overview of the results of waveform fitting, see Schaeffer and Lebedev (Schaeffer and Lebedev, 2013)) are combined into a single linear system and solved for the 3D distribution in isotropic P- and S-wave speeds and 2Ψ azimuthal anisotropy of S-wave velocity (Schaeffer et al., 2016), with respect to a modified 3D reference model that now comprises CRUST2 in the crust and the 1D upper mantle average taken from our own tomography (Lebedev and Hilst, 2008). The inversion is performed with the LSQR method (Paige and Saunders, 1982), subject to regularization (norm damping, lateral and vertical smoothing).

The third step of the procedure is the outlier analysis (Lebedev and Hilst, 2008; Schaeffer and Lebedev, 2013) aimed at selecting only the most mutually consistent seismogram fits for the final model. This analysis exploits the substantial redundancy of the dataset in order to remove the data most affected by errors (coming from event mislocations, etc). The starting dataset used in constraining AMISvArc includes waveform fits from the models SL2013NA and SL2013sv, and additional, recently recorded or recently made available, data from stations in the Arctic region (Lebedev et al., 2017). The total dataset includes more than one million vertical component seismograms successfully fit using AMI, recorded at more than 4600 stations globally. Outlier analysis was used to select a subset of 830,000 most mutually consistent waveform fits for an initial inversion; a final step of outlier analysis reduced the number of waveform fits to 817,200.

3.7.4 Lithosphere Thickness

Present-day lithosphere thickness on continents is computed based on the tomography model AMISvArc (Lebedev et al., 2017) (see previous section) using the same procedure and parameters as in the reference case of Steinberger (Steinberger, 2016). Conceptually, this model is based on the assumption that, in the global average, the temperature profile in the top thermal boundary layer of the mantle, which includes the lithosphere, follows an error function profile. It is further considered that compositional anomalies also contribute to seismic velocity anomalies. We assume that, on global average, this additonal contribution has a depth dependence that also follows an error function profile with the same scaling depth. Further, we assume these

compositional anomalies only occur inside the lithosphere and not at the LAB. Under these assumptions, we can now convert seismic velocity anomalies to absolute temperature, and we set the LAB to a constant temperature such that the temperature difference between LAB and surface is 84.3%=erf(1) of the total difference between (adiabatic) mantle potential temperature and surface temperature. Scaling depth of the error function and the compositional contribution to the global average of seismic velocity are two free parameters in this model, and they are adjusted (for a given tomography model) such that the oceanic depth versus age curve (assuming isostasy) is optimally matched.

Present-day continental lithosphere thickness grids are then assigned to four different plates North America, Greenland, Jan Mayen and Eurasia and moved back in time according to the respective plate rotations. In the oceans (wherever the age grid (Müller et al., 2008) is defined), present-day lithosphere thickness is computed from sea floor age with a diffusivity $8 \times 10^{-7} \mathrm{m}^2\mathrm{s}^{-1}$. Lithosphere thickness in the past is again determined with backward-rotation, but also taking into account the younger age at past times. Past lithosphere thickness determined in this way is applied to the numerical model at the inital time (either 80 Ma or 120 Ma) for the whole box, but afterward only at the sides, where material moves into the box. Elsewhere, the thickness of lithosphere that either moves into the box or gets created at the ridge is computed self-consistently, such that in effect the lithosphere thickness in our numerical model is very similar to, but not exactly the same as in Figure 3.2 left.

Code Availability

The version of ASPECT we used to run our models is available online (https://github.com/ebredow/aspect/tree/reunion_plume_model).

Data Availability

All of the input files that are required to reproduce this study are provided upon request.

References

Abdelmalak, M. M., T. B. Andersen, S. Planke, J. I. Faleide, F. Corfu, C. Tegner, G. E. Shephard, D. Zastrozhnov, and R. Myklebust (2015), The ocean-continent transition in the mid-Norwegian margin: Insight from seismic data and an onshore Caledonian field analogue, *Geology*, 43(11), 1011–1014, doi: 10.1130/G37086.1.

Bangerth, W., J. Dannberg, R. Gassmöller, T. Heister, et al. (2017), *ASPECT: Advanced Solver for Problems in Earth's ConvecTion, User Manual,* doi: 10.6084/m9.figshare.4865333.

Bassin, C., G. Laske, and G. Masters (2000), The current limits of resolution for surface wave tomography in North America, *EOS, Trans Am. Geophys. Un.*, 81, F897.

Becker, T. W. and L. Boschi (2002), A comparison of tomographic and geodynamic mantle models, *Geochem., Geophys., Geosys.*, 3, 1003, doi: 10.1029/2001GC000168.

Bijwaard, H. and W. Spakman (1999), Tomographic evidence for a narrow whole mantle plume below Iceland, *Earth Planet. Sci. Lett.*, 166(3-4), 121–126, doi: 10.1016/S0012-821X(99)00004-7.

Bredow, E., B. Steinberger, R. Gassmöller, and J. Dannberg (2017), How plume-ridge interaction shapes the crustal thickness pattern of the Réunion hotspot track, *Geochem. Geophys. Geosyst.*, 18(8), 2930–2948, doi: 10.1002/2017GC006875.

Doubrovine, P. V., B. Steinberger, and T. H. Torsvik (2012), Absolute plate motions in a reference frame defined by moving hot spots in the Pacific, Atlantic, and Indian oceans, *J. Geophys. Res.*, 117, B09101, doi: 10.1029/2011JB009072.

Foulger, G. R. and D. L. Anderson (2005), A cool model for the Iceland hotspot, *J. Volcanol. Geoth. Res.*, 141(1-2), 1–22, doi: https://doi.org/10.1016/j.jvolgeores.2004.10.007.

French, S. W. and B. Romanowicz (2015), Broad plumes rooted at the base of the Earth's mantle beneath major hotspots, *Nature*, 525, 95–99, doi: 10.1038/nature14876.

Gaina, C., S. Medvedev, T. H. Torsvik, and S. C. Werner (2014), 4D Arctic: A Glimpse into the Structure and Evolution of the Arctic in the Light of New Geophysical Maps, Plate Tectonics and Tomographic Models, *Surv. Geophys.*, 35, 1095–1122, doi: 10.1007/s10712-013-9254-y.

Ganerød, M., M. A. Smethurst, T. H. Torsvik, T. Prestvik, S. Rousse, C. McKenna, D. J. J. Van Hinsbergen, and B. W. H. Hendriks (2010), The North Atlantic Igneous Province reconstructed and its relation to the plume generation zone: the Antrim Lava Group revisited, *Geophys. J. Int.*, 182, 183–202, doi: 10.1111/j.1365-246X.2010.04620.x.

Gassmöller, R., J. Dannberg, E. Bredow, B. Steinberger, and T. H. Torsvik (2016), Major influence of plume-ridge interaction, lithosphere thickness variations, and global mantle flow on hotspot volcanism – The example of Tristan, *Geochem. Geophys. Geosyst.*, 17, 1454–1479, doi: 10.1002/2015GC006177.

Grand, S. P. (2002), Mantle shear-wave tomography and the fate of subducted slabs, *Phil. Trans. R. Soc. Lond. A*, 360, 2475–2491.

Hager, B. H. and R. J. O'Connell (1979), Kinematic models of large-scale flow in the Earth's mantle, *J. Geophys. Res.*, 84(B3), 1031–1048, doi: 10.1029/JB084iB03p01031.

Hager, B. H. and R. J. O'Connell (1981), A simple global model of plate dynamics and mantle convection, *J. Geophys. Res.*, 86(B6), 4843–4867, doi: 10.1029/JB086iB06p04843.

Ito, G., R. Dunn, and A. Li (2015), The origin of shear wave splitting beneath Iceland, *Geophys. J. Int.*, 201(3), 1297–1312, doi: 10.1093/gji/ggv078.

Jakovlev, A. V., N. A. Bushenkova, I. Y. Koulakov, and N. L. Dobretsov (2012), Structure of the upper mantle in the Circum-Arctic region from regional seismic tomography, *Russ. Geol. Geophys.*, 53, 963–971, doi: 10.1016/j.rgg.2012.08.001.

Katz, R. F., M. Spiegelman, and C. H. Langmuir (2003), A new parameterization of hydrous mantle melting, *Geochem. Geophys. Geosyst.*, 4(9), 1073, doi: 10.1029/2002GC000433.

Kennett, B. L. N., E. R. Engdahl, and R. Buland (1995), Constraints on seismic velocities in the Earth from traveltimes, *Geophys. J. Int.*, 122, 108–124, doi: 10.1111/j.1365-246X.1995.tb03540.x.

Kronbichler, M., T. Heister, and W. Bangerth (2012), High accuracy mantle convection simulation through modern numerical methods, *Geophys. J. Int.*, 191(1), 12–29, doi: 10.1111/j.1365-246X.2012.05609.x.

Lawver, L. A. and R. D. Müller (1994), Iceland hotspot track, *Geology*, 22(4), 311–314, doi: 10.1130/0091-7613(1994)022⟨0311:IHT⟩2.3.CO;2.

Lebedev, S. and R. D. van der Hilst (2008), Global upper-mantle tomography with the automated multimode inversion of surface and S-wave forms, *Geophys. J. Int.*, 173(2), 505–518, doi: 10.1111/j.1365-246X.2008.03721.x.

Lebedev, S., G. Nolet, T. Meier, and R. D. van der Hilst (2005), Automated multimode inversion of surface and S waveforms, *Geophys. J. Int.*, 162(3), 951–964, doi: 10.1111/j.1365-246X.2005.02708.x.

Lebedev, S., J. M.-C. Adam, and T. Meier (2013), Mapping the Moho with seismic surface waves: A review, resolution analysis, and recommended inversion strategies, *Tectonophysics*, 609, 377–394, doi: 10.1016/j.tecto.2012.12.030.

Lebedev, S., A. J. Schaeffer, J. Fullea, and V. Pease (2017), Seismic tomography of the Arctic region: inferences for the thermal structure and evolution of the lithosphere, *Geological Society, London, Special Publications*, 460, doi: 10.1144/SP460.10.

Lekic, V., S. Cottaar, A. Dziewonski, and B. Romanowicz (2012), Cluster analysis of global lower mantle tomography: A new class of structure and implications for chemical heterogeneity, *Earth Planet. Sci. Lett.*, 357–358, 68–77, doi: 10.1016/j.epsl.2012.09.014.

Mihalffy, P., B. Steinberger, and H. Schmeling (2008), The effect of the large-scale mantle flow field on the Iceland hotspot track, *Tectonophysics*, 447, 5–18, doi: 10.1016/j.tecto.2006.12.012.

Morgan, W. J. (1978), Rodriguez, Darwin, Amsterdam, ..., A second type of Hotspot Island, *J. Geophys. Res.*, 83(B11), 5355–5360, doi: 10.1029/JB083iB11p05355.

Morgan, W. J. (1981), "13. Hotspot tracks and the opening of the Atlantic and Indian Oceans". *Volume 7: The oceanic lithosphere*, 443–487.

Morgan, W. J. (1983), Hotspot Tracks and the early rifting of the Atlantic, *Tectonophysics*, 94, 123–139, doi: 10.1016/0040-1951(83)90013-6.

Müller, R. D., M. Sdrolias, C. Gaina, and W. R. Roest (2008), Age, spreading rates, and spreading asymmetry of the world's ocean crust, *Geochem. Geophys. Geosyst.*, 9, Q04006, doi: 10.1029/2007GC001743.

O'Neill, C., R. D. Müller, and B. Steinberger (2005), On the uncertainties in hotspot reconstructions, and the significance of moving hotspot reference frames, *Geochem., Geophys., Geosys.*, 6, Q04003, doi: 10.1029/2004GC000784.

Paige, C. C. and M. A. Saunders (1982), LSQR: An algorithm for sparse linear equations and sparse least squares, *ACM transactions on mathematical software*, 8(1), 43–71.

Putirka, K. (2008), Excess temperatures at ocean islands: Implications for mantle layering and convection, *Geology*, 36(4), 283–286, doi: 10.1130/G24615A.1.

Richards, M. A., R. A. Duncan, and V. E. Courtillot (1989), Flood Basalts and Hot-Spot Tracks: Plume Heads and Tails, *Science*, 246, 103–107, doi: 10.1126/science.246.4926.103.

Rickers, F., A. Fichtner, and J. Trampert (2013), The Iceland–Jan Mayen plume systemand its impact on mantle dynamics in the North Atlantic region: evidence fromfull-waveform inversion, *Earth Planet. Sci. Lett.*, 367, 39–51, doi: 10.1016/j.epsl.2013.02.022.

Rogozhina, I., A. Petrunin, A. P. M. Vaughan, B. Steinberger, J. V. Johnson, M. Kaban, R. Calov, F. Rickers, M. Thomas, and I. Koulakov (2016), Melting at the base of the Greenland Ice Sheet explained by Iceland hotspot history, *Nat. Geosci.*, 9, 366–369, doi: 10.1038/ngeo2689.

Schaeffer, A. J. and S. Lebedev (2013), Global shear speed structure of the upper mantle and transition zone, *Geophys. J. Int.*, 194, 417–449, doi: 10.1093/gji/ggt095.

Schaeffer, A. J. and S. Lebedev (2014), Imaging the North American continent using waveform inversion of global and USArray Data, *Earth Planet. Sci. Lett.*, 402, 26–41, doi: 10.1016/j.epsl.2014.05.014.

Schaeffer, A. J., S. Lebedev, and T. W. Becker (2016), Azimuthal seismic anisotropy in the Earth's upper mantle and the thickness of tectonic plates, *Geophys. J. Int.*, 207, 901–933, doi: 10.1093/gji/ggw309.

Schilling, J.-G. (1991), Fluxes and excess temperatures of mantle plumes inferred from their interaction with migrating mid-ocean ridges, *Nature*, 352, 397–403, doi: 10.1038/352397a0.

Schoonman, C. M., N. J. White, and D. Pritchard (2017), Radial viscous fingering of hot asthenosphere within the Icelandic plume beneath the North Atlantic Ocean, *Earth Planet. Sci. Lett.*, 468, 51–61, doi: 10.1016/j.epsl.2017.03.036.

Sleep, N. H. (1990), Hotspots and mantle plumes: Some phenomenology, *J. Geophys. Res.*, 95(B5), 6715–6736, doi: 10.1029/JB095iB05p06715.

Sleep, N. H. (1997), Lateral flow and ponding of starting plume material, *J. Geophys. Res.*, 102(B5), 10001–10012, doi: 10.1029/97JB00551.

Spice, H. E., J. G. Fitton, and L. A. Kirstein (2016), Temperature fluctuation of the Iceland mantle plume through time, *Geochem., Geophys., Geosys.*, 17(2), 243–254, doi: 10.1002/2015GC006059.

Steinberger, B. and A. Calderwood (2006), Models of large-scale viscous flow in the Earth's mantle with constraints from mineral physics and surface observations, *Geophys. J. Int.*, 167, 1461–1481, doi: 10.1111/j.1365-246X.2006.03131.x.

Steinberger, B. and R. J. O'Connell (1998), Advection of plumes in mantle flow: implications for hotspot motion, mantle viscosity and plume distribution, *Geophysical Journal International*, 132(2), 412–434, doi: 10.1046/j.1365-246x.1998.00447.x.

Steinberger, B., R. Sutherland, and R. J. O'Connell (2004), Prediction of Emperor-Hawaii seamount locations from a revised model of global plate motion and mantle flow, *Nature*, 430, 167–173, doi: 10.1038/nature02660.

Steinberger, B., W. Spakman, P. Japsen, and T. H. Torsvik (2015), The key role of global solid-Earth processes in preconditioning Greenland's glaciation since the Pliocene, *Terra Nova*, 27(1), 1–8, doi: 10.1111/ter.12133.

Steinberger, B. (2016), Topography caused by mantle density variations: observation-based estimates and models derived from tomography and lithosphere thickness, *Geophys. J. Int.*, 205, 604–621, doi: 10.1093/gji/ggw040.

Steinberger, B. and T. H. Torsvik (2012), A geodynamic model of plumes from the margins of Large Low Shear Velocity Provinces, *Geochem. Geophys. Geosyst.*, 13, Q01W09, doi: 10.1029/2011GC003808.

Storey, M., R. A. Duncan, and C. Tegner (2007), Timing and duration of volcanism in the North Atlantic Igneous Province: Implications for geodynamics and links to the Iceland hotspot, *Chem. Geol.*, 241(3-4), 264–281, doi: 10.1016/j.chemgeo.2007.01.016.

Torsvik, T. H. and L. R. M. Cocks (2017), *Earth History and Paleogeography*. Cambridge Univ. Press, Cambridge, U. K.

Torsvik, T. H., J. Mosar, and E. A. Eide (2001), Cretaceous-Tertiary geodynamics: a North Atlantic exercise, *Geophys. J. Int.*, 146(3), 850–866, doi: 10.1046/j.0956-540x.2001.01511.x.

Torsvik, T. H. et al. (2015), Continental crust beneath southeast Iceland, *P. Natl. Acad. Sci. USA*, 112, E1818–E1827, doi: 10.1073/pnas.1423099112.

Torsvik, T. H., B. Steinberger, M. Gurnis, and C. Gaina (2010), Plate tectonics and net lithosphere rotation over the past 150 My, *Earth Planet. Sci. Lett.*, 291(1-4), 106–112, doi: 10.1016/j.epsl.2009.12.055.

Vink, G. E. (1984), A hotspot model for Iceland and the Vøring Plateau, *J. Geophys. Res.*, 89, 9949–9959, doi: 10.1029/JB089iB12p09949.

White, R. and D. McKenzie (1989), Magmatism at rift zones: The generation of volcanic continental margins and flood basalts, *J. Geophys. Res.*, 94, 7685–7729, doi: 10.1029/JB094iB06p07685.

Wolfe, C. J., I. T. Bjarnason, J. C. VanDecar, and S. C. Solomon (1997), Seismic structure of the Iceland mantle plume, *Nature*, 385, 245–247, doi: 10.1038/385245a0.

Yuan, X., B. Heit, S. Brune, B. Steinberger, W. Geissler, W. Jokat, and M. Weber (2017), Seismic structure of the lithosphere beneath NW Namibia: Impact of the Tristan da Cunha mantle plume, *Geochem., Geophys., Geosys.*, 18, 125–141, doi: 10.1002/2016GC006645.

4 Variable melt production rate of the Kerguelen hotspot due to long-term plume-ridge interaction

A version of this chapter has been submitted to Geophysical Research Letters as Bredow, E. and B. Steinberger (2017), Variable melt production rate of the Kerguelen hotspot due to long-term plume-ridge interaction.

Abstract

For at least 120 million years, the Kerguelen plume has distributed enormous amounts of magmatic rocks over various igneous provinces between India, Australia and Antarctica. Previous attempts to reconstruct the complex history of this plume have revealed several characteristics that are inconsistent with properties typically associated with plumes. To explore the geodynamic behavior of the Kerguelen hotspot, and in particular address these inconsistencies, we set up a regional viscous flow model with the mantle convection code ASPECT. Our model features complex time-dependent boundary conditions in order to explicitly simulate the surrounding conditions of the Kerguelen plume. We show that a constant plume influx can result in a variable magma production rate if the plume interacts with nearby spreading ridges and that a dismembered plume, multiple plumes, or solitary waves in the plume conduit are not required to explain the fluctuating magma output and other unusual characteristics attributed to the Kerguelen hotspot.

4.1 Introduction

The basaltic rocks produced by the Kerguelen mantle plume record at least 120 Ma of persistent volcanic activities and yield altogether an estimated volume of approximately $2.5 \times 10^7\,\mathrm{km}^3$ (Coffin et al., 2002). These tremendous amounts include the Kerguelen Plateau in the southern Indian Ocean, which is the second largest oceanic plateau worldwide (Coffin and Eldholm, 1994) and the Ninetyeast Ridge, extended almost parallel to the 90th meridian east over a length of more than 5000 km and thus the longest linear tectonic feature on Earth (Mahoney et al., 1983; Duncan and Richards, 1991) (Figure 4.1). Reconstructing the long-term geodynamic history of the Kerguelen hotspot is however not as straightforward as assigning the Kerguelen Plateau to the classically expected giant eruptions of an impacting plume head and the Ninetyeast Ridge to the continuous surface expression of a stable plume tail (Richards et al., 1989).

Instead, the plume started to affect the surface of the Earth rather unconventionally with a number of small-volume magmatic provinces that were placed on the contiguous continental crust of eastern Gondwana. The earliest magmatism that recent studies have associated with the Kerguelen plume began during the Early Cretaceous in the Comei area, presently located in southeastern Tibet (145 – 130 Ma (Zhu et al., 2008; Zhu et al., 2009; Liu et al., 2015)), followed

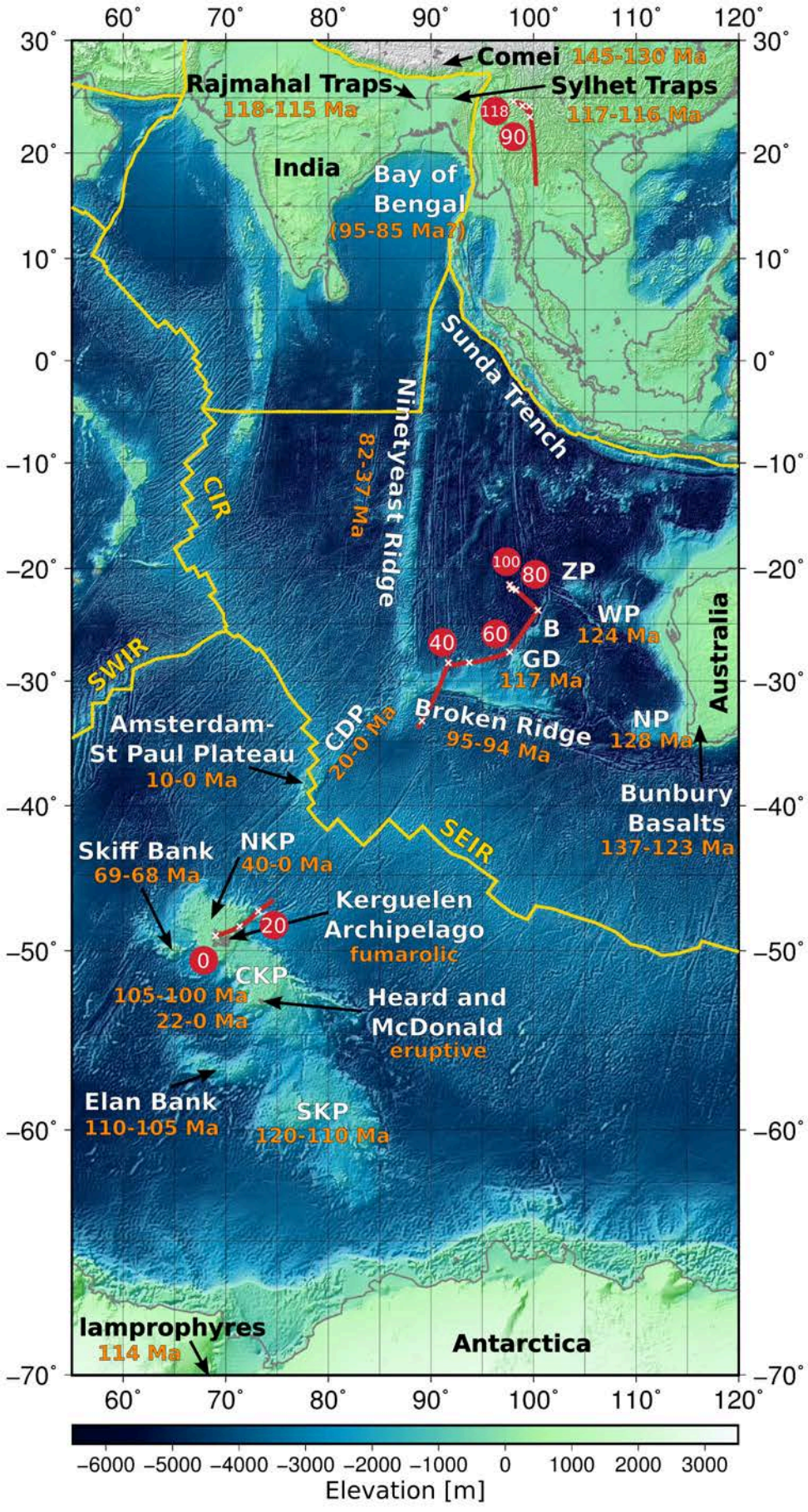
Comei 145-130 Ma
Rajmahal Traps 118-115 Ma
Sylhet Traps 117-116 Ma
India
Bay of Bengal (95-85 Ma?)
Sunda Trench
Ninetyeast Ridge 82-37 Ma
CIR
SWIR
ZP
WP 124 Ma
B
GD 117 Ma
Broken Ridge 95-94 Ma
NP 128 Ma
Australia
Amsterdam-St Paul Plateau 10-0 Ma
CDR 20-0 Ma
Bunbury Basalts 137-123 Ma
SEIR
Skiff Bank 69-68 Ma
NKP 40-0 Ma
Kerguelen Archipelago fumarolic
CKP 105-100 Ma 22-0 Ma
Heard and McDonald eruptive
Elan Bank 110-105 Ma
SKP 120-110 Ma
lamprophyres 114 Ma
Antarctica
Elevation [m]

Figure 4.1: Topographic map of the Indian Ocean and the surrounding continents showing an overview of the igneous provinces, which are mostly attributed to the Kerguelen plume. Age estimates are labeled in orange (see text for references). The red line shows the predicted hotspot track, distributed over several plates and with plume positions (in Ma); plate boundaries are shown as yellow lines. NKP, CKP, SKP - Northern, Central and Southern Kerguelen Plateau, respectively; NP, WP, ZP - Naturaliste, Wallaby and Zenith Plateau, respectively; B - Batavia Knoll; GD - Gulden Draak Knoll; SEIR, SWIR, CIR - Southeast, Southwest and Central Indian Ridge, respectively; CDP - Chain of the Dead Poets.

by several distinct eruption phases of the Bunbury Basalts in southwest Australia (between 137 and 123 Ma (Frey et al., 1996; Coffin et al., 2002; Olierook et al., 2016)).

After the continental breakup of India and Antarctica around 132 – 130 Ma (Powell et al., 1988; Gaina et al., 2007; Müller et al., 2016), the Indian Ocean started to open and dispersed continental material, in particular several microcontinents, throughout the growing ocean basin. Evidence for continental material has been found at the Naturaliste Plateau, the Wallaby Plateau, the Zenith Plateau, the Batavia Knoll and the Gulden Draak Knoll (all of which are submarine plateaus currently positioned off the west coast of Australia) (Gardner et al., 2015; Whittaker et al., 2016; Direen et al., 2017), at several parts of the Southern Kerguelen Plateau (Coffin et al., 2002) and at Elan Bank (located northwest of the Southern Kerguelen Plateau) (Frey et al., 2000; Nicolaysen et al., 2001; Weis et al., 2001; Ingle et al., 2002; Borissova et al., 2003; Gaina et al., 2003). Subsequently, large parts of these continental fragments were overlain by plume material. Age determinations of recovered igneous rocks revealed ∼130 – 125 Ma at the Naturaliste Plateau (Direen et al., 2017; Olierook et al., 2017), ∼124 Ma at the Wallaby Plateau (Olierook et al., 2015) and 117 Ma at the Gulden Draak Knoll (Whittaker et al., 2016).

The first larger volumes of volcanic material, considered as the actual Large Igneous Province (LIP) of the Kerguelen Plume, shaped the Southern Kerguelen Plateau in the growing basin of the Indian Ocean between 120 and 110 Ma (Coffin et al., 2002; Duncan, 2002). Thus, the LIP postdated the continental breakup by approximately 10 Ma, although older igneous rocks might be concealed at greater depths than penetrated by previous drilling campaigns. Parallel to the development of the Southern Kerguelen Plateau, further small-scale volcanism created the Rajmahal Traps (118 – 115 Ma (Baksi, 1995; Coffin et al., 2002; Kent et al., 2002)) and Sylhet Traps (118 – 116 Ma (Ray et al., 2005; Ghatak and Basu, 2011)) on the Indian continental margin and lamprophyre dikes on the conjugate Antarctic margin (114 Ma (Coffin et al., 2002)), whereas the Elan Bank microcontinent was capped by plume material between 110 and 105 Ma (Coffin et al., 2002; Duncan, 2002).

In contrast to the classically predicted short pulse of vigorous magmatic activity lasting only a few Myr (e.g. Coffin and Eldholm, 1994; Bryan and Ernst, 2008), the large-volume magma production of the Kerguelen plume continued for a much longer period and resulted in the formation of the Central Kerguelen Plateau between 105 and 100 Ma (Coffin et al., 2002; Duncan, 2002) and the (at that time) contiguous Broken Ridge between 100 and 95 Ma (Coffin et al., 2002; Duncan, 2002), both of which are generally also considered as part of the Kerguelen LIP.

Afterwards, the plume productivity decreased (Coffin et al., 2002) and created the Ninetyeast Ridge, probably starting around 95 Ma, although the northernmost part is currently covered

by the thick sediment load of the Bengal Fan (Coffin et al., 2002). The observable part of the Ninetyeast Ridge is explicitly age-progressive and ranges in age approximately from 82 to 37 Ma (Duncan, 1991; Coffin et al., 2002). Its clear, linear structure has been attributed to the rapid northward motion of the Indian plate over the Kerguelen plume by many previous studies (e.g. Mahoney et al., 1983; Duncan and Richards, 1991). Evidence for small-scale plume activity on the Antarctic plate in this period was found at Skiff Bank (69 – 68 Ma (Coffin et al., 2002; Duncan, 2002)).

The separation of the Kerguelen Plateau and the Broken Ridge was initiated by the onset of seafloor-spreading at the Southeast Indian Ridge around 40 Ma (Mutter and Cande, 1983; Müller et al., 2016). Simultaneously, long-term volcanism at the nearby Northern Kerguelen Plateau started (Nicolaysen et al., 2000; Coffin et al., 2002; Duncan, 2002; Weis and Frey, 2002; Doucet et al., 2002) and has continued until the present-day, as evidenced by active fumaroles at the Kerguelen Archipelago (Patrick and Smellie, 2013). The current hotspot location is however debatable, since the neighboring Central Kerguelen Plateau has also been volcanically active over the past 22 Ma (Weis et al., 2002; Duncan et al., 2016) and eruptions have recently been monitored at Heard and McDonald Island (Patrick and Smellie, 2013).

Regarding the plume history, it should be noted that the Kerguelen Plateau has been generated in three clearly distinct periods of plume activity, even though its structure appears to be continuous on topographic maps. Also split in three distinct parts is the Kerguelen hotspot track reconstructed in the Doubrovine et al. (2012) mantle reference frame (see Figure 4.1). It demonstrates that the Kerguelen plume has successively affected the Indian, Australian and Antarctic plates, and even simultaneously at times when the plume was close enough to interact with a spreading ridge. The long-term proximity and interaction of the Kerguelen plume and the plate boundaries in the Indian Ocean has been validated by the plate tectonic models of Whittaker et al. (2013) and Whittaker et al. (2015).

Another region relevant to the Kerguelen plume history is the volcanically active Amsterdam-Saint Paul Plateau (Johnson et al., 2000), which is located ∼1400 km northeast of the Kerguelen Archipelago and situated directly on the axis of the Southeast Indian Ridge. This plateau has been created during the past 10 Myr and the Chain of the Dead Poets is regarded as its corresponding hotspot track that was formed over the past 20 Myr and trends age-progressively from the southern end of the Ninetyeast Ridge toward the Amsterdam-Saint Paul Plateau (Maia et al., 2011; Janin et al., 2011). Already Morgan (1978) suggested that this region might be fed by the Kerguelen plume through an asthenospheric flow channel, a hypothesis that was supported by the flow models of Yale and Morgan (1998). Geochemical studies have however shown that the isotopic compositions from Amsterdam and Saint Paul Island, nearby ridge segments and an active submarine volcano are (apart from being clearly distinct from each other) incompatible with the characteristics of Kerguelen plume material and therefore regard the Amsterdam-Saint Paul plume as a second, independent plume with indications of a deep source (Graham et al., 1999; Johnson et al., 2000; Doucet et al., 2004; Nicolaysen et al., 2007).

Altogether, it can be summarized that the geodynamic history of the Kerguelen plume and

its magmatic output is very complex and challenges the classical plume model (e.g. Courtillot et al., 2003) as well as other characteristics potentially linked to plumes (e.g. Coffin and Eldholm, 1992; Courtillot et al., 1999) in different ways: the first eruptions produced only small volumes of basalt; the LIP was created long after the continental breakup; when the large-volume output finally started, it continued for an unusually long period; many different distinct provinces were affected by the plume and currently, a second deeply rooted plume might be situated not too far away. Despite the remote location of most parts of this area, it was the destination of various ocean drilling expeditions and most of the abundant published studies focussed on gaining further insights for the reconstruction of the origin and evolution of the Kerguelen plume history. Our study, however, provides the first geodynamic model of the Kerguelen plume that explicitly considers its local surroundings and a realistic plate tectonic geometry over time. The results can therefore be compared to the existing age dates, the structures of the igneous provinces, and estimates of the crustal thickness and the melt production rate. Most importantly, the dynamic behavior of the model reveals new perspectives on the apparent inconsistencies with the plume characteristics listed above.

4.2 Model Setup

Following the methods described in detail in Gassmöller et al. (2016) and Bredow et al. (2017), we set up a regional viscous flow model with the mantle convection code ASPECT (Bangerth et al., 2017; Heister et al., 2017) in order to explore the geodynamic history of the Kerguelen hotspot.

The model domain is a 3300 km long, 3300 km wide and 660 km high Cartesian box that specifically simulates the surrounding conditions of the Kerguelen plume by combining various initial and time-dependent boundary conditions: reconstructed plate boundaries (interpolations of Torsvik et al. (2010)) and plate velocities are prescribed on top of the box and the uppermost 200 km of the side boundaries (based on the reference frame of Doubrovine et al. (2012)), large-scale global mantle flow velocities are prescribed at depths greater than 200 km at the side boundaries and the bottom of the box (derived from a lower resolved global convection model; an update of Doubrovine et al. (2012), whereby mantle flow in the past is computed by backward-advecting present-day density heterogeneities from the SMEAN tomography model of Becker and Boschi (2002); for more details see appendix of Gassmöller et al. (2016)) and an inhomogeneous lithosphere thickness pattern simulates the distribution of continental and oceanic lithosphere, implemented as temperature boundary conditions (backward-rotations of the global lithosphere thickness model of Steinberger (2016) for continental areas; backward-rotated ocean-floor age of Müller et al. (2008), converted to half-space cooling temperatures for oceanic areas and considering that the lithosphere cools and thickens with age).

Note that apart from the initial state of the model, these conditions are only prescribed at the boundaries of the box while the model development inside the box is completely dynamic. Thus the model is able to show how the plume may have responded over time to nearby moving

mid-ocean ridges and a variable lithosphere thickness pattern moving across the plume.

The viscosity in the model (equivalent to Bredow et al. (2017)) is temperature-dependent and depth-dependent after Steinberger and Calderwood (2006), but also takes into account a dehydration rheology to consider the sudden viscosity increase due to the extraction of water from olivine during melting. Additionally, a depletion buoyancy induces a density decrease when melt is extracted.

Melting in the model depends on temperature and pressure, following the parametrization of Katz et al. (2003) for batch melting of anhydrous peridotite. In each timestep, the generated melt is instantly extracted vertically upward to the surface and, in a postprocessing procedure, moved to the present-day location with the according plate motions. The generated melt in its entirety finally shows the Kerguelen hotspot track as predicted by the model, i.e. at which areas the plume may have produced a certain thickness of crust. To investigate the crustal thickness contribution of the plume alone, we have to correct for the melt generated along the spreading ridges from passively upwelling material, without any plume influence. Therefore our results show the difference between the model with the plume as described in this section and another model with exactly the same setup, but without a plume.

As shown in Bredow et al. (2017), our model setup is not designed to handle melting in continental environments with high lithosphere thickness values (such as Eastern Gondwana before ∼132 Ma). It also remains somewhat enigmatic what prevented the Kerguelen plume, if it already ponded underneath Eastern Gondwana and produced the small-volume igneous provinces described above, from vigorous volcanic activities as soon as the Indian ocean basin started to open and placed thin oceanic lithosphere above the plume. In this case, the Southern Kerguelen Plateau would have been created contiguously with the Antarctic continental margin, as already noted by Müller et al. (1993). Therefore, our model does not start until 120 Ma, and the plume head enters the model at that time with an excess temperature $\Delta T_{head} = 300\,\mathrm{K}$, radius $R_{head} = 250\,\mathrm{km}$ and a vertical inflow velocity $v_{head} = 20\,\mathrm{cm/yr}$, corresponding to Bredow et al. (2017), such that the spatial extent of the melting region agrees approximately with the surface area of the Southern and Central Kerguelen Plateau. Thus, first plume-derived melts are generated at 118.75 Ma, in agreement with the onset of melting at the Southern Kerguelen Plateau (circa 120 – 110 Ma (Coffin et al., 2002; Duncan, 2002)) and the Rajmahal Traps (118 – 115 Ma (Baksi, 1995; Coffin et al., 2002; Kent et al., 2002)) and Sylhet Traps (118 – 116 Ma (Ray et al., 2005; Ghatak and Basu, 2011)).

For the plume tail, excess temperature estimates range between 209 and 232 K (Putirka, 2008; Schilling, 1991) and buoyancy flux estimates range between 200 and 2070 kg/s (Davies, 1988; Sleep, 1990; Schilling, 1991; Turcotte and Schubert, 2002). In our model, $\Delta T_{tail} = 250\,\mathrm{K}$, $R_{tail} = 140\,\mathrm{km}$ and $v_{tail} = 6$ cm/yr. The prescribed excess temperature is higher than the published values, because it decreases during its ascent from the bottom of the box to the melting area, where it arrives with an excess temperature within the estimated range. The buoyancy flux of the plume at the bottom of the box yields approximately 1150 kg/s, in the midst of the range of published estimates. We use a plume inflow position that is fixed in the

Global Moving Hotspot Reference Frame of Doubrovine et al. (2012) underneath the present location of the Kerguelen Archipelago, because Steinberger (2000) reported the best fit for a fixed plume. Note that since Kerguelen was not one of the plumes used to devise the Doubrovine et al. (2012) frame, assuming a fixed plume is not self-contradictory. To prevent any net mass influx or outflux of the model domain and especially balance the plume inflow, each model runs a second time with velocity boundary conditions that are corrected with the net mass flux derived from the first model run (see Gassmöller et al. (2016) for details).

4.3 Results

The model results are visualized in Figure 4.2: the large map on the right shows the entire crustal thickness pattern produced by the modeled plume to be compared to the topographic structures. To identify when each part of the hotspot track was created, the total result has been split into partial results for 10 Myr intervals, plotted on the smaller topographic maps. The evolution of the plume and its interaction with nearby spreading ridges can be followed along the interval maps and the inset figures, showing top views of the model at the respective times.

At 115 Ma, the plume head has reached the surface underneath the nascent Indian Ocean between India and Antarctica. The thin oceanic lithosphere and the dimension of the plume head enable extensive melting both on the Antarctic and the Indian plates and this results in the formation of the Southern Kerguelen Plateau, although shifted to the east in comparison to the present-day topography, and the Rajmahal and Sylhet Traps, shifted to the southeast (see black arrows). Some melt is also generated close to the Naturaliste, Wallaby and Zenith Plateaus, but not on the Gulden Draak Knoll (117 Ma) and there is no melt at all close to the lamprophyres at Antarctica (114 Ma). The timing for the origin of the Rajmahal Traps (118 – 115 Ma) and Sylhet Traps (118 – 116 Ma) and the Southern Kerguelen Plateau (120 – 110 Ma), however, is exactly reproduced in the model, due to the chosen initiation time of the modeled plume (see section 4.1 for age references).

Between 110 and 100 Ma, most of the crust is produced at the fast moving Antarctic plate, creating the Central Kerguelen Plateau in agreement with age dates (105 – 100 Ma), whereas only little crust is produced at Elan Bank (110 – 105 Ma). Around 105 Ma, the plume interacts with the triple junction between the Indian, Australian and Antarctic plates, thus generating crust at three different plates at the same time.

At 95 Ma, the plume is mostly situated underneath the Australian plate and creates the Broken Ridge (95 – 94 Ma), matching age dates very well. Subsequently, the Indian plate accelerates to its record velocities before the collision with the Eurasian plate and plume material gets captured by the ridge between India and Australia. This marks the onset of long-term decompression melting along the ridge that generates the Ninetyeast Ridge (82 – 37 Ma), including the part presumably covered underneath the Bengal Fan (95 – 85 Ma). This is a surprising and novel result, because many previous studies (e.g. Duncan, 1991; Duncan and Richards, 1991) agreed that the Ninetyeast Ridge results from the Indian plate moving above the Kerguelen plume –

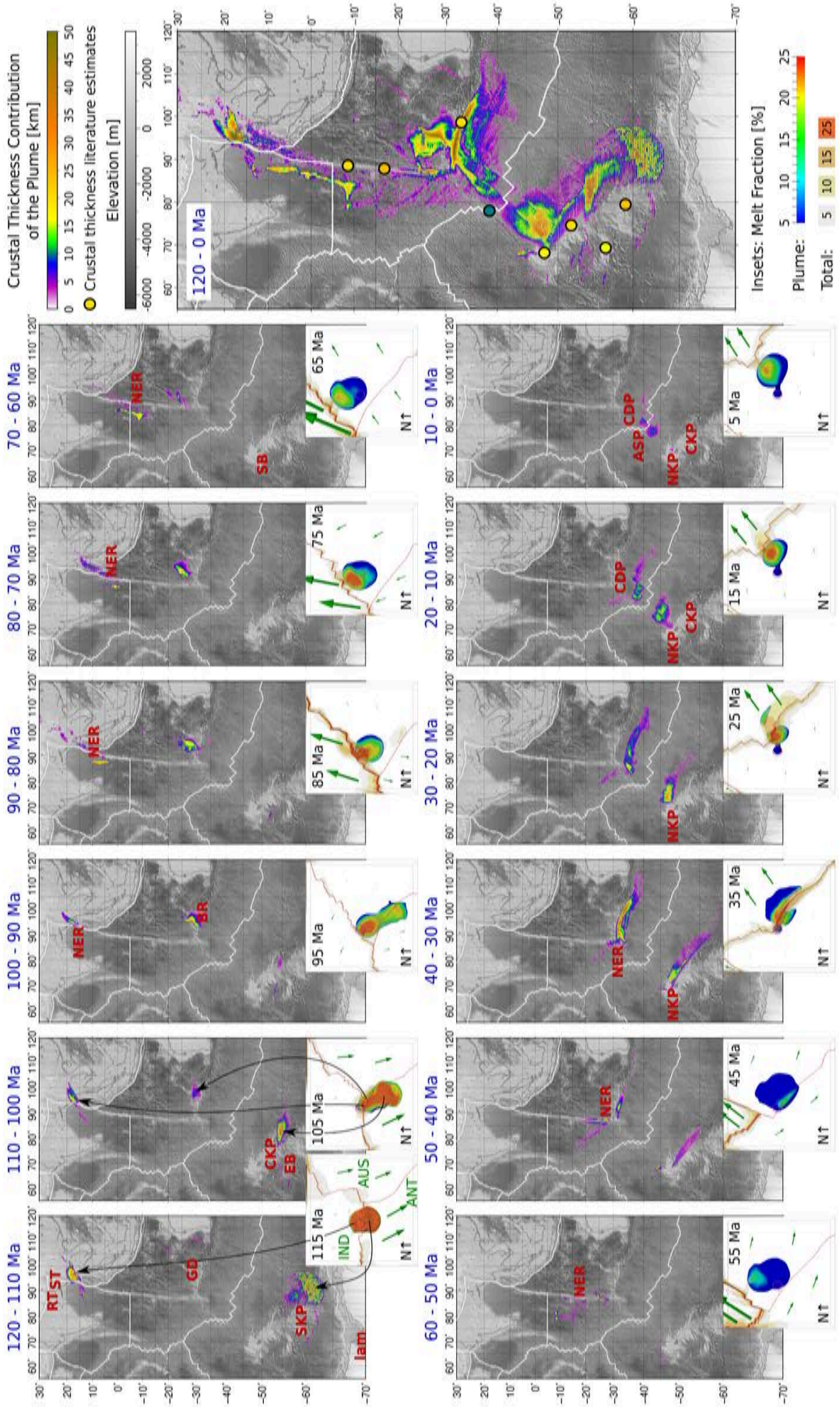
Crustal Thickness Contribution of the Plume [km]
0 5 10 15 20 25 30 35 40 45 50
Crustal thickness literature estimates
Elevation [m]
-6000 -4000 -2000 0 2000
120 - 0 Ma
Insets: Melt Fraction [%]
Plume: 5 10 15 25
Total: 5 10 15 25
120 - 110 Ma
110 - 100 Ma
100 - 90 Ma
90 - 80 Ma
80 - 70 Ma
70 - 60 Ma
60 - 50 Ma
50 - 40 Ma
40 - 30 Ma
30 - 20 Ma
20 - 10 Ma
10 - 0 Ma
RT
ST
GD
SKP
Iam
NER
BR
SB
CKP
EB
AUS
IND
ANT
CDP
ASP
NKP
115 Ma
105 Ma
95 Ma
85 Ma
75 Ma
65 Ma
55 Ma
45 Ma
35 Ma
25 Ma
15 Ma
5 Ma
N↑

Figure 4.2: Large map: crustal thickness pattern predicted by the modeled plume over the past 120 Ma, where color-coded circles correspond to literature estimates. Smaller maps: predicted crustal thickness pattern divided into 10 Myr intervals, plotted with present-day plate boundaries and red labels indicating approximately the areas in which igneous material was created during this interval (for abbreviations, see Figure 4.1). Insets show top views of the model in the middle of each respective time interval, where plate boundaries (in red) correspond to the respective time. The plume is visualized by the 100 K excess temperature isocontour and colored according to the melt fraction. Isocontours show total melt fractions above 5% in the entire model domain. Green arrows depict the plate velocities and the pink circles indicate the position of the plume stem at the bottom of the model box (apparent shift due to 3D view from vertically above the center of the model, not vertically above the plume).

yet in our model, the plume is located underneath the Australian plate between 95 and 45 Ma and the Ninetyeast Ridge is clearly produced on the ridge axis and not directly above the plume.

The opening of the Southeast Indian Ridge at 40 Ma results in a period of intensive on-ridge volcanism that starts to form the Northern Kerguelen Plateau at the Antarctic plate around 40 Ma, matching age dates excellently. The large-scale structure on the conjugate Australian plate resembles the Broken Ridge very well, but it is much younger than indicated by oceanic drilling (95 – 94 Ma).

Approaching the present-day model state, there is no crust generated at the Central Kerguelen Plateau, but on the Northern Kerguelen Plateau melting occurs close to the Kerguelen Archipelago. Another interesting result concerns the Amsterdam-Saint Paul Plateau: in agreement with age dates, crust is generated close to the Chain of the Dead Poets over the past 20 Ma and currently, the model predicts crustal material also close to the Ridge, in vicinity of the Amsterdam-Saint Paul Plateau. The inset map reveals that the plume has a circular shape at 5 Ma, which means that it is no longer captured by the ridge and intraplate volcanism creates the melt at the Kerguelen Plateau. However, there is still a flow connection which transports plume material toward the ridge (in agreement with Morgan (1978) and Yale and Morgan (1998)) and the crust close to the Amsterdam-Saint Paul Plateau is the product of on-ridge volcanism. Even though geochemical studies conclude differently, our model provides a simple yet elegant explanation for the observed volcanic structures without the need for a second plume.

All in all, the crustal thickness pattern predicted by the model over the past 120 Ma (large map on the right in Figure 4.2) resembles the topographic structures associated with Kerguelen plume activities remarkably well. The Ninetyeast Ridge, although shifted to the west and not entirely continuous (due to the decreasing amount of spreading segments at the Indian-Australian plate boundary, where most melt is generated), is clearly recognisable, as well as the Broken Ridge. The Kerguelen Plateau is predicted to result explicitly from three distinct periods of volcanism, although shifted to the east in the model relative to its true location. Apart from several small-scale areas, where the model reaches maximum crustal thickness values of about 45 km, the model result approximately fits the range of literature values from seismic refraction and reflection studies, wide-angle seismic data, gravity, bathymetry and isostasy analyses (marked by color-coded filled circles on the map): 21 – 25 km at the Southern Kerguelen Plateau (Operto and Charvis, 1995, 1996), 19 – 21 km at the Central Kerguelen Plateau (Charvis et al., 1995), at least 16 km at Elan Bank (Borissova et al., 2003), circa 22 – 24 km at the Ninetyeast Ridge

(Grevemeyer et al., 2001; Krishna et al., 2001), 18 – 22 km at the Broken Ridge (Francis and Raitt, 1967), 15 – 21 km at the Northern Kerguelen Plateau and Archipelago (Charvis et al., 1995; Recq et al., 1990) and 10 km on average at the Amsterdam-Saint Paul Plateau (Scheirer et al., 2000). It must however be considered that a direct comparison is not entirely accurate, since the modeled crustal thickness is only accumulated by plume activities, whereas the contribution of melting along the spreading ridges is removed from the model result.

Based on radiometric age determinations and crustal structure volume estimates, Coffin et al. (2002) calculated the magmatic output rate of the Kerguelen plume over time and concluded that the melt production rate has been substantially variable (see Figure 4.3a), with a discontinuous 25 Myr peak magma output. To account for these results, Coffin et al. (2002) suggested the involvement of multiple plumes or one plume split into several diapirs by vigorous mantle shear flow. Based on numerical models of thermal plumes, Lin and van Keken (2005) demonstrated that the entrainment of dense material in the lowermost mantle can lead to multiple pulses of plume material and thus be another explanation for several volcanic episodes generating flood basalts. Sreejith and Krishna (2015) reported a rapidly varying magma production rate along the Ninetyeast Ridge (see Figure 4.3a) and attributed the long-term variations to the frequent ridge jumps and major velocity changes of the Indian plate, whereas short-term variations were explained by solitary waves in the plume tail. Referring to these results, Figure 4.3b shows the magma production rate in the model, derived both for the 10 Ma intervals as shown in Figure 4.2 and also for 1 Ma intervals in order to visualize the short-term variations. Note that due to an applied smoothing algorithm, the 1 Ma intervals underestimate the magma flux by ∼8 %. The peak produced by the impact of the plume head reaches 0.9 km^3/yr, matching the rate estimated by Coffin et al. (2002), but it lasts only for a few Myr in agreement with the classical plume model. Subsequently, the magma flux fluctuates significantly, and reaches a second peak after the onset of spreading at the South East Indian Ridge at 40 Ma. Our model does not reach the values of Sreejith and Krishna (2015) during the creation of the Ninetyeast Ridge, but the total magma production of our model yields a volume of 1.98×10^7 km^3, comparable to the 2.5×10^7 km^3 given by Coffin et al. (2002). The reason for the fluctuations can best be seen by comparing the colors of the plume in the insets in Figure 4.2, which correspond to the degree of melting in the model. Even though the plume tail influx at the bottom of the model is constant, the melt production rate changes significantly over time, mainly influenced by the distance to mid-ocean ridges (which determines the thickness of the lithosphere the plume material impinges on), as well as the directions and velocities of nearby plate motions. Since all these influencing factors, in short, plume-ridge interaction, change considerably over time, the variable melt production rate is rather the direct consequence of a very dynamic long-term plume history than an indication of highly complicated plume properties – the main result of this study.

Concerning the parameters chosen for the model, a variation of the plume parameters mainly changes the width of the resulting hotspot track and thus the amount of produced crust (see Bredow et al. (2017) for an extensive parameter study). A variation that we tested for the

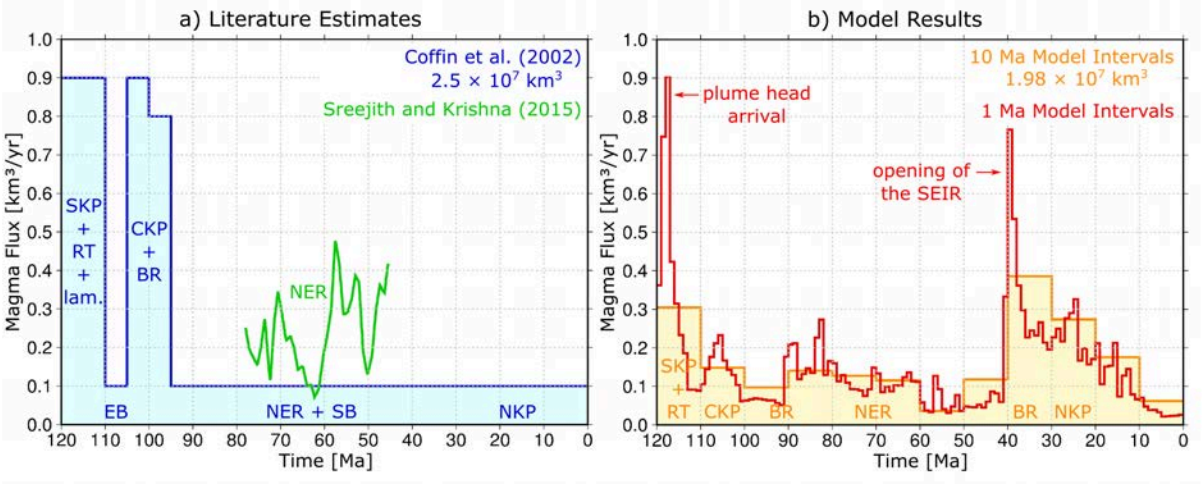

Figure 4.3: Variations in the melt production rate of the Kerguelen plume (a) as estimated by previous studies and (b) predicted by the model. All rates refer only to the excess of the normal oceanic crustal production. For abbreviations, see Figure 4.1.

Kerguelen plume model was to fix the plume underneath Heard Island instead of the Kerguelen Archipelago, referring to the recent eruptions at Heard and McDonald Island. As a result, all parts of the Kerguelen Plateau and the Broken Ridge appear too far southeast and at the present-day state, crust is neither produced at the Central, nor at the Northern Kerguelen Plateau, likely due to the relatively thick lithosphere. We have not considered a southward motion of the plume as inferred by O'Neill et al. (2003) or Antretter et al. (2002), nor any other hotspot motion – although it might be used to improve the agreement between predicted hotspot track and topography, since a likely explanation for the deviations is that the plume did not stay fixed below the Kerguelen Archipelago, as assumed in our model. Given the major role of the plate motions and plate boundaries, we also used the plate reconstruction of Matthews et al. (2016), based on Domeier and Torsvik (2014) and Müller et al. (2016) for the boundary conditions as an alternative to the results presented in the figures. As a result, the Ninetyeast Ridge loses its linear structure, the Southern Kerguelen Plateau is only a very small province, disconnected with the rest of the Plateau and the overall pattern resembles the topographic structures less than in our reference model.

Returning to the unusual plume characteristics described in section 4.1, the model can neither explain why the oldest continental igneous provinces have very small volumes, nor why the LIP significantly postdated the continental breakup. However, we show that the large-volume output does not have to continue for an uncommonly long period in order to create the observable topography structures. Furthermore, our model demonstrates that a single, not unusually buoyant or hot plume can cause the variety of widespread basaltic provinces attributed to Kerguelen plume activities as well as the current eruption sites at the Amsterdam-Saint Paul Plateau.

4.4 Conclusions

Our three-dimensional regional convection model of the Kerguelen mantle plume predicts the amount and distribution of plume-generated crust over the past 120 Ma. We compare the result to present-day topographic structures to gain insights into the geodynamic processes involved in the history of the plume, which leads to the following conclusions:

1. A constant plume influx can result in a significantly variable magma production rate due to the interaction of the plume with nearby mid-ocean ridges and plate motions.

2. The model indicates that the Ninetyeast Ridge was created by volcanism along the ridge axis between the Indian and Australian plate, while the Kerguelen plume was located further away underneath the Australian plate. This differs with previous studies that described the Ninetyeast Ridge as the result of the Indian plate moving above the plume.

3. In a dynamic sense, the model suggests that the Amsterdam-Saint Paul Plateau is generated by volcanic material that flows from the plume conduit toward the axis of the Southeast Indian Ridge and leads to on-ridge eruptions, whereas the volcanic activities at the Kerguelen Plateau can be attributed to intraplate volcanism, directly above the plume.

Acknowledgments

This project is funded by the Deutsche Forschungsgemeinschaft (DFG) under grant STE 907/11-1 to B.S. and the computational resources were provided by the North-German Supercomputing Alliance (HLRN) as part of project bbp00006. The geodynamic models were computed with the open-source software ASPECT (*https://aspect.geodynamics.org/*) and the necessary data to reproduce the models are provided upon request. We thank Anneke Veting for helping to prepare the plate reconstructions used as boundary conditions, Simon Williams for inspiration at the right time and Juliane Dannberg for helpful comments on the manuscript. We also thank Garrett Ito and an anonymous reviewer for constructive comments on the paper.

References

Antretter, M., B. Steinberger, F. Heider, and H. Soffel (2002), Paleolatitudes of the Kerguelen hotspot: new paleomagnetic results and dynamic modeling, *Earth Planet. Sci. Lett.*, 203(2), 635–650, doi: 10.1016/S0012-821X(02)00841-5.

Baksi, A. K. (1995), Petrogenesis and timing of volcanism in the Rajmahal flood basalt province, northeastern India, *Chemical Geology*, 121(1), 73–90, doi: 10.1016/0009-2541(94)00124-Q.

Bangerth, W., J. Dannberg, R. Gassmöller, T. Heister, et al. (2017), *ASPECT: Advanced Solver for Problems in Earth's ConvecTion, User Manual,* doi: 10.6084/m9.figshare.4865333.

Becker, T. W. and L. Boschi (2002), A comparison of tomographic and geodynamic mantle models, *Geochem., Geophys., Geosys.*, 3, 1003, doi: 10.1029/2001GC000168.

Borissova, I., M. F. Coffin, P. Charvis, and S. Operto (2003), Structure and development of a microcontinent: Elan Bank in the southern Indian Ocean, *Geochem. Geophys. Geosyst.*, 4(9). doi: 10.1029/2003GC000535.

Bredow, E., B. Steinberger, R. Gassmöller, and J. Dannberg (2017), How plume-ridge interaction shapes the crustal thickness pattern of the Réunion hotspot track, *Geochem. Geophys. Geosyst.*, 18(8), 2930–2948, doi: 10.1002/2017GC006875.

Bryan, S. E. and R. E. Ernst (2008), Revised definition of Large Igneous Provinces (LIPs), *Earth-Science Reviews*, 86(1), 175–202, doi: 10.1016/j.earscirev.2007.08.008.

Charvis, P., M. Recq, S. Operto, and D. Brefort (1995), Deep structure of the northern Kerguelen Plateau and hotspot-related activity, *Geophys. J. Int.*, 122(3), 899–924, doi: 10.1111/j.1365-246X.1995.tb06845.x.

Coffin, M. F. and O. Eldholm (1992), Volcanism and continental break-up: a global compilation of large igneous provinces, *Geological Society, London, Special Publications*, 68(1), 17–30, doi: 10.1144/GSL.SP.1992.068.01.02.

Coffin, M. F. and O. Eldholm (1994), Large igneous provinces: Crustal structure, dimensions, and external consequences, *Rev. Geophys.*, 32(1), 1–36, doi: 10.1029/93RG02508.

Coffin, M. F., M. Pringle, R. Duncan, T. Gladczenko, M Storey, R. Müller, and L. Gahagan (2002), Kerguelen Hotspot Magma Output since 130 Ma, *Journal of Petrology*, 43(7), 1121–1137, doi: 10.1093/petrology/43.7.1121.

Courtillot, V., C. Jaupart, I. Manighetti, P. Tapponnier, and J. Besse (1999), On causal links between flood basalts and continental breakup, *Earth Planet. Sci. Lett.*, 166(3), 177 –195, doi: 10.1016/S0012-821X(98)00282-9.

Courtillot, V., A. Davaille, J. Besse, and J. Stock (2003), Three distinct types of hotspots in the Earth's mantle, *Earth Planet. Sci. Lett.*, 205(3-4), 295–308, doi: 10.1016/S0012-821X(02)01048-8.

Davies, G. F. (1988), Ocean bathymetry and mantle convection: 1. Large-scale flow and hotspots, *J. Geophys. Res.*, 93, (B9), 104,67–10,480, doi: 10.1029/JB093iB09p10467.

Direen, N. G., B. E. Cohen, R. Maas, F. A. Frey, J. M. Whittaker, M. F. Coffin, S. Meffre, J. A. Halpin, and A. J. Crawford (2017), Naturaliste Plateau: constraints on the timing and evolution of the Kerguelen Large Igneous Province and its role in Gondwana breakup, *Australian Journal of Earth Sciences*, 64(7), 851–869, doi: 10.1080/08120099.2017.1367326.

Domeier, M. and T. H. Torsvik (2014), Plate tectonics in the late Paleozoic, *Geoscience Frontiers*, 5(3), 303–350, doi: 10.1016/j.gsf.2014.01.002.

Doubrovine, P. V., B. Steinberger, and T. H. Torsvik (2012), Absolute plate motions in a reference frame defined by moving hot spots in the Pacific, Atlantic, and Indian oceans, *J. Geophys. Res.*, 117, B09101, doi: 10.1029/2011JB009072.

Doucet, S., D. Weis, J. S. Scoates, K. Nicolaysen, F. A. Frey, and A. Giret (2002), The Depleted Mantle Component in Kerguelen Archipelago Basalts: Petrogenesis of Tholeiitic-Transitional

Basalts From the Loranchet Peninsula, *Journal of Petrology*, 43(7), 1341–1366, doi: 10.1093/petrology/43.7.1341.

Doucet, S., D. Weis, J. S. Scoates, V. Debaille, and A. Giret (2004), Geochemical and Hf-Pb-Sr-Nd isotopic constraints on the origin of the Amsterdam-St. Paul (Indian Ocean) hotspot basalts, *Earth Planet. Sci. Lett.*, 218(1-2), 179–195, doi: 10.1016/S0012-821X(03)00636-8.

Duncan, R. A. (1991), Age distribution of volcanism along aseismic ridges in the eastern Indian Ocean, *Proceedings of the Ocean Drilling Program, Scientific Results*, 121, 507–517, doi: 10.2973/odp.proc.sr.121.162.1991.

Duncan, R. A. (2002), A Time Frame for Construction of the Kerguelen Plateau and Broken Ridge, *Journal of Petrology*, 43(7), 1109–1119, doi: 10.1093/petrology/43.7.1109.

Duncan, R. A. and M. A. Richards (1991), Hotspots, mantle plumes, flood basalts, and true polar wander, *Reviews of Geophysics*, 29(1), 31–50, doi: 10.1029/90RG02372.

Duncan, R. A., T. J. Falloon, P. G. Quilty, and M. F. Coffin (2016), Widespread Neogene volcanism on Central Kerguelen Plateau, Southern Indian Ocean, *Australian Journal of Earth Sciences*, 63(4), 379–392, doi: 10.1080/08120099.2016.1221857.

Francis, T. J. G. and R. W. Raitt (1967), Seismic refraction measurements in the southern Indian Ocean, *J. Geophys. Res.*, 72(12), 3015–3041, doi: 10.1029/JZ072i012p03015.

Frey, F. et al. (2000), Origin and evolution of a submarine large igneous province: the Kerguelen Plateau and Broken Ridge, southern Indian Ocean, *Earth Planet. Sci. Lett.*, 176(1), 73 –89, doi: 10.1016/S0012-821X(99)00315-5.

Frey, F. A., N. J. McNaughton, D. R. Nelson, J. R. deLaeter, and R. A. Duncan (1996), Petrogenesis of the Bunbury Basalt, Western Australia: interaction between the Kerguelen plume and Gondwana lithosphere?, *Earth Planet. Sci. Lett.*, 144(1), 163–183, doi: 10.1016/0012-821X(96)00150-1.

Gaina, C., R. D. Müller, B. J. Brown, and T. Ishihara (2003), Microcontinent formation around Australia, *Spec. Pap. Geol. Soc. Am.*, 372, 405–416, doi: 10.1130/0-8137-2372-8.405.

Gaina, C., R. D. Müller, B. Brown, T. Ishihara, and S. Ivanov (2007), Breakup and early seafloor spreading between India and Antarctica, *Geophys. J. Int.*, 170(1), 151–169, doi: 10.1111/j.1365-246X.2007.03450.x.

Gardner, R. L., N. R. Daczko, J. A. Halpin, and J. M. Whittaker (2015), Discovery of a microcontinent (Gulden Draak Knoll) offshore Western Australia: Implications for East Gondwana reconstructions, *Gondwana Research*, 28(3), 1019–1031, doi: 10.1016/j.gr.2014.08.013.

Gassmöller, R., J. Dannberg, E. Bredow, B. Steinberger, and T. H. Torsvik (2016), Major influence of plume-ridge interaction, lithosphere thickness variations, and global mantle flow on hotspot volcanism – The example of Tristan, *Geochem. Geophys. Geosyst.*, 17, 1454–1479, doi: 10.1002/2015GC006177.

Ghatak, A. and A. R. Basu (2011), Vestiges of the Kerguelen plume in the Sylhet Traps, northeastern India, *Earth Planet. Sci. Lett.*, 308(1), 52–64, doi: 10.1016/j.epsl.2011.05.023.

Graham, D. W., K. T. M. Johnson, L. D. Priebe, and J. E. Lupton (1999), Hotspot-ridge interaction along the Southeast Indian Ridge near Amsterdam and St. Paul islands: helium

isotope evidence, *Earth Planet. Sci. Lett.*, 167(3-4), 297–310, doi: 10.1016/S0012-821X(99)00030-8.

Grevemeyer, I., E. R. Flueh, C. Reichert, J. Bialas, D. Kläschen, and C. Kopp (2001), Crustal architecture and deep structure of the Ninetyeast Ridge hotspot trail from active-source ocean bottom seismology, *Geophys. J. Int.*, 144(2), 414–431, doi: 10.1046/j.0956-540X.2000.01334.x.

Heister, T., J. Dannberg, R. Gassmöller, and W. Bangerth (2017), High Accuracy Mantle Convection Simulation through Modern Numerical Methods. II: Realistic Models and Problems, *Geophys. J. Int.*, 210(2), 833–851, doi: 10.1093/gji/ggx195.

Ingle, S., D. Weis, and F. A. Frey (2002), Indian Continental Crust Recovered from Elan Bank, Kerguelen Plateau (ODP Leg 183, Site 1137), *Journal of Petrology*, 43(7), 1241–1257, doi: 10.1093/petrology/43.7.1241.

Janin, M., C. Hémond, H. Guillou, M. Maia, K. T. M. Johnson, C. Bollinger, C. Liorzou, and A. Mudholkar (2011), Hot spot activity and tectonic settings near Amsterdam-St. Paul plateau (Indian Ocean), *J. Geophys. Res.*, 116(B5). B05206, doi: 10.1029/2010JB007800.

Johnson, K. T. M., D. W. Graham, K. H. Rubin, K. Nicolaysen, D. S. Scheirer, D. W. Forsyth, E. T. Baker, and L. M. Douglas-Priebe (2000), Boomerang Seamount: the active expression of the Amsterdam-St. Paul hotspot, Southeast Indian Ridge, *Earth Planet. Sci. Lett.*, 183(1-2), 245–259, doi: 10.1016/S0012-821X(00)00279-X.

Katz, R. F., M. Spiegelman, and C. H. Langmuir (2003), A new parameterization of hydrous mantle melting, *Geochem. Geophys. Geosyst.*, 4(9), 1073, doi: 10.1029/2002GC000433.

Kent, R. W., M. S. Pringle, R. D. Müller, A. D. Saunders, and N. C. Ghose (2002), 40Ar/39Ar Geochronology of the Rajmahal Basalts, India, and their Relationship to the Kerguelen Plateau, *Journal of Petrology*, 43(7), 1141–1153, doi: 10.1093/petrology/43.7.1141.

Krishna, K. S., Y. P. Neprochnov, D. G. Rao, and B. N. Grinko (2001), Crustal structure and tectonics of the Ninetyeast Ridge from seismic and gravity studies, *Tectonics*, 20(3), 416–433, doi: 10.1029/2001TC900004.

Lin, S.-C. and P. E. van Keken (2005), Multiple volcanic episodes of flood basalts caused by thermochemical mantle plumes, *Nature*, 436(7048), 250–252, doi: 10.1038/nature03697.

Liu, Z., Q. Zhou, Y. Lai, C. Qing, Y. Li, J. Wu, and X. Xia (2015), Petrogenesis of the Early Cretaceous Laguila bimodal intrusive rocks from the Tethyan Himalaya: Implications for the break-up of Eastern Gondwana, *Lithos*, 236-237, 190–202, doi: 10.1016/j.lithos.2015.09.006.

Mahoney, J., J. Macdougall, G. Lugmair, and K. Gopalan (1983), Kerguelen hotspot source for Rajmahal Traps and Ninetyeast Ridge?, *Nature*, 303, 385–389, doi: doi:10.1038/303385a0.

Maia, M. et al. (2011), Building of the Amsterdam-Saint Paul plateau: A 10 Myr history of a ridge-hot spot interaction and variations in the strength of the hot spot source, *J. Geophys. Res.*, 116(B9). B09104, doi: 10.1029/2010JB007768.

Matthews, K. J., K. T. Maloney, S. Zahirovic, S. E. Williams, M. Seton, and R. D. Müller (2016), Global plate boundary evolution and kinematics since the late Paleozoic, *Global and Planetary Change*, 146, 226–250, doi: 10.1016/j.gloplacha.2016.10.002.

Morgan, W. J. (1978), Rodriguez, Darwin, Amsterdam, ..., A second type of Hotspot Island, *J. Geophys. Res.*, 83(B11), 5355–5360, doi: 10.1029/JB083iB11p05355.

Müller, R. D., J.-Y. Royer, and L. A. Lawver (1993), Revised plate motions relative to the hotspots from combined Atlantic and Indian Ocean hotspot tracks, *Geology*, 21(3), 275–278, doi: 10.1130/0091-7613(1993)021⟨0275:RPMRTT⟩2.3.CO;2.

Müller, R. D., M. Sdrolias, C. Gaina, and W. R. Roest (2008), Age, spreading rates, and spreading asymmetry of the world's ocean crust, *Geochem. Geophys. Geosyst.*, 9, Q04006, doi: 10.1029/2007GC001743.

Müller, R. D. et al. (2016), Ocean Basin Evolution and Global-Scale Plate Reorganization Events Since Pangea Breakup, *Annu. Rev. Earth Planet. Sci.*, 44, 107–138, doi: 10.1146/annurev-earth-060115-012211.

Mutter, J. C. and S. C. Cande (1983), The early opening between Broken Ridge and Kerguelen Plateau, *Earth Planet. Sci. Lett.*, 65(2), 369–376, doi: 10.1016/0012-821X(83)90174-7.

Nicolaysen, K., F. Frey, K. Hodges, D. Weis, and A. Giret (2000), 40Ar/39Ar geochronology of flood basalts from the Kerguelen Archipelago, southern Indian Ocean: implications for Cenozoic eruption rates of the Kerguelen plume, *Earth Planet. Sci. Lett.*, 174(3-4), 313–328, doi: 10.1016/S0012-821X(99)00271-X.

Nicolaysen, K. P., F. A. Frey, J. J. Mahoney, K. T. M. Johnson, and D. W. Graham (2007), Influence of the Amsterdam/St. Paul hot spot along the Southeast Indian Ridge between 77° and 88°E: Correlations of Sr, Nd, Pb, and He isotopic variations with ridge segmentation, *Geochem. Geophys. Geosyst.*, 8(9). Q09007, doi: 10.1029/2006GC001540.

Nicolaysen, K., S. Bowring, F. Frey, D. Weis, S. Ingle, M. S. Pringle, and M. F. Coffin (2001), Provenance of Proterozoic garnet-biotite gneiss recovered from Elan Bank, Kerguelen Plateau, southern Indian Ocean, *Geology*, 29(3), 235–238, doi: 10.1130/0091-7613(2001)029⟨0235:POPGBG⟩2.0.CO;2.

Olierook, H. K. H., R. E. Merle, F. Jourdan, K. Sircombe, G. Fraser, N. E. Timms, G. Nelson, K. A. Dadd, L. Kellerson, and I. Borissova (2015), Age and geochemistry of magmatism on the oceanic Wallaby Plateau and implications for the opening of the Indian Ocean, *Geology*, 43(11), 971–974, doi: 10.1130/G37044.1.

Olierook, H. K. H., F. Jourdan, R. E. Merle, N. E. Timms, N. Kusznir, and J. R. Muhling (2016), Bunbury Basalt: Gondwana breakup products or earliest vestiges of the Kerguelen mantle plume?, *Earth Planet. Sci. Lett.*, 440, 20–32, doi: 10.1016/j.epsl.2016.02.008.

Olierook, H. K., R. E. Merle, and F. Jourdan (2017), Toward a Greater Kerguelen large igneous province: Evolving mantle source contributions in and around the Indian Ocean, *Lithos*, 282-283, 163–172, doi: 10.1016/j.lithos.2017.03.007.

O'Neill, C., D. Müller, and B. Steinberger (2003), Geodynamic implications of moving Indian Ocean hotspots, *Earth Planet. Sci. Lett.*, 215(1), 151–168, doi: 10.1016/S0012-821X(03)00368-6.

Operto, S. and P. Charvis (1995), Kerguelen Plateau: A volcanic passive margin fragment?, *Geology*, 23(2), 137–140, doi: 10.1130/0091-7613(1995)023⟨0137:KPAVPM⟩2.3.CO;2.

Operto, S. and P. Charvis (1996), Deep structure of the southern Kerguelen Plateau (southern Indian Ocean) from ocean bottom seismometer wide-angle seismic data, *J. Geophys. Res.*, 101(B11), 25077–25103, doi: 10.1029/96JB01758.

Patrick, M. R. and J. L. Smellie (2013), Synthesis: A spaceborne inventory of volcanic activity in Antarctica and southern oceans, 2000-10, *Antarctic Science*, 25(4), 475–500, doi: 10.1017/S0954102013000436.

Powell, C. M., S. R. Roots, and J. J. Veevers (1988), Pre-breakup continental extension in East Gondwanaland and the early opening of the eastern Indian Ocean, *Tectonophysics*, 155(1-4), 261–283, doi: 10.1016/0040-1951(88)90269-7.

Putirka, K. (2008), Excess temperatures at ocean islands: Implications for mantle layering and convection, *Geology*, 36(4), 283–286, doi: 10.1130/G24615A.1.

Ray, J. S., S. K. Pattanayak, and K. Pande (2005), Rapid emplacement of the Kerguelen plume-related Sylhet Traps, eastern India: Evidence from 40Ar-39Ar geochronology, *Geophys. Res. Lett.*, 32(10). doi: 10.1029/2005GL022586.

Recq, M., D. Brefort, J. Malod, and J.-L. Veinante (1990), The Kerguelen Isles (southern Indian Ocean): new results on deep structure from refraction profiles, *Tectonophysics*, 182(3-4), 227–248, doi: 10.1016/0040-1951(90)90165-5.

Richards, M. A., R. A. Duncan, and V. E. Courtillot (1989), Flood Basalts and Hot-Spot Tracks: Plume Heads and Tails, *Science*, 246, 103–107, doi: 10.1126/science.246.4926.103.

Scheirer, D. S., D. W. Forsyth, J. A. Conder, M. A. Eberle, S.-H. Hung, K. T. M. Johnson, and D. W. Graham (2000), Anomalous seafloor spreading of the Southeast Indian Ridge near the Amsterdam-St. Paul Plateau, *J. Geophys. Res.*, 105(B4), 8243–8262, doi: 10.1029/1999JB900407.

Schilling, J.-G. (1991), Fluxes and excess temperatures of mantle plumes inferred from their interaction with migrating mid-ocean ridges, *Nature*, 352, 397–403, doi: 10.1038/352397a0.

Sleep, N. H. (1990), Hotspots and mantle plumes: Some phenomenology, *J. Geophys. Res.*, 95(B5), 6715–6736, doi: 10.1029/JB095iB05p06715.

Sreejith, K. M. and K. S. Krishna (2015), Magma production rate along the Ninetyeast Ridge and its relationship to Indian plate motion and Kerguelen hot spot activity, *Geophys. Res. Lett.*, 42(4), 1105–1112, doi: 10.1002/2014GL062993.

Steinberger, B. (2000), Plumes in a convecting mantle: Models and observations for individual hotspots, *J. Geophys. Res.*, 105(B5), 11,127–11,152, doi: 10.1029/1999JB900398.

Steinberger, B. (2016), Topography caused by mantle density variations: observation-based estimates and models derived from tomography and lithosphere thickness, *Geophys. J. Int.*, 205, 604–621, doi: 10.1093/gji/ggw040.

Steinberger, B. and A. R. Calderwood (2006), Models of large-scale viscous flow in the Earth's mantle with constraints from mineral physics and surface observations, *Geophys. J. Int.*, 167(3), 1461–1481, doi: 10.1111/j.1365-246X.2006.03131.x.

Torsvik, T. H., B. Steinberger, M. Gurnis, and C. Gaina (2010), Plate tectonics and net lithosphere rotation over the past 150 My, *Earth Planet. Sci. Lett.*, 291(1-4), 106–112, doi: 10.1016/j.epsl.2009.12.055.

Turcotte, D. L. and G. Schubert (2002), *Geodynamics,* 2nd ed., Cambridge Univ. Press, Cambridge, U. K.

Weis, D. and F. A. Frey (2002), Submarine Basalts of the Northern Kerguelen Plateau: Interaction Between the Kerguelen Plume and the Southeast Indian Ridge Revealed at ODP Site 1140, *Journal of Petrology*, 43(7), 1287–1309, doi: 10.1093/petrology/43.7.1287.

Weis, D., S. Ingle, D. Damasceno, F. A. Frey, K. Nicolaysen, and J. Barling (2001), Origin of continental components in Indian Ocean basalts: Evidence from Elan Bank (Kerguelen Plateau, ODP Leg 183, Site 1137), *Geology*, 29(2), 147–150, doi: 10.1130/0091-7613(2001)029⟨0147:OOCCII⟩2.0.CO;2.

Weis, D., F. A. Frey, R. Schlich, M. Schaming, R. Montigny, D. Damasceno, N. Mattielli, K. E. Nicolaysen, and J. S. Scoates (2002), Trace of the Kerguelen mantle plume: evidence from seamounts between the Kerguelen Archipelago and Heard Island, Indian Ocean, *Geochem. Geophys. Geosyst.*, 3(6), 1–27, doi: 10.1029/2001GC000251.

Whittaker, J. M., S. E. Williams, and R. D. Müller (2013), Revised tectonic evolution of the Eastern Indian Ocean, *Geochem. Geophys. Geosyst.*, 14(6), 1891–1909, doi: 10.1002/ggge.20120.

Whittaker, J. M., J. C. Afonso, S. Masterton, R. D. Müller, P. Wessel, S. E. Williams, and M. Seton (2015), Long-term interaction between mid-ocean ridges and mantle plumes, *Nat. Geosci.*, 8, 479–483, doi: 10.1038/ngeo2437.

Whittaker, J. M., S. E. Williams, J. A. Halpin, T. J. Wild, J. D. Stilwell, F. Jourdan, and N. R. Daczko (2016), Eastern Indian Ocean microcontinent formation driven by plate motion changes, *Earth Planet. Sci. Lett.*, 454, 203–212, doi: 10.1016/j.epsl.2016.09.019.

Yale, M. M. and J. P. Morgan (1998), Asthenosphere flow model of hotspot-ridge interactions: a comparison of Iceland and Kerguelen, *Earth Planet. Sci. Lett.*, 161(1-4), 45–56, doi: 10.1016/S0012-821X(98)00136-8.

Zhu, D.-C., S.-L. Chung, X.-X. Mo, Z.-D. Zhao, Y. Niu, B. Song, and Y.-H. Yang (2009), The 132 Ma Comei-Bunbury large igneous province: Remnants identified in present-day southeastern Tibet and southwestern Australia, *Geology*, 37(7), 583–586, doi: 10.1130/G30001A.1.

Zhu, D., X. Mo, G. Pan, Z. Zhao, G. Dong, Y. Shi, Z. Liao, L. Wang, and C. Zhou (2008), Petrogenesis of the earliest Early Cretaceous mafic rocks from the Cona area of the eastern Tethyan Himalaya in south Tibet: Interaction between the incubating Kerguelen plume and the eastern Greater India lithosphere?, *Lithos*, 100(1-4), 147–173, doi: 10.1016/j.lithos.2007.06.024.

5 Discussion and Summary

5.1 Geodynamic models of plume-ridge interaction for specific hotspot histories

This thesis presents a regional numerical model setup that considers a variety of time-dependent boundary conditions and demonstrates how this immensely versatile type of model can be used to gain further insights into an individual hotspot history and its effects on the Earth's surface at the examples of the Réunion, Iceland, and Kerguelen mantle plumes.

In each case, the crustal thickness contribution of the plume as predicted by the model is compared to surface observations: the timing of the melt (or crust) generation is compared to age dates of the igneous provinces associated with the respective hotspot, the distribution of volcanic material, also including smaller features, is compared to current topographic structures, and the modelled crustal thickness is compared to crustal thickness estimates derived from seismic studies. Moreover, in the case of the Kerguelen plume, the melt production rate in the model is compared to results from previous studies of age determinations and crustal volume estimates. All three case studies consistently confirm that this type of model is altogether able to reproduce the large-scale pattern of the volcanic edifices and provides a dynamic context for the generation of specific small-scale structures attributed to a particular hotspot – the main results of this thesis.

Especially important – and the major contrast to previous regional plume models (except for the preceding study of Gassmöller et al. (2016)) – is the consideration of the large-scale global mantle flow field, which can significantly deflect or tilt the plume tail, as shown in the case of the Réunion plume model. Another important feature is the realistic lithosphere thickness distribution, which has a large impact on the pattern of generated crust, since the lithosphere thickness mainly controls the melt generation and an inhomogeneous relief of the lithospheric base enables the effect of upside-down drainage, i.e. hot plume material can flow toward regions where the lithosphere is thin enough to enable melting. Furthermore, the use of a dehydration rheology effectively reduces the amount of generated melt to more realistic values. The combination of all these features in one regional model – as presented in this thesis – is a novel model setup.

The fact that the three case studies can answer different questions concerning the records of each respective hotspot shows the flexibility of this model setup, especially given that it cannot only reproduce the relatively classical example of the Réunion hotspot, but also more complicated records. Figure 5.1 shows comparable top views of the present-day state of the three models and visualizes how the regional, time-dependent boundary conditions result in very different plume shapes and melt fractions even though the parameters of the plume (excess temperature, inflow velocity and radius of the plume tail conduit) are identical.

Given the overall agreement of the model results and surface observations, each respective

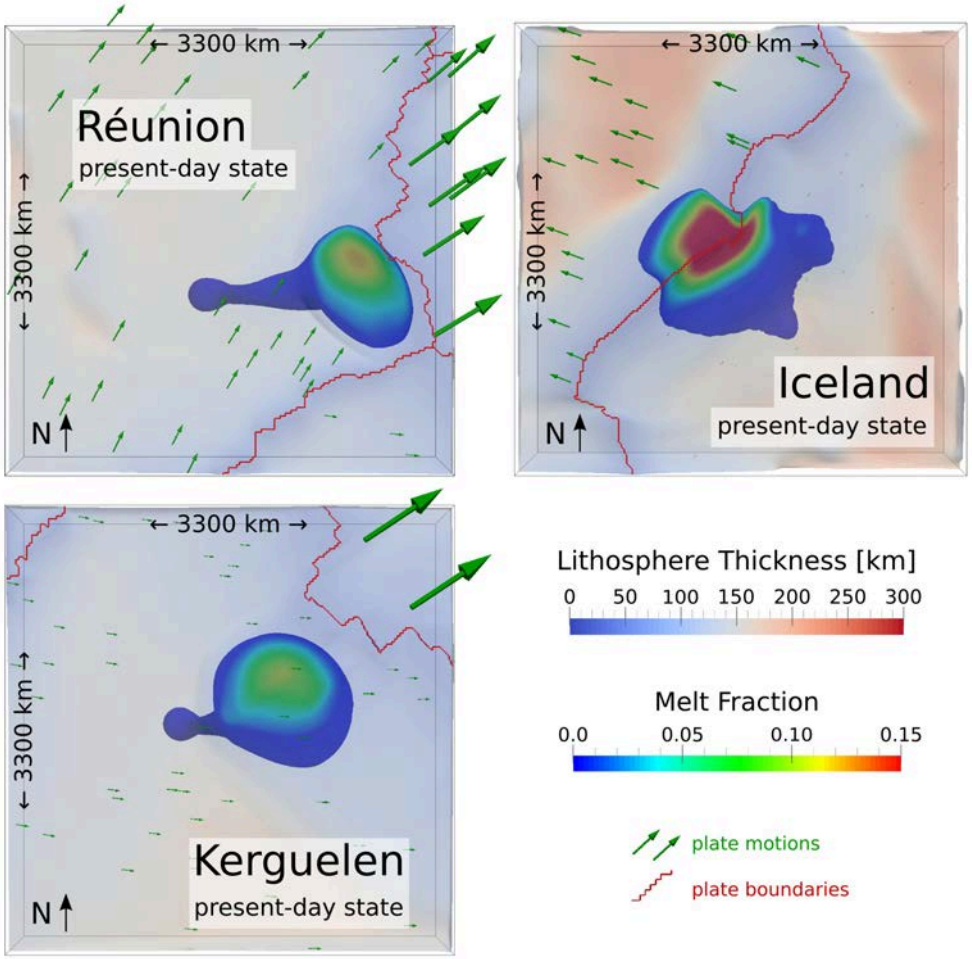

Figure 5.1: Top views of the three different case studies at the present-day state. Note how the local conditions, particularly the interaction with nearby ridges, result in very different plume shapes and melt fractions.

present-day model state can be regarded as a "prediction" for the current thermal state of the uppermost 660 km. In the case of the Réunion plume, first seismological results from the RHUM-RUM project have recently become available. (Note, however, that the geodynamic model had already been published at that time.)

Figure 5.2 shows a result that Mazzullo et al. (2017) achieved by surface wave tomography. The cross section in Figure 5.2b can be compared to the uppermost 300 km of the geodynamic model in Figure 2.6a, which yields a striking resemblance: in the seismic as well as in the geodynamic model, the plume reaches the base of the lithosphere underneath Réunion and flows through a sublithospheric flow channel toward the Central Indian Ridge, thus confirming the hypothesis of Morgan (1978).

Figure 5.3 shows a preliminary result of the whole mantle tomography model from the RHUM-RUM project. In agreement with previous results, as for example shown in Figure 2.S4, the Réunion plume rises from the African LLSVP in the lowermost mantle toward La Réunion. The rendered image in Figure 5.3b shows, however, that the plume structure is highly complex and needs to be studied as a three-dimensional structure.

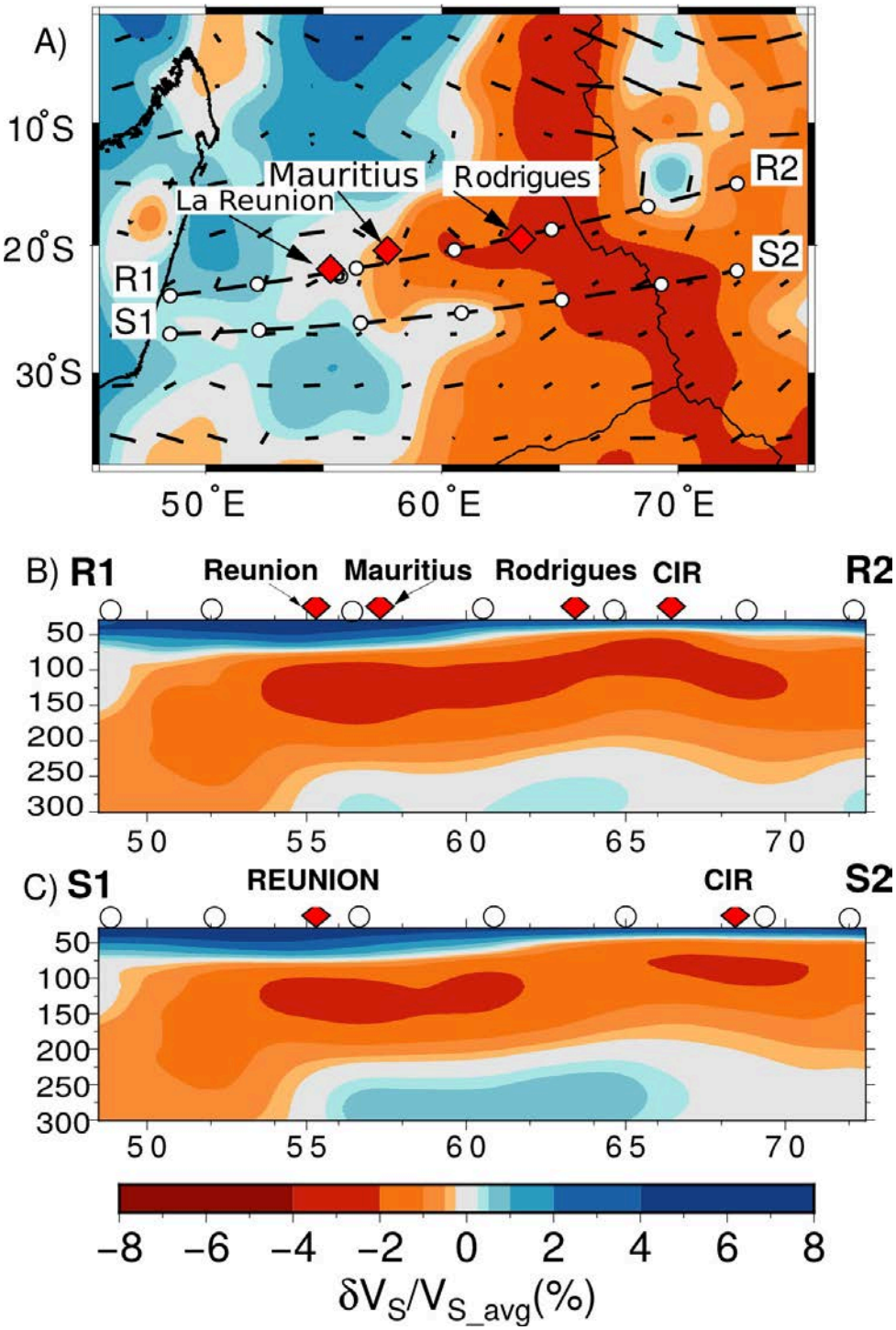

Figure 5.2: Surface wave tomography model from Mazzullo et al. (2017), where colors correspond to the shear wave velocities relative to the average shear wave velocities of the model. (a) Velocity distribution at 80 km depth around La Réunion. The locations of the cross sections in (b) and (c) are indicated by dotted lines. The cross sections show the low velocity signature of the plume rising to the base of the lithosphere underneath La Réunion and the channelled, sublithospheric flow toward the Central Indian Ridge (CIR). Note that the lateral resolution of approximately 500 km prevents any imaging of plume material migrating through the thick lithosphere and feeding the active volcano at La Réunion. (b) shows a remarkable agreement with the uppermost 300 km of Figure 2.6a.

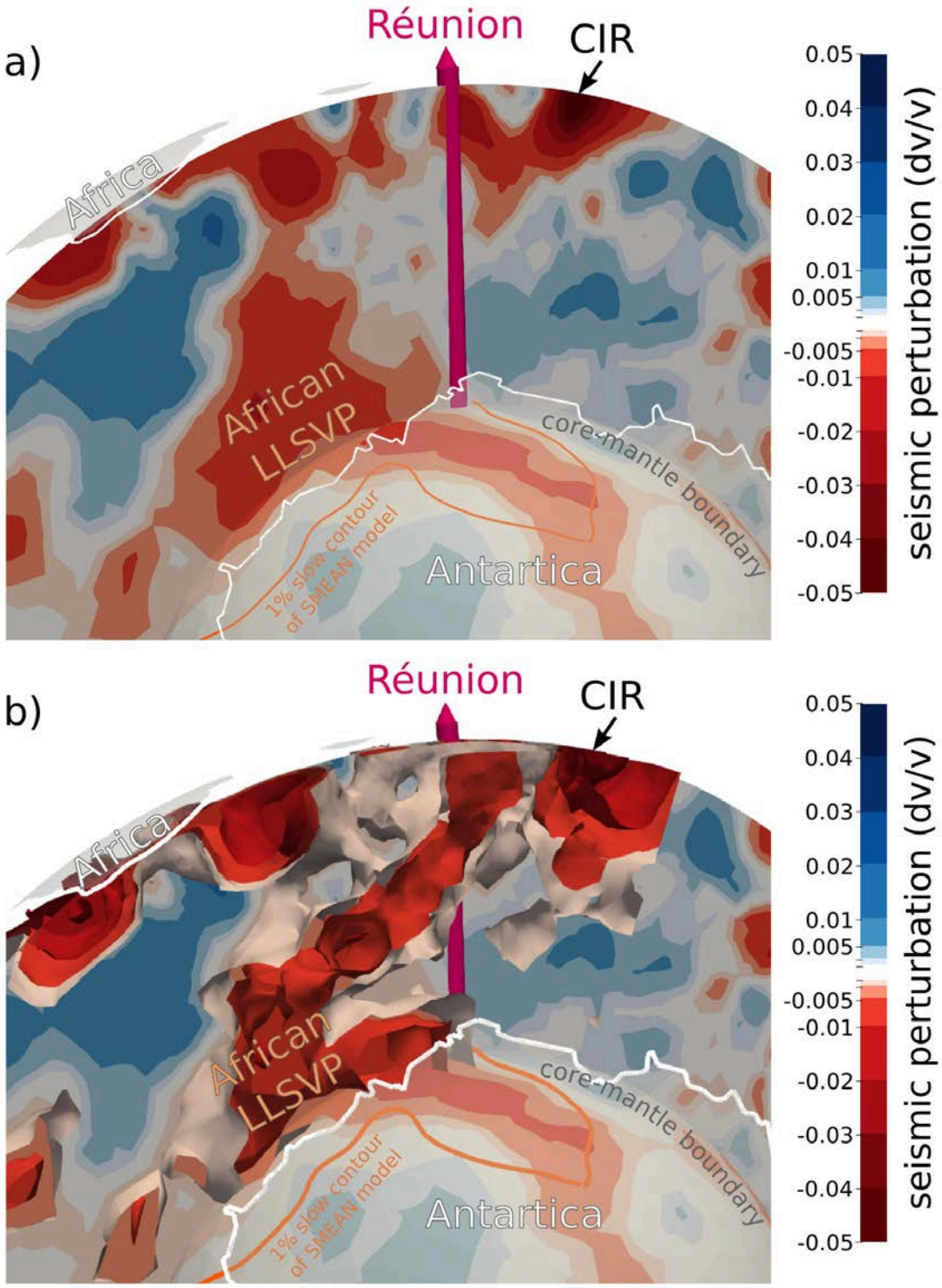

Figure 5.3: Whole mantle tomography model from the RHUM-RUM project (preliminary result), showing the region underneath South Africa, Réunion and the Central Indian Ridge (CIR), with colors corresponding to perturbations in seismic P-wave velocities (raw image courtesy of Maria Tsekhmistrenko, with modifications). The cross section in (a) shows how the Réunion plume seems to rise from the African LLSVP toward Réunion Island, in agreement with Figure 2.S4. The rendered image in (b) illustrates that the plume structure is much more complex than a vertical conduit. The orange line shows the 1% slow contour of the SMEAN model (Becker and Boschi, 2002), corresponding to the plume-generation zone at the CMB (Torsvik et al., 2006; Burke et al., 2008).

These two examples show clearly that the geodynamic model result is suited to be compared with structures in the mantle in addition to the comparisons with surface observations. If more well-resolved seismic images of the deeper mantle become available, as expected in the scope of the RHUM-RUM project, extending the regional geodynamic models to greater depths might be an interesting task for future models. However, for studying the melt distribution at the surface caused by a plume, the depth of 660 km is sufficient. In this regard, it might be interesting to use a more realistic formulation for melt transport in the code to test if the melt distribution can possibly be improved in future models.

The regional model setup works well in the three cases presented in this thesis, however, its success is limited by several factors, mainly by the accuracy of the applied boundary conditions. For example, if the lithosphere thickness is too high as in the Réunion model directly underneath the island, melting is prevented (see section 2.4.1 for details). Further, if the global flow is too strong, the plume conduit may be strongly deflected (discussed in section 2.4.3). Special attention should be paid to the earlier times of the model, since all reconstructions are naturally less constrained further back in time. The misplaced Deccan Traps in the Réunion model have shown another limitation of the model setup: it is not designed to handle melting in a continental environment and is therefore not the most suitable approach for modeling any plume history where continents play a major role.

Regarding the current scientific knowledge about plume dynamics and surface effects of specific hotspot histories, the models in this thesis highlight the importance of plume-ridge interaction and show that it is not necessary to attribute highly complicated properties to specific plumes in order to account for complex observations. The results of the models with fixed plume positions, constant plume inflow and not unusually hot plumes yield the best match with surface observations and allow (to a certain degree) to constrain the properties of a particular plume. Thus, this thesis contributes to the general understanding of plume-ridge interaction processes as well as to the very specific knowledge about individual plumes.

5.2 Conclusions for each individual hotspot history

The models presented in the three case studies in this thesis lead to the following conclusions concerning each individual hotspot history:

Réunion:

- The modelled Réunion plume leads to a crustal thickness pattern, that altogether agrees well with the structures of the hotspot track on topographic maps.
- The distinctive gap in the hotspot track between the Maldives and Chagos is generated due to the combined effects of the ridge geometry (in particular the distribution of transform faults) and plume-ridge interaction.
- The narrow crustal lineament of the Rodrigues Ridge is formed as the surface expression of

a long-distance sublithospheric flow channel between the upwelling plume and the closest segment of the Central Indian Ridge. This confirms the feasibility of the longstanding hypothesis of Morgan (1978) for the first time in a dynamic context.

- Considering the present-day state of the geodynamic model as a prediction for the thermal state in the mantle, comparisons to seismic tomography results (published later than the geodynamic model) yield an excellent match and provide further confirmation for the hypothesis of Morgan (1978).

Iceland:

- The modelled Iceland plume shows how plume material may have accumulated in an east-west corridor of thin lithosphere across Greenland and led to simultaneous melt generation west and east of Greenland. This may explain the extremely widespread volcanic material attributed to activities of the Iceland hotspot and shows that the model setup is also suited for more complicated hotspot histories.

- The model result agrees well with the new and highly resolved tomographic images of Lebedev et al. (2017).

Kerguelen:

- The model shows that a constant influx of the Kerguelen plume can result in a variable magma production rate if the plume interacts with nearby mid-ocean ridges. This is remarkable, because previous studies concluded that the plume might be dismembered or influenced by solitary waves in its conduit to produce such a variable melt production rate.

- The Ninetyeast Ridge in the model is generated by volcanic activities along the ridge axis between the Indian and Australian plate, while the Kerguelen plume was located beneath the Australian plate. This result is surprising since earlier studies described how the Indian plate migrated above the plume and created the Ninetyeast Ridge.

- Dynamically, it seems likely that the Amsterdam-Saint Paul Plateau is the result of plume material flowing from the upwelling toward the Southeast Indian Ridge, whereas previous (geochemical) studies attribute the volcanism at the Amsterdam-Saint Paul Plateau to a separate deep plume.

References

Becker, T. W. and L. Boschi (2002), A comparison of tomographic and geodynamic mantle models, *Geochem. Geophys. Geosyst.*, 3, 1003, doi: 10.1029/2001GC000168.

Burke, K., B. Steinberger, T. H. Torsvik, and M. A. Smethurst (2008), Plume Generation Zones at the margins of Large Low Shear Velocity Provinces on the core-mantle boundary, *Earth Planet. Sci. Lett.*, 265(1-2), 49–60, doi: 10.1016/j.epsl.2007.09.042.

Gassmöller, R., J. Dannberg, E. Bredow, B. Steinberger, and T. H. Torsvik (2016), Major influence of plume-ridge interaction, lithosphere thickness variations, and global mantle flow on hotspot volcanism – The example of Tristan, *Geochem. Geophys. Geosyst.*, 17, 1454–1479, doi: 10.1002/2015GC006177.

Lebedev, S., A. J. Schaeffer, J. Fullea, and V. Pease (2017), Seismic tomography of the Arctic region: inferences for the thermal structure and evolution of the lithosphere, *Geological Society, London, Special Publications*, 460, doi: 10.1144/SP460.10.

Mazzullo, A., E. Stutzmann, J.-P. Montagner, S. Kiselev, S. Maurya, G. Barruol, and K. Sigloch (2017), Anisotropic tomography around Réunion Island from Rayleigh waves, *J. Geophys. Res. Solid Earth*, 122, doi: 10.1002/2017JB014354.

Morgan, W. J. (1978), Rodriguez, Darwin, Amsterdam, ..., A second type of Hotspot Island, *J. Geophys. Res.*, 83(B11), 5355–5360, doi: 10.1029/JB083iB11p05355.

Torsvik, T. H., M. A. Smethurst, K. Burke, and B. Steinberger (2006), Large igneous provinces generated from the margins of the large low-velocity provinces in the deep mantle, *Geophys. J. Int.*, 167(3), 1447–1460, doi: 10.1111/j.1365-246X.2006.03158.x.

Selbstständigkeitserklärung

Hiermit erkläre ich, dass ich die vorliegende Arbeit selbstständig angefertigt, nicht anderweitig zu Prüfungszwecken vorgelegt und keine anderen als die angegebenen Hilfsmittel verwendet habe. Sämtliche wissentlich verwendeten Textausschnitte, Zitate oder Inhalte anderer Verfasser wurden ausdrücklich als solche gekennzeichnet.

Potsdam, den 22. November 2017

Eva Bredow